

1 **1 MICROSTRUCTURAL EVOLUTION AND MECHANICAL BEHAVIOUR OF**
2
3 **2 ALKALI ACTIVATED FLY ASH BINDER TREATED CLAY**

4
5
6 **3**
7
8 **4 Elodie Coudert^{a,b}, Dimitri Deneele^{c,d}, Giacomo Russo^{e*}, Enza Vitale^e, Alessandro**
9 **5 Tarantino^b**

10
11
12
13 **6**
14
15 **7 ^aDepartment of Civil and Mechanical Engineering, University of Cassino and Southern**
16 **8 Lazio, Via Gaetano di Biasio, 43, 03043 Cassino, FR, Italy**

17
18 **9 ^b Department of Civil and Environmental Engineering, University of Strathclyde, 75**
19 **10 Montrose Street, Glasgow, Scotland, G1 1XJ, United Kingdom**

20
21 **11 ^c Institut des Matériaux Jean Rouxel (IMN), Université de Nantes, CNRS, 2 rue de la**
22 **12 Houssinière, BP 32229, 44322 Nantes Cedex 3, France**

23 **13 ^dGERS-LEE, Univ Gustave Eiffel, IFSTTAR, F-44344 Bouguenais, France**

24 **14 ^e Department of Earth Science, Environment and Resources, University of Napoli**
25 **15 Federico II, Via Cinthia 21 80126, Napoli, Italy**

26 **16 * Corresponding Author, giaruso@unina.it**
27
28
29
30
31
32
33
34
35
36
37
38
39
40
41
42
43
44
45
46
47
48
49
50
51
52
53
54
55
56
57
58
59
60
61
62
63
64
65

1 **18 Abstract**

2
3
4 19 This work focuses on the use of alkali activated fly ash-based binder to enhance
5 20 engineering characteristics of soft clay-rich soils and as a substitute to standard stabilisers
6
7 21 (e.g., lime or cement). Especially, it examines the microstructural evolution of a calcium-
8
9 22 rich fly ash from coal combustion-based binder activated by a sodium-based alkaline
10
11 23 solution. To this end, the processes generating the microstructure and the evolution of the
12
13 24 pore network over time are investigated. A second point addressed by this study is how
14
15 25 the presence of-kaolin particles affects the microstructural features of the binder. The
16
17 26 microstructure has therefore been investigated by considering the binder alone and the
18
19 27 binder mixed with kaolin. The effects of microstructural evolution have been observed at
20
21 28 macroscopic level by means of one-dimensional compression tests.

22
23 29 The combination of completing techniques has been used including Optical microscopy,
24
25 30 Scanning Electron Microscopy and Mercury Intrusion Porosimetry in order to gain an
26
27 31 overview of the complex pore structure.

28
29 32 Microstructural changes occur around calcium-containing phases derived from fly ash
30
31 33 which are the reactive phases of the system. Namely, the dissolution of calcium-rich
32
33 34 grains leads to the formation of new compounds that first cover the grain surfaces and
34
35 35 then further grow into the available space. Furthermore, the evolution of the pore network
36
37 36 over time is characterized by a progressive filling of capillary pores by new compounds
38
39 37 while small nanometric pores are being formed and associated with the newly formed
40
41 38 silicate-calcium chains. Similar tendencies are observed when the binder is mixed with
42
43 39 the soil although the general porosity is lesser due to the filling of pores by small-sized
44
45 40 kaolinite platelets. Experimental evidences at microscale level have been linked to the
46
47 41 macroscopic behaviour of treated soil.

48
49 43 **Keywords:** Kaolin, Fly ash, Soil treatment, Alkali activated material, Microstructure,
50
51 44 Mechanical Behaviour

52
53
54 46 **1. Introduction**

55
56 47 Soft clay-rich soils are frequently encountered in construction sites. Their poor
57
58 48 mechanical performances represent a critical issue in engineering projects and are

1 49 commonly improved by using either Ordinary Portland Cement or lime as a soil stabiliser.
2
3 50 Nevertheless, those conventional stabilisers are associated with high carbon dioxide
4
5 51 emissions and energy intensive processes, significantly increasing the worldwide carbon
6
7 52 footprint (Scrivener and Kirkpatrick, 2008, Xi et al. 2016). The anthropogenic carbon
8
9 53 emissions have been increasingly recognized to be one of the main responsible of climate
10
11 54 changes and environmental degradation (United Nations, 2004). In the low carbon
12
13 55 agenda, it is then of outmost relevance the development of cost- and carbon-efficient
14
15 56 technologies. In the construction sector, for which cement production contributes to at
16
17 57 least 5–8% of global carbon dioxide emissions (Scrivener and Kirkpatrick, 2008),
18
19 58 alternative industrial by-products (e.g. high-calcium fly ash, rice husk ash, silica fume)
20
21 59 have been successfully used as cementing agents in soil improvement resulting in
22
23 60 environmental and economic benefits (Basha et al. 2003, Nalbantoğlu 2004, Sargent
24
25 61 2015, James & Pandian 2016).
26
27 62 As an alternative, the use of Alkali Activated Material (AAM) as a soil stabiliser is
28
29 63 gaining more and more attention over the past ten years. Alkali Activated Materials are
30
31 64 defined as any binder system derived by the reaction of an alkali metal source (usually
32
33 65 alkali hydroxide and alkali silicate solutions) with a solid aluminosilicate powder
34
35 66 (commonly metakaolin, fly ash, blast furnace slag or natural pozzolan) (Buchwald et al.,
36
37 67 2003; Shi et al., 2006). It gives a hardened material at room temperature with mechanical
38
39 68 properties potentially suitable for Portland cement replacement. Alkali Activated
40
41 69 Materials could constitute a viable sustainable soil binder because of their lower CO₂
42
43 70 emission process compared to traditional Portland cement (Duxson et al. 2007; McLellan
44
45 71 et al. 2011, Zhang et al. 2014). Furthermore, recent studies have shown a positive
46
47 72 potential and feasibility results of using alkali activated binders for soil improvement, and
48
49
50
51
52
53
54
55
56
57
58
59
60
61
62
63
64
65

1 73 this not only for different types of soil i.e. clayey soil (Wilkinson et al., 2010; Singhi et
2
3 74 al., 2016; Vitale et al. 2017, Vitale et al. 2019; Vitale et al. 2020a, 2020b), sandy clay
4
5 75 (Cristelo et al., 2011), marl, marlstone (Cristelo et al., 2012), silty sand (Rios et al., 2016)
6
7
8 76 or else road aggregates (Tenn et al., 2015); but also for different applications i.e. in deep
9
10 77 soft soil (Cristelo et al., 2011), at shallow depth (Zhang et al., 2013) or in rammed earth
11
12 78 construction (Silva et al., 2013).

13
14
15 79 Works on alkali activated binder treated soils are relatively recent and constitute a novel
16
17 80 domain of application. Our study particularly focuses on the use of a calcium-rich fly ash
18
19 81 from coal combustion activated by sodium-based alkaline solution as a binder for clay
20
21 82 kaolin stabilisation. Kaolin was selected as a model soil that represent a wide class of
22
23 83 clays encountered in engineering projects and for maintaining the system simple.
24
25 84 Kaolinite being not reactive to alkaline activation at ambient temperature, a more reactive
26
27 85 aluminosilicate source is required for chemical reactions to occur. For that purpose, a
28
29 86 calcium-rich fly ash was selected in the context of resource-saving being an industrial
30
31 87 waste. The main aim is to assess the feasibility of using this novel binder for soil
32
33 88 treatment.

34
35 89 When addressing the feasibility of using a class of material for a novel application, there
36
37 90 are several important parameters to consider such as the composition, microstructure and
38
39 91 processing which all ultimately affect the performance-to-cost ratio of a material
40
41 92 (Askeland et al., 2011). A detailed understanding of both the composition but also the
42
43 93 structure of the binder across length scales is therefore required in order to control
44
45 94 materials properties through its processing.

46
47 95 Two main length scales of investigation can be distinguished with relevant importance.
48
49 96 A first one is the particle scale and corresponds to the identification of the different phases
50
51
52
53
54
55
56
57
58
59
60
61
62
63
64
65

1 97 constituting particles in terms of chemical composition and crystal structure. Important
2
3 98 properties of particles depend on the arrangements of atoms and types of bonding within
4
5 99 each phase (Clemens et al., 2008). A second scale of observation is at the level of group
6
7
8 100 of particles, or microstructure. Microstructural investigations for alkali activated
9
10
11 101 materials are of prime importance as their physical properties depend largely on their pore
12
13 102 network characteristics and microstructure (Nath et al., 2016; Lawrence and Jiang, 2017).
14
15 103 This is associated with the fact that the microstructure controls the transport properties of
16
17 104 the binder and the stability of the matrix when exposed to aggressive agents (van Deventer
18
19 105 et al., 2015).
20
21
22 106 In our previous study the physicochemical evolution of similar systems than those herein
23
24 107 studied was carried out i.e. identification and evolution of the constitutive phases until 28
25
26 108 days of curing time at an atomic level. It showed that the soil i.e. kaolin was not reactive.
27
28
29 109 Whereas, fly ash was partly reactive. Some of its phases such as the vitreous phase and
30
31 110 quartz were mainly unreactive, while calcium-containing phases represented the reactive
32
33 111 phases. The new compounds formed were an amorphous silicate consisting of chains
34
35 112 combined with calcium probably incorporating three-dimensional four-fold aluminium
36
37 113 environments and thenardite Na_2SO_4 (Coudert et al., 2019).
38
39
40 114 The present work focusses on the microstructural description, taking into account the
41
42 115 knowledge gained about the physicochemical evolution of the system. The study was
43
44 116 designed in three stages. An initial stage consisted in the identification of the phases
45
46 117 present in the reactive aluminosilicate source i.e. the original calcium-rich fly ash and
47
48 118 description of their structure, shape and size distribution. The different constituents of fly
49
50 119 ash being inhomogeneously reactive (Provis and Deventer, 2009), it was important to
51
52 120 identify the reactive phases around which microstructural changes were predominant. A
53
54
55
56
57
58
59
60
61
62
63
64
65

1 121 second stage focussed on the investigation of the microstructural evolution of the alkali
2
3 122 activated fly ash binder during the first 28 days of curing, including (i) a description of
4
5 123 the dispersion and arrangement of phases, (ii) an understanding of which processes
6
7 124 generate the microstructure over time and (iii) a pore network characterisation. Fly ash
8
9 125 being a highly inhomogeneous material (Provis and Deventer, 2009), a key point was to
10
11 126 determine the homogeneity of processes across the sample at a microscopic level.
12
13 127 Besides, a particular emphasis was put at understanding microstructural changes and
14
15 128 processes around calcium particles which are the main reactive phases. A third stage
16
17 129 focussed on the interaction of the fly ash-based binder with the kaolin clay to understand
18
19 130 how the presence of kaolin modifies the microstructural features of the system. As
20
21 131 previously stated, kaolinite is unreactive during the alkaline activation. However, because
22
23 132 of its small size kaolinite acts as a filler of the porosity (Coudert et al., 2019) and
24
25 133 undoubtedly plays a role on the microstructural evolution. The effects at macroscopic
26
27 134 level have been highlighted with reference to one dimensional compression results,
28
29 135 showing the improvement of the mechanical performances of the treated soil as function
30
31 136 of binder percentage and curing time. A final comparison between the performance of
32
33 137 cement treated soil with alkali activated binder treated soil has shown for highlighting the
34
35 138 effectiveness of the improvement.
36
37
38
39
40
41
42
43
44
45
46
47
48
49
50
51
52
53
54
55
56
57
58
59
60
61
62
63
64
65

141 **2. Material and methods**

142 *2.1 Materials*

143 A Polish fly ash derived from hard coal and coal slime combustion in fluidised bed boiler
144 was used. Its chemical analysis is given in Table 1, and consists primarily of SiO_2 , Al_2O_3

145 and CaO. The fly ash contains, approximately, 52% of particles sized lower than 45 μm
 146 and 41% lower than 10 μm .

147 Speswhite kaolin provided by Imerys Minerals UK, and whose chemical composition is
 148 given in Table 1 was used. It is mainly constituted of kaolinite (95%) and secondarily of
 149 muscovite (4%) (Chemeda, 2015). The kaolin contains, approximately, 100 % of particles
 150 sized lower than 10 μm and 80 % lower than 2 μm .

151 A unique alkaline solution was used: a sodium silicate with a mass ratio $\text{SiO}_2/\text{Na}_2\text{O}$ of
 152 1.7 and a dry mass percentage of 44%; supplied by Woellner Group and named GEOSIL
 153 34417.

154
 155 Table 1 - Chemical composition (wt. %) of raw fly ash and kaolin.

	SiO_2	Al_2O_3	Fe_2O_3	CaO	$\text{CaO}_{\text{free}}^{\text{a}}$	MgO	SO_3	Na_2O	K_2O	H_2O	L.o.I.
Fly ash	39.4	19.8	7.4	18.6	5.2	1.8	4.1	2.0	1.8	0.0	1.7 ^b
Kaolin	49.2	34.5	1.2	0.0	0.0	0.2	0.0	0.1	1.7	13.1	12.0 ^c

156 ^a Free calcium oxide content

157 ^b L.o.I = Loss on ignition 900 °C

158 ^c L.o.I = Loss on ignition 1000 °C

160 *2.2 Sample preparation*

161 Sample preparation consisted in (i) mix of liquid sources i.e. silicate and water (ii) mix
 162 of aluminosilicate powders i.e. fly ash and kaolin in the case of soil-source sample (iii)
 163 mix of (i) and (ii) previously prepared.

164 For microstructural analyses, two types of mixes were studied and named F100 and KF50.
 165 F100 is the fly ash-based alkali activated binder. It corresponds to a solid phase made of
 166 fly ash only, whereas KF50 is the alkali activated binder treated soils and corresponds to
 167 a solid phase made of 50% of fly ash and 50% of kaolin in mass.

1 168 To ensure a good workability, the amount of added water with respect to the solid mass
2
3 169 (e.g. mass of kaolin and fly ash) was fixed to 50% for all the samples. Additionally, the
4
5 170 mass ratio of alkaline solution to fly ash was fixed to 50% for all the samples, giving the
6
7
8 171 initial molar ratios (considering that kaolin is unreactive): $\text{Si/Al} = 2.0$, $\text{Si/Na} = 3.5$ and
9
10 172 $\text{Al/Na} = 1.8$. The Al/Na ratio was not fixed to one because of the presence of calcium
11
12 173 ions in high quantity in our system playing a role of charge compensation as well as
13
14
15 174 sodium.

16
17
18 175 The paste obtained was poured in closed plastic molds and cured at room temperature (20
19
20 176 °C). Samples were finally demoulded and freeze-dried at curing times of 24 hours, 3, 7
21
22
23 177 or 28 days.

24
25 178 Samples for one dimensional compression tests were prepared with the described
26
27 179 technique. Three mixes have been considered in the study, namely KF10, KF20 and KF40
28
29 180 corresponding to a solid phase made of 10%, 20% and 40% of fly ash with reference to
30
31 181 dry mass of solids (fly ash+ kaolin). Remoulded samples were prepared by hand mixing
32
33 182 solids, alkaline solution and water at their liquid limits (i.e. $w_L=67\%$ for KF10, $w_L=60\%$
34
35 183 for KF20, $w_L=55\%$ for KF40). Samples were poured in the mould and placed in
36
37 184 oedometer cell without compaction. Treated samples were cured for 24 hours, 7, 14, 28
38
39
40 185 and 60 days before mechanical testing.

41
42
43
44
45 186

46 47 187 *2.3 Methods*

48
49 188 Samples were studied by Optical and Scanning Electron Microscope from polished
50
51 189 section. Freeze-dried samples were impregnated under a vacuum with an acrylic resin
52
53 190 (LR White). The polymerisation of the resin was performed in an oven at 60 °C over 48
54
55
56
57 191 h. The samples were then polished with diamond powder. The observations from Optical
58
59
60
61
62
63
64
65

1 192 Microscopy were done with a Nikon LV100 polarizing optical microscope combined with
2
3 193 a ccd Nikon DS-2Mv camera and the NIS Element BS software. Whereas the
4
5 194 observations from Scanning Electron Microscope were done with a HITACHI SU5000
6
7
8 195 scanning electron microscope equipped with an energy-dispersive X-ray analyser
9
10 196 (Quantax microanalyser system composed of X-Flash® SDD detector and the Esprit
11
12 197 software). The polished samples were coated with carbon before the observation. The
13
14 198 microscope was operated at an accelerating voltage of 20 kV and working distances of
15
16
17 199 10 mm.
18
19
20 200 MIP tests were performed by a double chamber Micromeritics Autopore III apparatus. In
21
22 201 the filling apparatus (dilatometer) samples were outgassed under vacuum and then filled
23
24 202 by mercury allowing increase of absolute pressure up to ambient one. Using the same unit
25
26 203 the intrusion pressure was than raised up to approximately 200 kPa by means of
27
28 204 compressed air. The detected entrance pore diameters ranges between 134 μm and 7.3
29
30 205 μm (approximately 0.01 MPa - 0.2 MPa for a mercury contact angle of 139°). After
31
32 206 depressurisation to ambient pressure, samples were transferred to high-pressure unit,
33
34 207 where mercury pressure was increased up to 205 MPa following a previously set intrusion
35
36 208 program. The smallest detected entrance pore diameter was about 7 nm. Corrections to
37
38 209 pore-size distribution due to compressibility of intrusion system were applied performing
39
40 210 a blank test.
41
42 211 One dimensional compression tests have been performed in standard oedometer cells,
43
44 212 where vertical stress was conventionally applied in successive steps ($\Delta\sigma_v/\sigma_v = 1$) within
45
46 213 the stress interval $10 \div 2400$ kPa. Micrometer dial gauges with an accuracy of 0.001 mm
47
48 214 have been used to measure vertical displacements.
49
50
51
52
53
54
55
56
57 215
58
59
60
61
62
63
64
65

1 216 **3. Results and discussion**

2
3 217 The first section of results presents the general characteristics of the raw fly ash which
4
5
6 218 constitutes the reactive aluminosilicate source of the mixes. The second part examines
7
8 219 the microstructural evolution of the binder. The third part focusses on the description of
9
10 220 system made by kaolin and the alkali activated binder and its mechanical performance.

11
12
13 221

14
15 222 *3.1 Raw fly ash*

16
17 223 The fly ash used here contains various components. Its composition consisting of (i) a
18
19 224 vitreous phase and (ii) various crystalline phases i.e. calcium-containing minerals:
20
21 225 anhydrite CaSO_4 , calcite CaCO_3 and portlandite $\text{Ca}(\text{OH})_2$, and other minerals: quartz
22
23 226 SiO_2 , feldspar $(\text{K,Na,Ca})(\text{Si,Al})_4\text{O}_8$, hematite Fe_2O_3 and muscovite
24
25 227 $(\text{Si}_3\text{Al})\text{O}_{10}(\text{Al}_2)(\text{OH})_2\text{K}$ (Coudert et al., 2019).

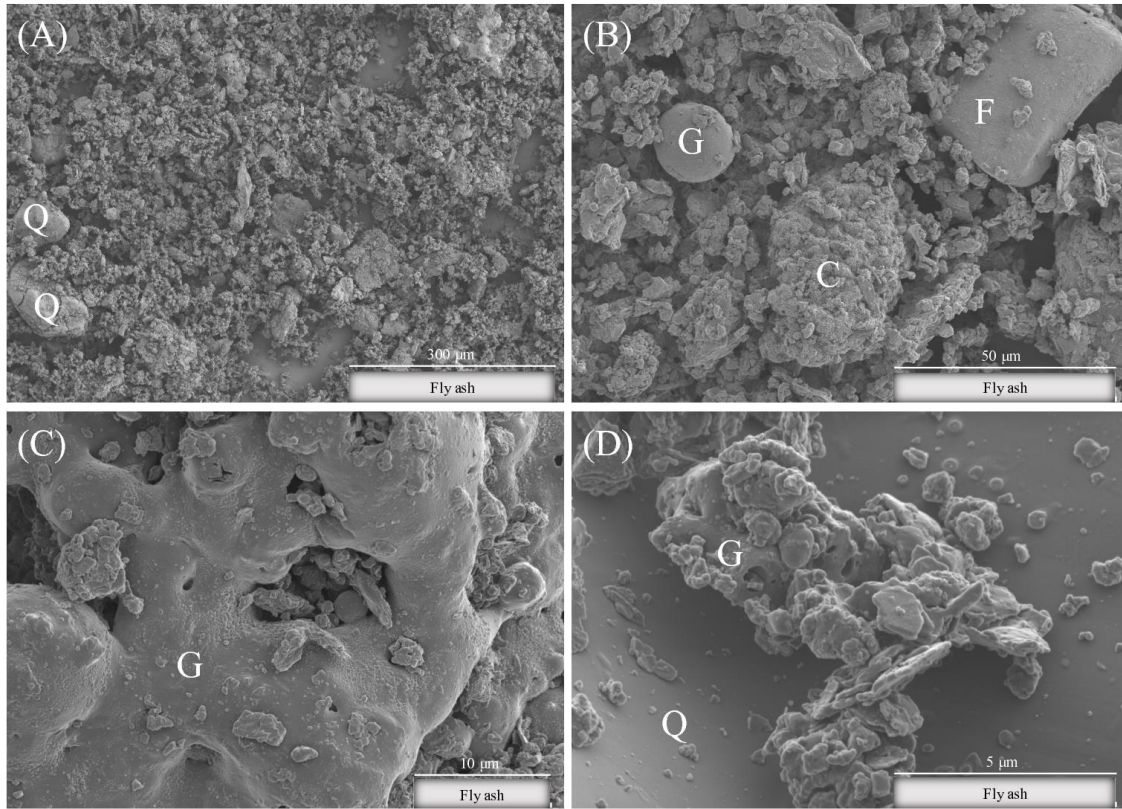
26
27 228 Its particle size distribution reflects this diversity with 52 % of particles lower than 45
28
29 229 μm , 41 % of particles lower than 10 μm and 12 % of particles lower than 2 μm .

30
31 230 Figure 1 confirms this great variety also detectable by Scanning Electron Microscopy. In
32
33 231 fact, the fly ash presents an extremely heterogeneous microstructure with particles of
34
35 232 different shapes and ranging from 1 μm to more than 200 μm . The vitreous phase is itself
36
37 233 heterogeneous and made of (i) some spherical particles (see G Figure 1B), (ii) bigger
38
39 234 unshaped particles (see G Figure 1C) and (iii) aggregates of small particles primarily (see
40
41 235 G Figure 1D).

42
43 236 Some crystallised angular shaped minerals can also be distinguished and correspond to
44
45 237 quartz (see Q Figure 1A&D) or feldspar (see F Figure 1B).

46
47 238 Finally, regarding calcium-rich phases, our previous study showed that calcium-
48
49 239 containing minerals i.e. anhydrite CaSO_4 , calcite CaCO_3 and portlandite $\text{Ca}(\text{OH})_2$ are

1 240 interlaced together (Coudert et al., 2019). Especially, they are interlinked within a nodule
2
3 241 shape structure generally of 50 to 200 μm size as seen on Figure 1B (particle labelled C).
4
5
6 242



243

244 **Fig. 1** SEM micrographs of the raw fly ash; C=calcium-rich particle; F=feldspar;
245 G=glass; Q=quartz.

246

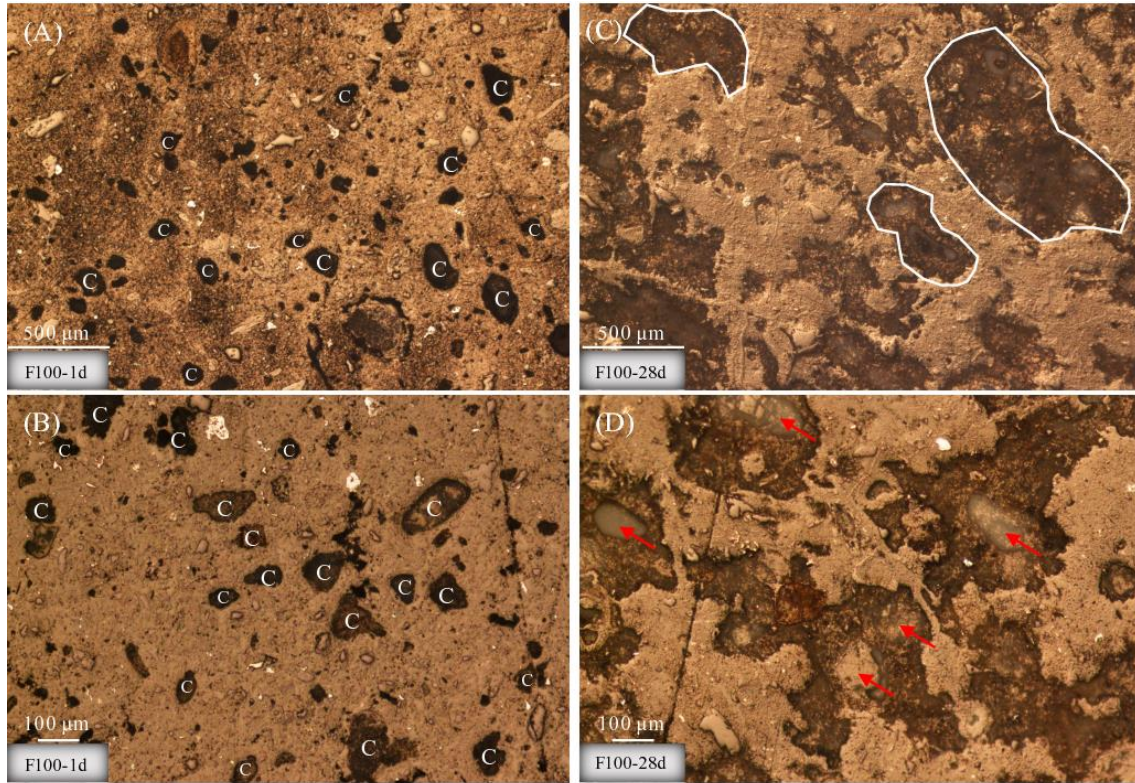
247 3.2 Alkali activated fly ash binder

248 3.2.1 Optical Microscopy

249 Figure 2 shows the microstructural evolution of the alkali activated fly ash binder over
250 time by optical microscopy. Observations were carried out until 28 days as chemical
251 reactions are fully developed at that curing time (Coudert et al., 2019).

252 After 24 hours of curing, dispersed dark spots of around 50 μm to 200 μm size are seen
253 across the overall sample (see particles labelled C on Figure 2A&B), and correspond to
254 reactive calcium-rich nodules by analogy with the previous observations of the raw fly

1 255 ash constituents (section 3.1). They represent approximately 15 % of the mixture.
2
3 256 Whereas the brown matrix includes the vitreous phase and calcium-free minerals from
4
5
6 257 fly ash.



258
259 **Fig. 2** Optical microscopy images of the alkali activated fly ash binder F100 (A) and (B)
260 after 24 hours, (C) and (D) at 28 days; C=calcium-rich particle.
261

262 By comparison, at 28 days, no dark spots are visible but instead large dark zones whose
263 edges are less well defined (see encircled areas on Figure 2C), and correspond to new
264 products formed. Figure 2D shows a closer observation of those large dark reactive areas.
265 The initial nodule shapes can still be distinguished at 28 days but instead of a dark spot
266 as observed at 24 hours it is a hollowed greyish structure that is seen as shown by the red
267 arrow (Figure 2D). This structure is associated with dissolution features over time of the
268 calcium-rich phase, and in accordance with the previous results about the
269 physicochemical evolution which indicate that calcium-containing phases are the main

1 270 reactive phases. New compounds corresponding to dark areas are therefore formed
2
3 271 around the hollowed dissolved calcium nodules. Those new compounds have been
4
5 272 identified in a previous study as thenardite Na_2SO_4 , and an amorphous silicate consisting
6
7
8 273 of chains combined with calcium probably incorporating three-dimensional four-fold
9
10 274 aluminium environments (Coudert et al., 2019).

11
12
13 275 As a consequence of those observations, the spreading of the darker areas at 28 days gives
14
15 276 an idea of the extent of the reaction and widening of the new compounds formation across
16
17
18 277 samples. In this system, half of the sample encompasses the new compounds and is hence
19
20 278 reactive whereas the initial calcium nodules represented only 15 % of the sample.
21
22 279 Besides, those new compounds seem homogeneously spread across the sample which
23
24
25 280 likely could give a homogeneously reinforced material at the macroscopic scale.

26
27
28 281 Results from optical microscopy therefore match with the observed physicochemical
29
30 282 evolution i.e. principal changes occur around calcium-rich reactive particles. That is why
31
32 283 the next session focusses on the in-situ microstructural transformation of calcium-rich
33
34
35 284 phases induced by the alkaline solution.

36
37 285

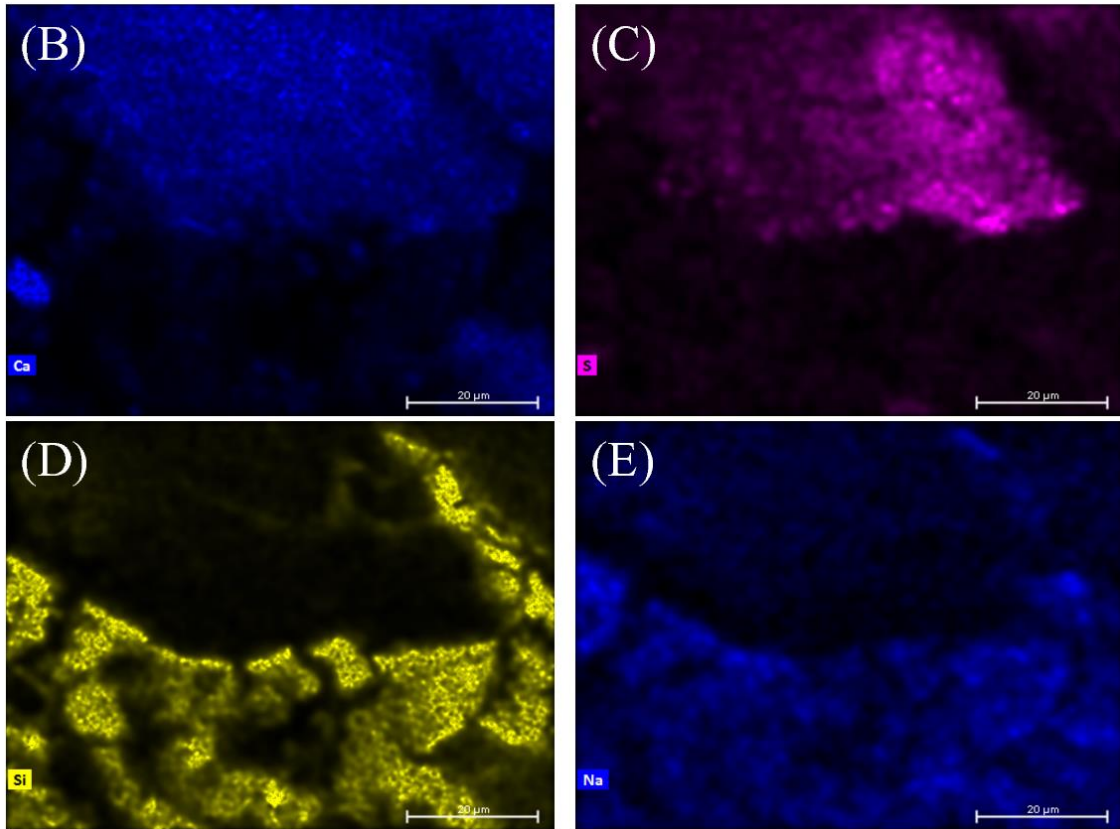
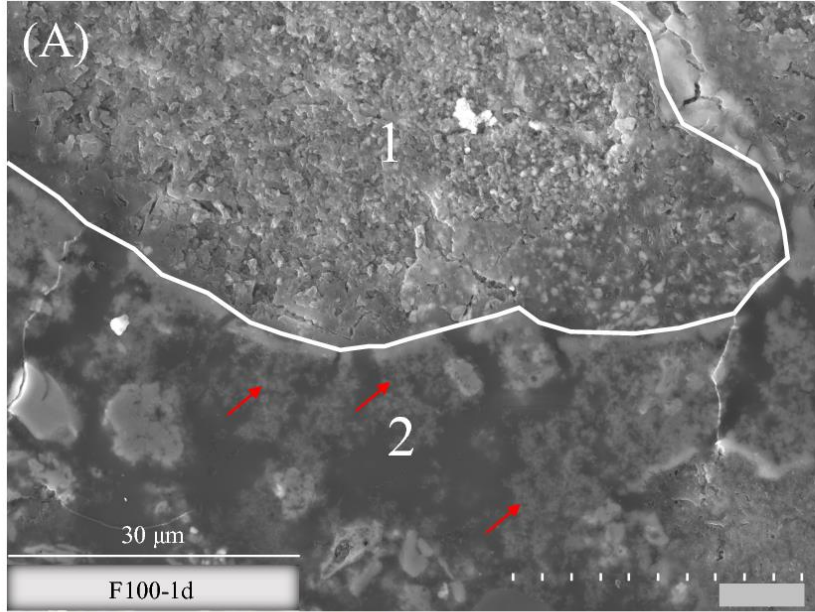
38 286 3.2.2 Scanning Electron Microscopy (SEM)

39
40
41
42 287 Figure 3 shows microstructural observations from a polished section and combined
43
44 288 chemical mappings of the alkali activated fly ash binder after 24 hours of curing.
45
46
47 289 Chemical mappings on Figure 3B&C indicate the presence of a calcium-rich nodule
48
49 290 labelled 1 on Figure 3A and predominantly made of calcium and sulphur. Additionally,
50
51
52 291 those calcium-rich particles display a granular aspect on their surface.

53
54 292 Surrounding this calcium-rich particle, the area labelled 2 on Figure 3A corresponds to a
55
56
57 293 porous zone distinguishable by the presence of dense black areas characteristic of the
58
59
60
61
62
63
64
65

1 294 filling resin of low atomic mass. Chemical mappings of that porous zone show an
2
3 295 enrichment in silicon and sodium (Figure 3D&E) indicating the presence of the sodium-
4
5 296 silicate Na_2SiO_3 alkaline solution at that short curing time. Additionally, filament like
6
7
8 297 structures are observed within that area (see red arrow on Figure 3A), and considered as
9
10 298 the beginning of the secondary phases formation i.e. the amorphous silicate consisting of
11
12 299 chains combined with calcium and potentially aluminium. In fact, a former study about
13
14 300 cementitious microstructures has shown the formation of similar arrangements associated
15
16 301 with Calcium Silicate Hydrates whose structure strongly resembles the one of our newly
17
18 302 formed chains (Scrivener, 2004). Moreover, it appears that those filament structures are
19
20 303 stacked around particles corresponding to the initiation of the reaction process after 24
21
22 304 hours of curing.
23
24
25 305 Figure 4 also shows microstructural observations of the alkali activated fly ash binder
26
27 306 after 24 hours of curing, and particularly illustrates the microstructural difference
28
29 307 between a calcium-rich particle and a particle from the vitreous phase both originally
30
31 308 present in the fly ash. They can both be distinguished by SEM by their chemical
32
33 309 composition and microstructural features. Regarding calcium-rich particles, they present
34
35 310 a nodule shape with a granular surface (see 3 on Figure 4A) as previously observed
36
37 311 (Figure 3A). Whereas particles from the vitreous phase display a vesicular structure (see
38
39 312 1 on Figure 4A) and can be distinguished using chemical mappings by their enrichment
40
41 313 in silicon and aluminium (Figure 4D&E).
42
43 314 In between those two particles, a porous area labelled 2 on Figure 4A and with filament
44
45 315 like structures can once again be observed and evidences the initiation of the reaction
46
47 316 processes. Consequently, from Figure 3 as from Figure 4 it is noticeable that the alkali
48
49 317 activated binder after 24 hours of curing presents a high porosity created by the fly ash
50
51
52
53
54
55
56
57
58
59
60
61
62
63
64
65

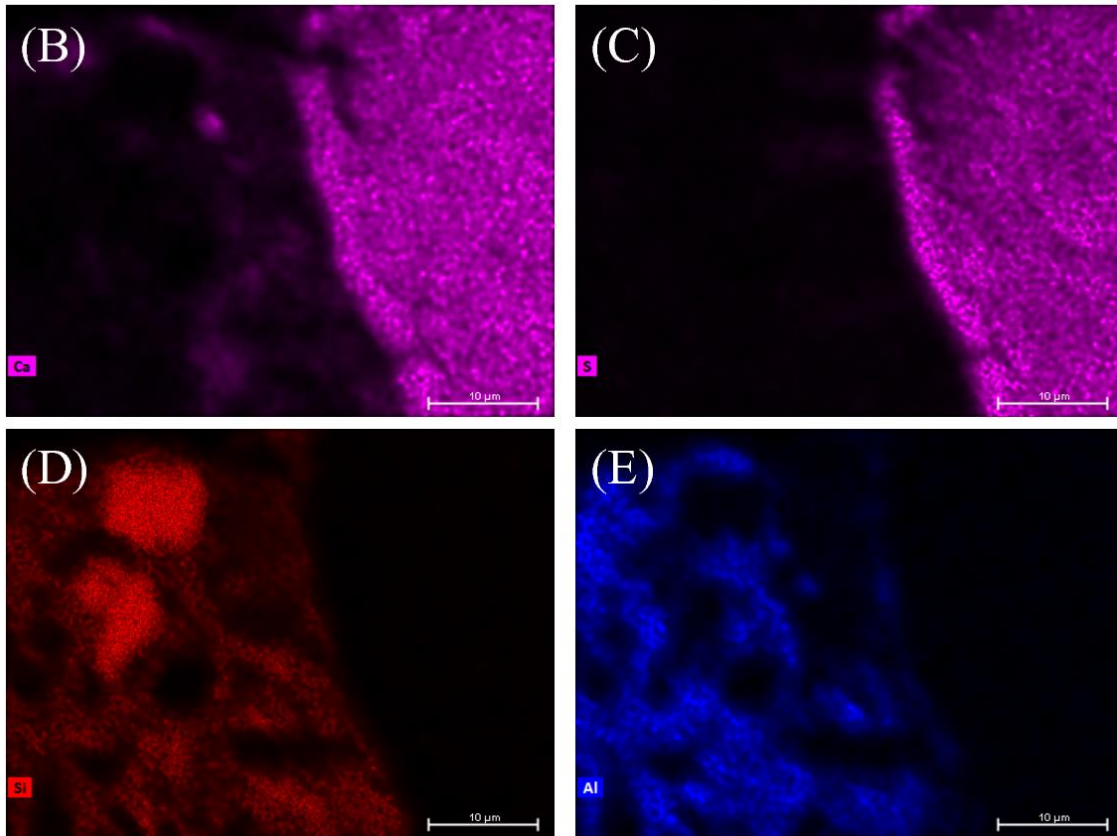
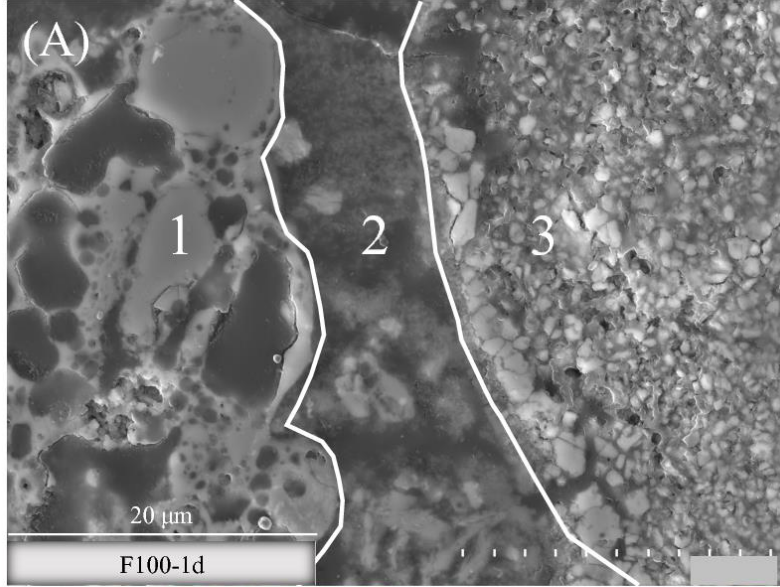
1 318 grains of various sizes and that is filled by water, alkaline solution, and the new product
2
3 319 starting to be formed.
4
5
6 320



321

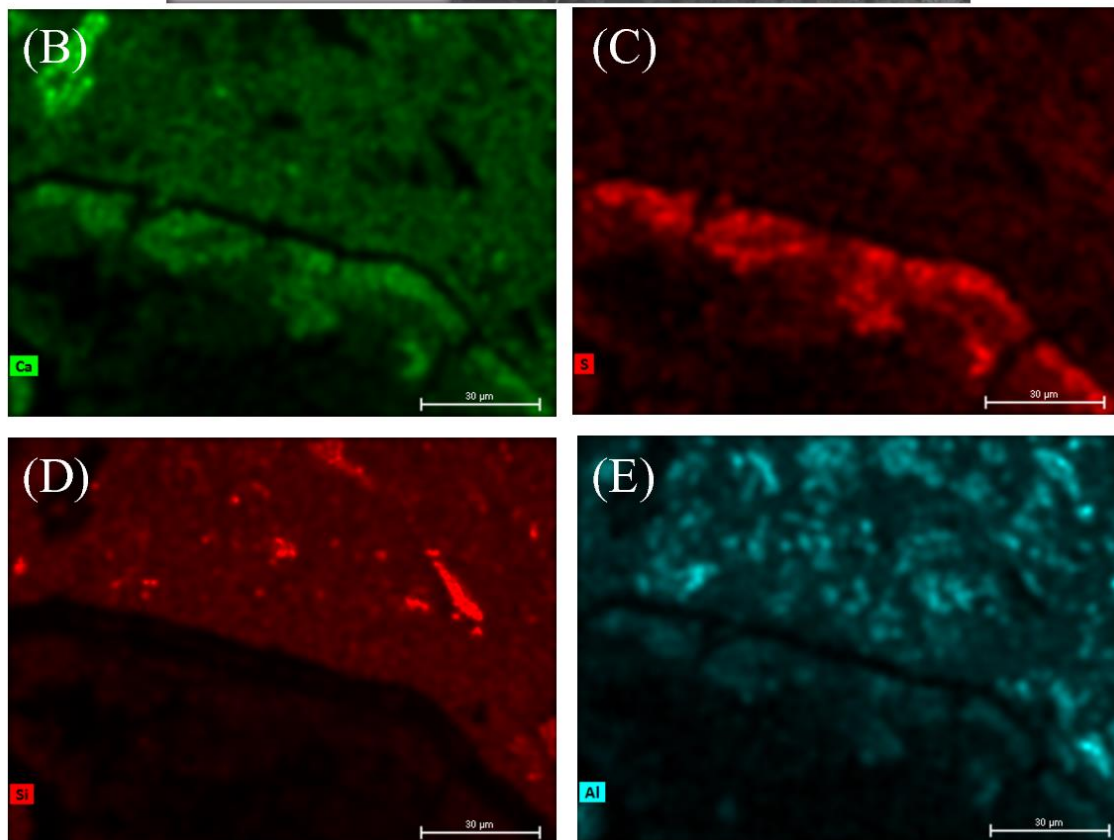
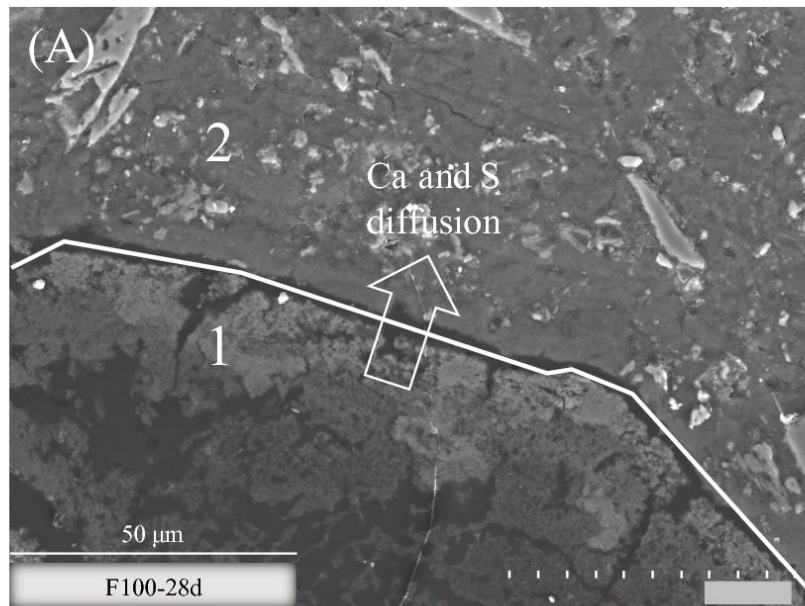
1
2
3
4
5
6
7
8
9
10
11
12
13
14
15
16
17
18
19
20
21
22
23
24
25
26
27
28
29
30
31
32
33
34
35
36
37
38
39
40
41
42
43
44
45
46
47
48
49
50
51
52
53
54
55
56
57
58
59
60
61
62
63
64
65

322 **Fig. 3** SEM observations of the alkali activated fly ash binder F100 after 24 hours of
323 curing: (A) SEM micrograph, and chemical mappings of: (B) calcium, (C) sulphur, (D)
324 silicon and (E) sodium.
325



326
327 **Fig. 4** SEM observations of the alkali activated fly ash binder F100 after 24 hours of
328 curing: (A) SEM micrograph, and chemical mappings of: (B) calcium, (C) sulphur, (D)
329 silicon and (E) aluminium

1 330
2
3 331 Figure 5 shows SEM observations and combined chemical mappings of the alkali
4
5
6 332 activated fly ash binder after 28 days of curing. It especially focuses on the interface
7
8 333 between a calcium-rich nodule labelled 1 and the surrounding matrix labelled 2.
9
10 334 Regarding the calcium-rich nodule, it displays a hollowed structure, especially in its
11
12
13 335 centre, and as similarly observed previously by optical microscopy in section 3.2.1. In
14
15 336 addition, those hollowed structures show dense black zones indicating the presence of
16
17
18 337 filling resin and therefore porosity. Those structural characteristics strongly contrast with
19
20 338 calcium nodules after 24 hours presenting a granular surface, and are attributed to the
21
22 339 dissolution of calcium-rich phases over time leaving behind a porous body. It is supported
23
24
25 340 by chemical mappings on Figure 5B&C showing a strong impoverishment in calcium and
26
27
28 341 sulphur in the hollowed area with respect to nodules after 24 hours.
29
30 342 An enrichment in calcium and sulphur is seen in the outer part of the nodule suggesting
31
32 343 a mechanism of dissolution of calcium and sulphur moving from the calcium nodules to
33
34
35 344 the matrix. Moreover, few silicon supplied in that system by the alkaline solution is
36
37
38 345 detected above the edges of the calcium nodule and inside implying that the alkaline
39
40 346 solution penetrates through the calcium-nodule accelerating its dissolution. The
41
42 347 coloration due to the silicon presence inside the nodule is few marked as unreactive quartz
43
44 348 which corresponds to intensely coloured and well defined edges spots on the silicon
45
46
47 349 chemical mapping (Figure 5D) are present in the matrix and induces a rescaling of the
48
49 350 silicon coloration.
50
51
52 351
53
54
55
56
57
58
59
60
61
62
63
64
65



352

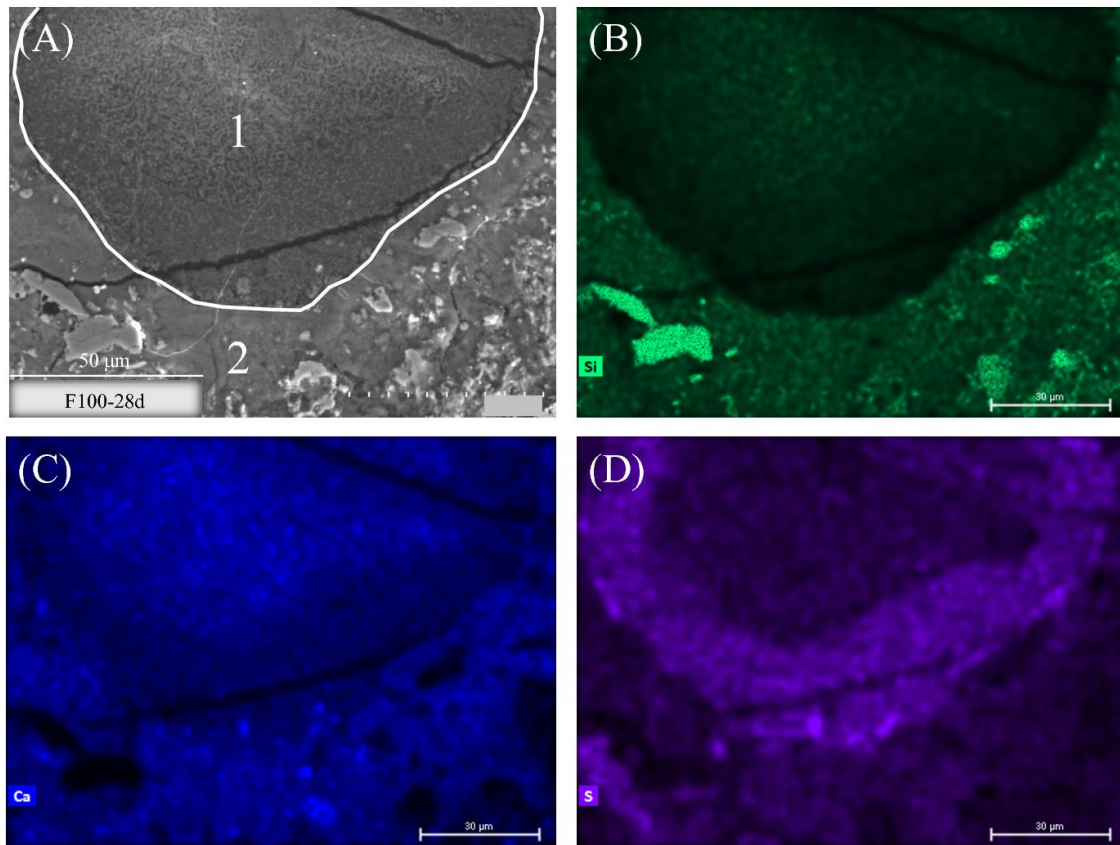
353 **Fig. 5** SEM observations of the alkali activated fly ash binder F100 at 28 days: (A) SEM
 354 micrograph, and chemical mappings of: (B) calcium, (C) sulphur, (D) silicon and (E)
 355 aluminium.

356

357 Regarding the area surrounding the calcium nodule labelled 1, it is massive and presents
 358 a low porosity compared to the binder after 24 hours. It corresponds to the area where

1 359 new products are formed. Its chemical mappings show a high content of calcium and
2
3 360 silicon which is in accordance with the physicochemical investigation that showed the
4
5 361 formation of silicate chains combined with calcium over time. The wide diffusion of
6
7
8 362 calcium into the matrix is clearly seen from Figure 5 when compared to the binder after
9
10 363 24 hours of curing for which calcium is contained and restrained to the nodule surface
11
12 364 (see Figure 3 and Figure 4). Concerning sulphur elements, as well initially present in the
13
14 365 nodule in the form of anhydrite CaSO_4 , its dissolution occurs in a lesser extent and seems
15
16 366 stopped to the outer part of the nodule at 28 days (Figure 5C). The physicochemical
17
18 367 evolution of this system showed that dissolved sulphur combine with sodium to form
19
20 368 thenardite Na_2SO_4 at 28 days (Coudert et al., 2019). Consequently, the presence of
21
22 369 thenardite is restrained to small areas around the calcium-rich particles, whereas silicate
23
24 370 two-dimensional chains combined with calcium are widely spread all around the calcium
25
26 371 nodules. The formation of this thenardite crust limited around calcium nodules can be
27
28 372 explained by the low amount of sulphur elements compared to calcium (see chemical
29
30 373 composition of the raw fly ash in Table 1), that already all precipitated in this small area.
31
32 374 The conjoint chemical mapping of sodium to localise thenardite is not shown here as
33
34 375 sodium is a volatile element for which it is difficult to get a chemical mapping showing
35
36 376 a reliable representativeness of sodium dispersion.
37
38 377 Finally, important crackings are observed around calcium-rich particle as seen on Figure
39
40 378 5 and are associated with shrinkage processes frequently observed for alkali activated
41
42 379 materials (Fang et al., 2018).

52 380



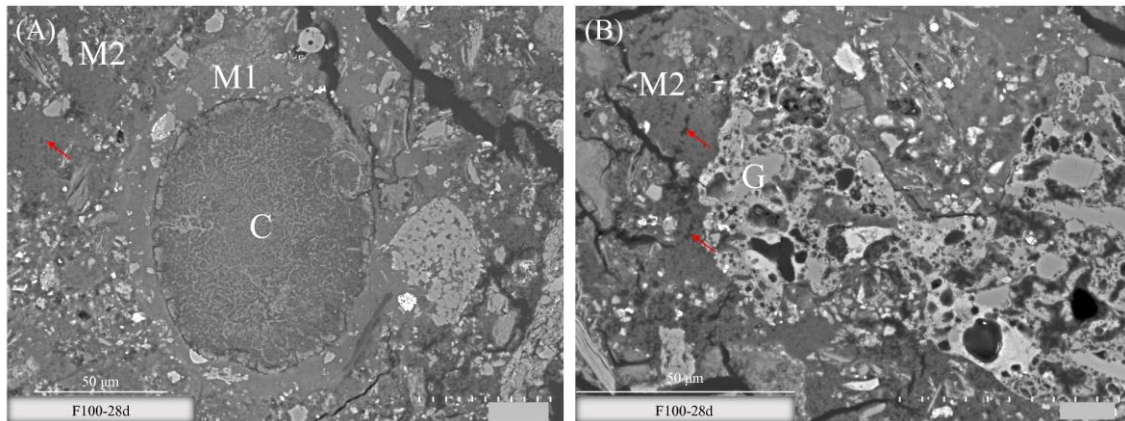
381

382 **Fig. 6** SEM observations of the alkali activated fly ash binder F100 at 28 days: (A) SEM
 383 micrograph, and chemical mappings of: (B) silicon, (C) calcium and (D) sulphur.

384

385 Figure 6 shows the alkali activated fly ash binder at 28 days, and more particularly a
 386 calcium-rich reactive nodule labelled 1 surrounded by a dense matrix comprising both
 387 new products and non-reactive phases such as quartz or aluminium containing minerals.
 388 However, in that case the extent of dissolution of the calcium nodule appears lower as the
 389 hollowed structure is not seen but rather a granular microstructure similar of those
 390 observed after 24 hours. Chemical mappings show that the dissolution of that nodule did
 391 start as calcium is widely diffused into the matrix, and an enrichment in sulphur is once
 392 again seen in the outer part of the nodule. Nevertheless, the dissolution is at a different
 393 stage as calcium is still strongly detected in the centre of the nodule and no hollowed
 394 structure is noticed. Consequently, the extent of reaction of a calcium-rich nodule varies

1 395 locally. A lesser porosity of the calcium nodule could for instance moderates its
2
3 396 dissolution. Its size, its content in calcium and sulphur or else the amount of water locally
4
5 397 available are also all parameters that may locally affect the extent of reaction.
6
7
8 398



400 **Fig. 7** Comparing SEM microstructural changes of the alkali activated fly ash binder F100
401 at 28 days around: (A) a calcium-rich nodule labelled C, and (B) a particle from the
402 vitreous phase labelled G; M1 = dense matrix; M2 = porous matrix
403

404 Figure 7 shows micrographs of the alkali activated binder after 28 days, and more
405 particularly the difference between microstructural changes occurring (A) around a
406 calcium rich particle identified as the dark reactive zones in optical microscopy, and
407 around a glassy particle identified as the brown matrix in optical microscopy.

408 It is worth noting that although amorphous and extremely porous the vesicular glassy
409 phases reaction is negligible as its vesicular structure remains similar to the one after 24
410 hours (see Figure 4A, particle labelled 1). This observation is in accordance with our
411 previous study about the physicochemical evolution of that system which shows that the
412 vitreous phase mainly remains unreactive (Coudert et al., 2019). It is well known that the
413 rate of reaction of the aluminosilicate vitreous phases of fly ash at ambient temperature
414 following alkaline activation is slow and takes several days (Provis and Deventer, 2009;
415 Wardhono et al., 2015). Whereas the calcium-rich particles in our mixes are extremely

1 416 and quickly reactive as the formation of new products containing calcium already starts
2
3 417 after 24 hours as seen previously in Figure 3. Hence, the faster reaction of calcium-rich
4
5 418 particles leads to the formation of dense products (as seen in Figure 7A) freezing the
6
7
8 419 system and preventing the later reaction of the aluminosilicate glassy phases.
9

10 420 Massive and dense areas are observed around calcium-rich nodules (see Figure 7A), while
11
12 421 a more porous matrix is seen around vesicular glassy phases (see Figure 7B). The
13
14 422 comparison in Figure 7 hence evidences that there are different matrices forming the
15
16 423 alkali activated treated soil: (i) a first circularly-shaped matrix identified around calcium-
17
18 424 rich particles and presenting a high density labelled M1 on Figure 7A, and (ii) a more
19
20 425 porous matrix less bonded labelled M2 on Figure 7A&B whose pores are shown by red
21
22 426 arrows, and located around glassy phases of lower reactivity. A previous investigation of
23
24 427 that system by Nuclear Magnetic Resonance showed the signature of only one type of
25
26 428 silicate chains combined with calcium and spreaded into the matrix as a new compound
27
28 429 (Coudert et al., 2019). Therefore, Scanning Electron Microscopy provides an additional
29
30 430 information: although the atomic structure of the silicate chain remains similar, the
31
32 431 arrangement of those phases in the matrix varies following the local environment.
33
34 432 Similarly to the great heterogeneity of fly ash, the matrix formed is also highly
35
36 433 heterogeneous.
37
38
39
40
41
42
43
44
45
46

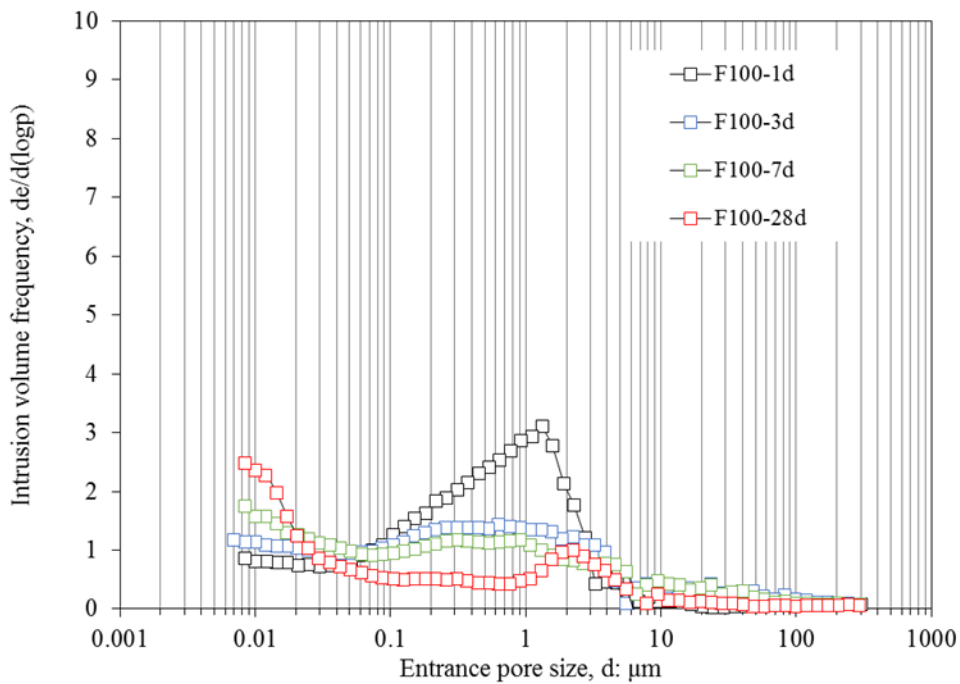
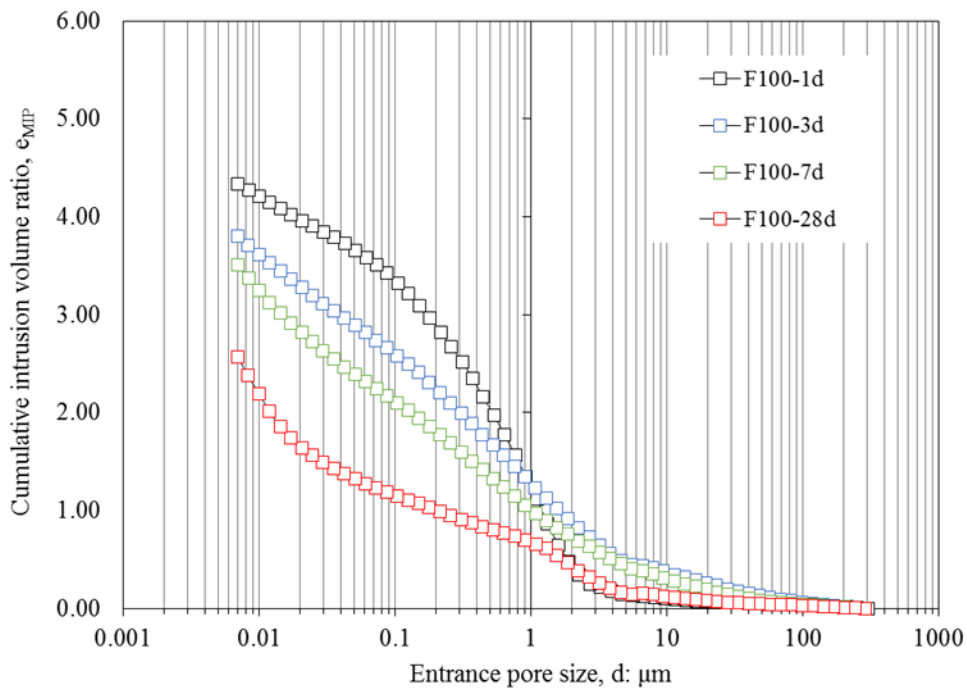
47 3.2.3 Mercury Intrusion Porosimetry (MIP)

48
49 436 Figure 8A shows cumulative curves of mercury intrusion porosimetry tests of the alkali
50
51 437 activated fly ash binder over time. The longer the curing time, the lower is the cumulative
52
53 438 intrusion volume ratio implying a progressive decrease of the overall porosity over time,
54
55 439 and in accordance with the general tendencies observed by SEM in section 3.2.2. It is
56
57
58
59
60
61
62
63
64
65

1 440 owed to the progressive filling of pores by the new compounds formed i.e. calcium-
2
3 441 silicate two-dimensional chains and thenardite.
4

5
6 442 Figure 8B shows the frequency distributions of pore entrance diameters belonging to the
7
8 443 alkali activated fly ash binder over time. Samples at 24 hours, 3 and 7 days all show one
9
10 444 broad modal pore sizes between 0.05 μm and 3 μm . However, from 24 hours to 7 days
11
12 445 the frequency of those pores progressively decreases due to their filling by newly formed
13
14 446 compounds. Whereas, at 28 days a narrower modal pore size at about 2 μm is observed.
15
16 447 By analogy with SEM pictures, those remaining pores at 2 μm could correspond to either
17
18 448 the size of the cracks seen around calcium particles and associated with shrinkage as
19
20 449 previously observed on Figure 5, the porosity formed within calcium nodules after their
21
22 450 dissolution also seen on Figure 5, or else pores that have not been filled by new
23
24 451 compounds within the more porous matrix previously identified and labelled M2 on
25
26 452 Figure 7.
27
28
29
30
31

32 453 Finally, in the area of lower pore size i.e. below 20 nm the increase of frequency over
33
34 454 time corresponds to the formation of a new class of pores inside the matrix. It is associated
35
36 455 with the formation of the silicate two-dimensional chains combined with calcium, whose
37
38 456 structure resembles those of Calcium-Silicate Hydrates (i.e. C-S-H phases commonly
39
40 457 found in Portland cement) known for possessing an intrinsic porosity of a nanometer size
41
42 458 (Muller, 2014). However, this small new class of pores cannot be fully probed by MIP
43
44 459 technique whose detection limit in the small entrance pore size is of 7 nm.
45
46
47
48
49
50
51
52
53
54
55
56
57
58
59
60
61
62
63
64
65



460

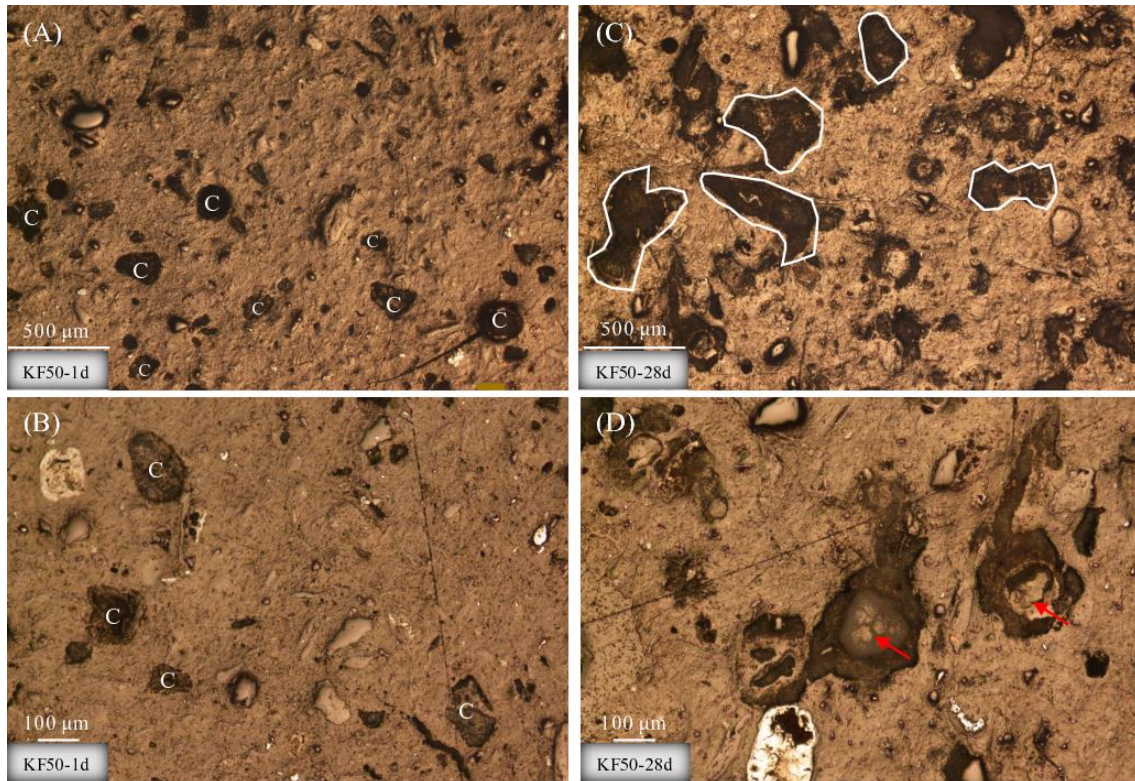
461 **Fig. 8** Comparing mercury intrusion porosimeter tests of the alkali activated fly ash binder
 462 F100 over time and in terms of (A) cumulative intrusion volume ratios, (B) intrusion
 463 volume frequency ratios as a function of entrance pore size.

464

465

466 *3.3 Interaction between the alkali activated fly ash binder and kaolin*

1 467 The following section aims at understanding the interaction between kaolin and the alkali
2
3 468 activated fly ash binder previously described. Our former study focussing on the
4
5
6 469 physicochemical evolution of the same mixes herein studied showed that kaolin was not
7
8 470 reactive during alkaline activation and did not modify the reaction sequence when
9
10 471 compared to the one of the alkali activated fly ash binder alone (Coudert et al., 2019).
11
12 472 Accordingly, similar mechanisms of ions dissolution precipitation from the calcium-rich
13
14 473 particles into the matrix leading to the formation of new products also occur in the alkali
15
16 474 activated fly ash binder treated soil as previously described for the binder in section 3.2.2,
17
18 475 and hence will not be detailed here.
19
20
21 476 Regarding the pore network structure, our previous study also showed that kaolinite
22
23 477 platelets were homogeneously spread across the matrix. This section consequently aims
24
25 478 at giving a deeper insight of the influence of kaolin on the microstructure with respect to
26
27 479 the binder alone.
28
29
30 480 Figure 9 shows microstructural observations of the alkali activated fly ash binder treated
31
32 481 soil over time by optical microscopy. Similarly, to the alkali activated fly ash binder, after
33
34 482 24 hours of curing, dispersed dark spots corresponding to calcium-rich nodules are seen
35
36 483 across the overall sample, whereas at 28 days larger dark zones encompassing the newly
37
38 484 formed compounds have grown around those nodules. Hollowed greyish nodule
39
40 485 structures at 28 days can also be distinguished as for the binder and associated with the
41
42 486 dissolution of calcium-rich particles.
43
44
45
46
47
48
49
50 487



488

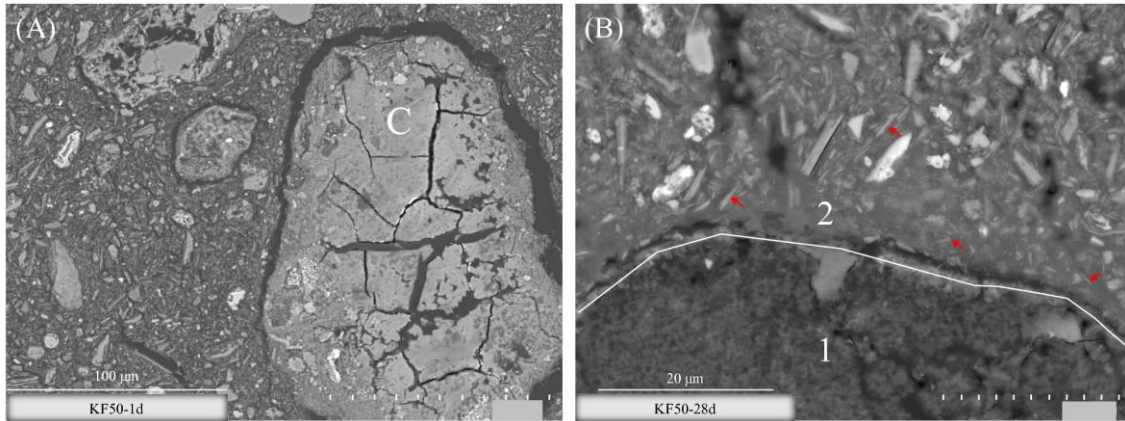
489 **Fig. 9** Optical microscopy images of the alkali activated fly ash binder treated soil KF50
 490 (A) and (B) after 24 hours, (C) and (D) at 28 days, C=calcium-rich particle.
 491

492 The widening of darker zones which indicates the extent of reaction is lesser than the
 493 binder and represents around $\frac{1}{4}$ of the sample. This is consistent with the proportions of
 494 aluminosilicate solid considering that half of fly ash containing the reactive calcium
 495 nodules has been replaced by non-reactive kaolin in this soil-binder mixture.
 496 Consequently, the growth and development of new products into the available spaces
 497 does not seem influenced by the presence of kaolin.

498 Figure 10 shows micrographs of the alkali activated binder treated soil. After 24 hours
 499 crackings around and inside calcium nodules are seen (see particle C on Figure 10A), and
 500 associated to shrinkage similarly to the alkali activated fly ash binder at 28 days. The
 501 treated soil at 28 days however shows less marked crackings as shown on Figure 10B
 502 which focusses on the interface between a calcium-rich nodule labelled 1 and the

1 503 surrounding dense matrix labelled 2. It is attributed to the presence of kaolinite acting as
2
3 504 a filler at the periphery of the calcium-rich nodules (see red arrows on Figure 10B
4
5
6 505 showing kaolinite platelets).

7
8 506



24 507

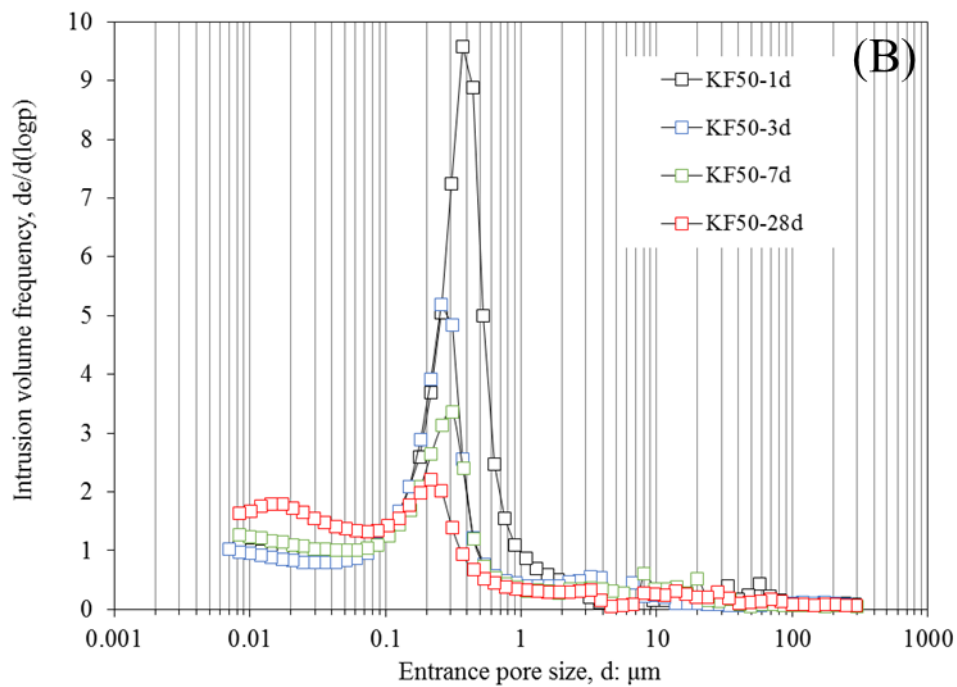
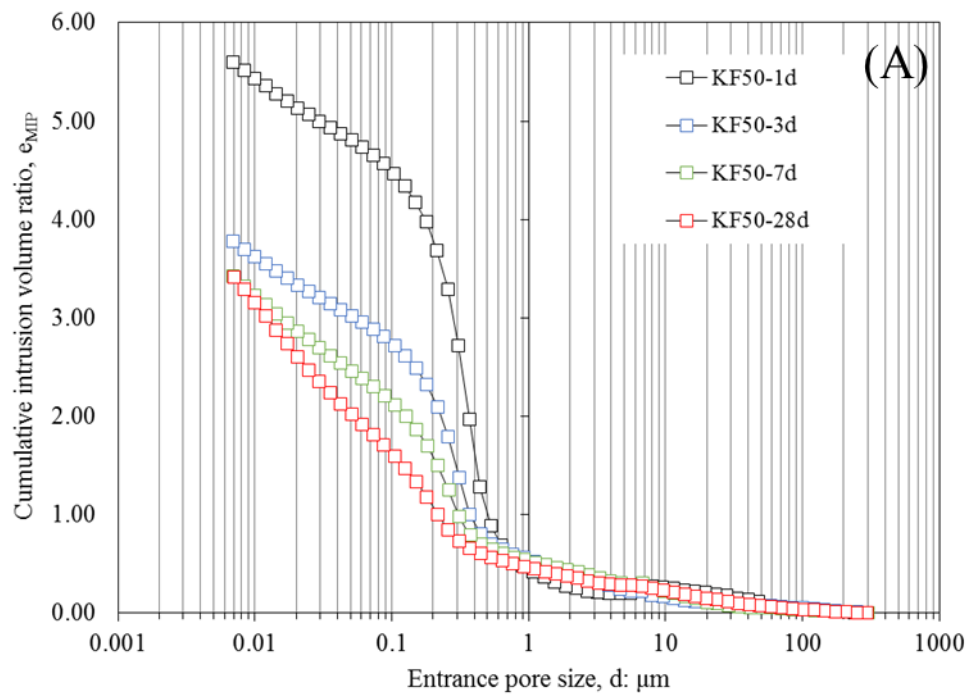
26 508 **Fig. 10** SEM micrographs of the alkali activated fly ash binder treated soil KF50 at (A)
27 509 24 hours and (B) 28 days.

28 510

31 511 Figure 11A shows cumulative curves of mercury intrusion porosimetry tests of the alkali
32
33 512 activated fly ash binder treated kaolin over time. Similarly to what was observed for the
34
35 513 alkali activated binder, a decrease of the total porosity is detected over time.

38 514 Figure 11B shows the frequency distributions of pore entrance diameters belonging to the
39
40 515 treated soil over curing time. Similarly to the alkali activated fly ash binder, the treated
41
42 516 soil at 24 hours shows one modal pore sizes. Nevertheless, compared to the binder it is
43
44 517 associated with a lower entrance pore size value around 0.4 μm and a much thinner peak.

48 518 The non-presence of a wide class of pores between 0.05 μm and 3 μm at 24 hours as seen
49
50 519 for the alkali activated fly ash binder is associated with the filling of the spaces between
51
52 520 the coarse grains of fly ash by the small sized kaolinite platelets. At 24 hours, kaolin
53
54 521 therefore leads the organisation of the system microstructure as the typical pattern of
55
56 522 kaolin (i.e. a monomodal curve with a peak around 0.4 μm) is shaping the curve.



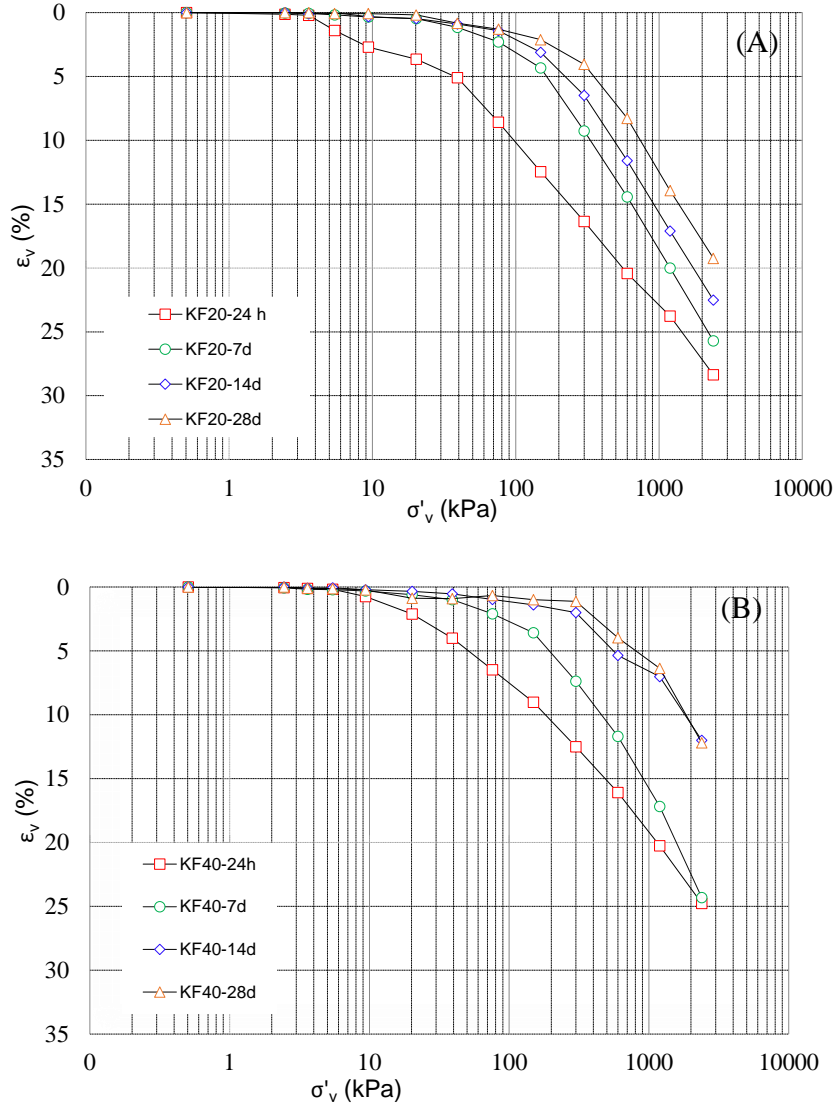
523

524 **Fig. 11** Comparing mercury intrusion porosimeter tests of the alkali activated fly ash
 525 binder treated soil KF50 over time and in terms of (A) cumulative intrusion volume ratios,
 526 (B) intrusion volume frequency ratios as a function of entrance pore size.

527

1 528 Increasing the curing time, the filling of largest pores around the peak is seen as for the
2
3 529 binder and due to the progressive filling of those pores by the newly products formed. A
4
5
6 530 little shift of the residual peak towards smaller entrance diameters is also observed.
7
8 531 Finally, the formation of a new class of pores in the area of lower pore size i.e. below 30
9
10 532 nm is observed between 7 and 28 days of curing. Similarly to the binder, it is associated
11
12 533 with the intrinsic porosity of the newly formed silicate-calcium chains. The delay in
13
14 534 detection compared to the binder is due to the lower amount of phases formed for that
15
16 535 system.
17
18 536 Figure 12 shows the results of one dimensional compression tests on KF20 and KF40
19
20 537 treated samples at increasing curing times, namely 24h, 7, 14 and 28 days. Addition of
21
22 538 alkali activated binder induces an overall reduction of compressibility of the treated
23
24 539 samples, with reduced volume strains for reference vertical stresses. The reduction is
25
26 540 more relevant for increasing curing times, showing the stiffer behaviour of the treated
27
28 541 sample. Coupled with the reduction of compressibility, an increase of yield stress of the
29
30 542 samples is observed. The transition from a reversible behaviour to an irreversible one is
31
32 543 shifted (yield stress) to higher vertical stresses. The shift is more relevant for higher
33
34 544 amount of binder and at increasing curing time, revealing the reactivity of the binder to
35
36 545 promote an improvement of the mechanical response of the treated soil. For stress levels
37
38 546 higher than yield stress, treated samples show a higher compressibility coefficient (i.e.
39
40 547 slope of the compressibility curve), depending on the destructure stage induced by
41
42 548 load increase, more evident for longer curing times and higher binder content. As a
43
44 549 confirmation, in Figure 13 the compressive behaviour of treated samples is reported as
45
46 550 function of binder contents. Sample prepared at 10%, 20% and 40% of alkali activated
47
48 551 fly ash and cured for 24 hours before testing show a progressive improvement mainly
49
50
51
52
53
54
55
56
57
58
59
60
61
62
63
64
65

1 552 related to the amount of new compounds forming over time. Compressibility curves show
 2
 3 553 a reduction of compressibility evidenced by the relevant decrease of volume strains and
 4
 5
 6 554 an increase yield stresses of the treated samples, whose extent depends on binder content.



555
 556
 557 **Fig. 12** One dimensional compression curves of alkali activated binder treated samples at
 558 24 h, 7, 14 and 28 days of curing: (A) KF20; (B) KF40.
 559

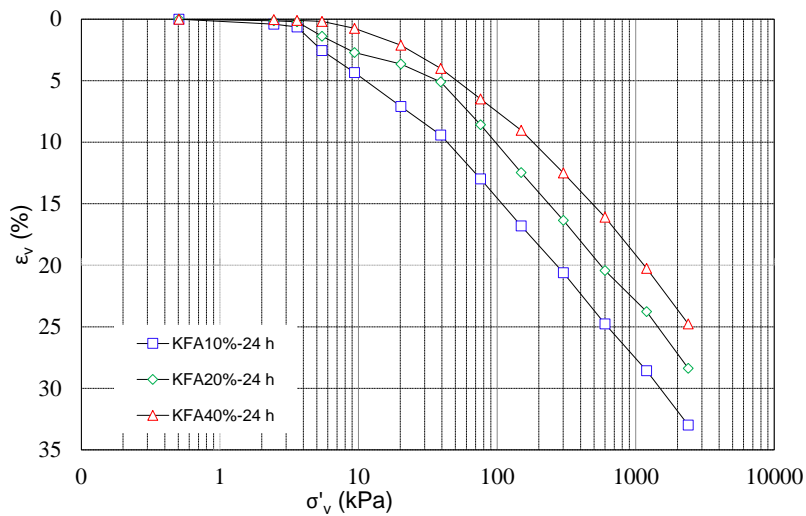


Fig. 13 One dimensional compression curves of treated samples as function of binder contents (i.e. KF10, KF20, KF40) at 24 hours of curing.

3.4 Comparison with Portland cement

This last section focusses on a comparison with microstructural development in Portland cement for which the mechanisms involved appear alike. This comparison particularly helps at providing a better understanding of (i) how microstructures are formed and (ii) interpreting the short and long-term performances of the treated soil regarding the evolution of the binder over time. At macroscopic level, the effectiveness of alkali activated binder soil treatment has been highlighted by comparison with mechanical performance induced by Portland cement.

3.4.1 Processes generating the microstructure

In cement systems, the dissolution of cement particles releases ions into the pore solution which then combine with water to form mainly Calcium Silicate Hydrates C-S-H (Muller, 2014). In a similar way, in our alkali activated binder, the dissolution of calcium-rich particles from fly ash releases calcium cations into the pore solution which then combine with water and silicon anions from the alkaline solution to form silicate two-

1 579 dimensional chains combined with calcium. A former investigation by Nuclear Magnetic
2
3 580 Resonance nevertheless showed that the chains structure is slightly different from C–S–
4
5
6 581 H, namely they are not well organized, of high length and may incorporate aluminum in
7
8 582 a three dimensional environment which has not been described in literature yet (Coudert
9
10 583 et al., 2019).

11
12
13 584 Secondly, it was reported for cement systems that the first Calcium Silicate Hydrates C–
14
15 585 S–H cover cement grains and further grow into the available space. All cement grains are
16
17
18 586 therefore surrounded by a shell of C–S–H (Scrivener, 2004). Again similarly in this study,
19
20 587 optical microscopy images clearly show the development and growth of new products
21
22 588 around calcium-rich reactive particles suggesting a similar mechanism.

23
24
25 589 Furthermore, Scrivener (2004) shows that as the cement grains dissolve, this might leave
26
27 590 a hollow shell (Scrivener, 2004). The various extent of reaction of individual cement
28
29 591 grains depends on their sizes: small cement grains hydrate completely in the first stages
30
31
32 592 and remain as hollow shells of hydration product; whereas big grains further hydrate
33
34
35 593 which forms denser hydration products and which fill in the gap between shell and grain
36
37 594 (Muller, 2014). In this study it is also noticeable that calcium-rich reactive phases react
38
39 595 at different rates: some completely dissolve after 28 days leaving a hollow shell while
40
41
42 596 other remain with their initial structure and still contain calcium. Consequently, and
43
44
45 597 similarly to what is described in the literature, depending on the calcium nodule size, the
46
47 598 local products formed slightly differ which could lead to local variation of the inherent
48
49 599 material properties.

50
51
52 600

53
54 601 *3.4.2 Pore network characteristics*
55
56
57
58
59
60
61
62
63
64
65

1 602 Regarding the pore network characteristics of cement systems, two populations of pores
2
3 603 are generally distinguished: (i) capillary pores which correspond to space not being filled
4
5 604 by solid products of hydration, and (ii) small pores called gel pores associated to the
6
7
8 605 intrinsic porosity of Calcium Silicate Hydrates C-S-H. Over time, while chemical
9
10 606 reactions proceed the population of capillary pores decreases whereas the population of
11
12 607 gel pores increases, which may lead to the formation of disconnected spaces (Jennings et
13
14 608 al., 2008). Our alkali activated binder shows similar tendencies that is a progressive
15
16 609 decrease of intermediate pores or capillary pores while a new class of pores associated
17
18 610 with silicate-calcium chain products is detected using Mercury Intrusion Porosimetry.
19
20
21
22
23
24

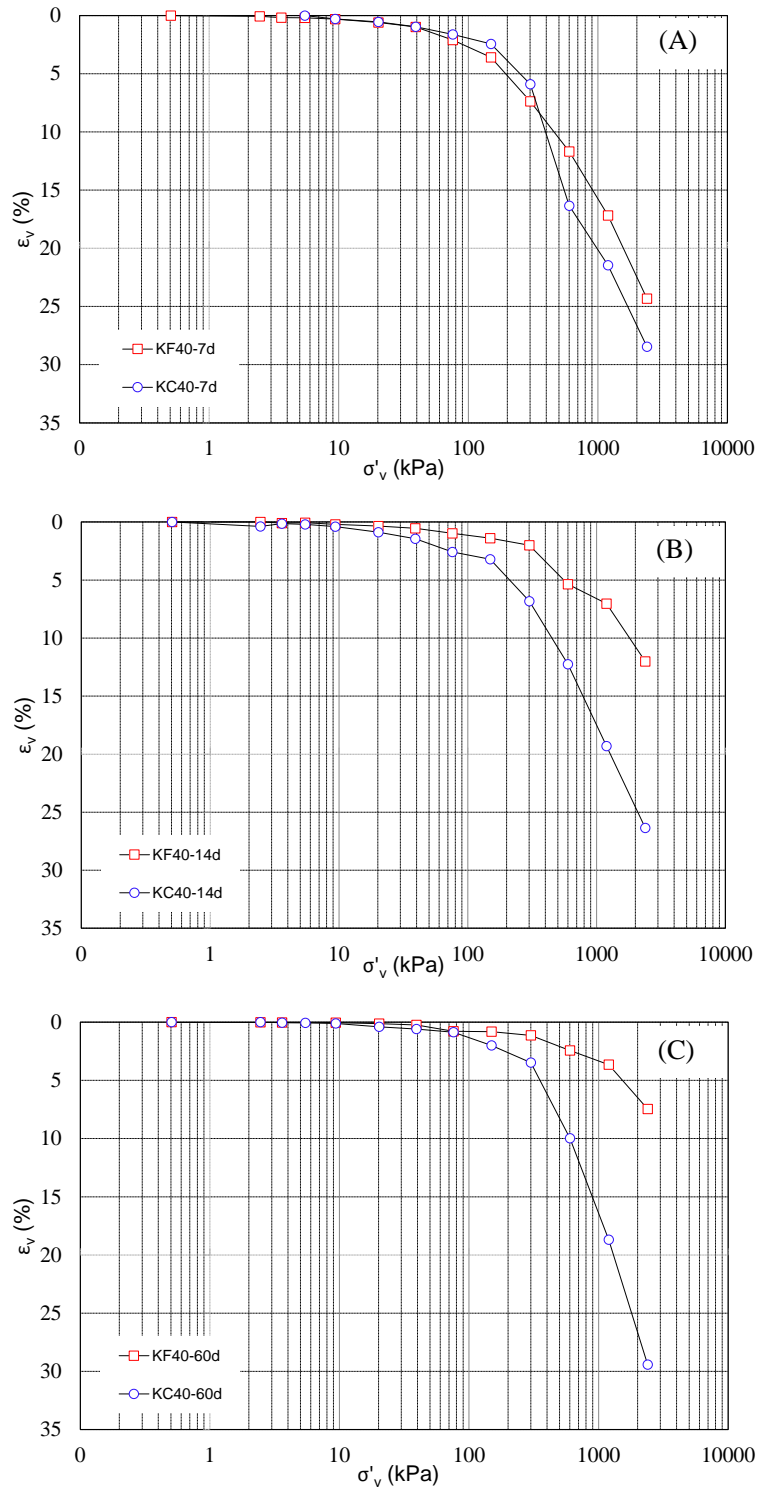
25 612 *3.4.3 Macroscopic behaviour according to the microstructure evolution*

26
27 613 Since both the processes generating the microstructure and the evolution of the pore
28
29 614 network over time of our alkali activated binder are similar to cement systems, a similar
30
31 615 influence of the microstructure on the short and long-term performances can be expected.
32
33 616 Changes in the pore network strongly influence transport properties that govern the rate
34
35 617 of all major deterioration processes and the service life of building materials (Wong et
36
37 618 al., 2006). Namely the formation of gel pores inside the capillary spaces tends to decrease
38
39 619 the connectivity of the pore network inhibiting the transport of aggressive substances such
40
41 620 as acids, carbonate or chloride through concrete and therefore enhancing the material
42
43 621 durability (van Deventer et al., 2010; Muller, 2014).
44
45
46
47
48

49 622 Finally, despite the great inhomogeneity of the reactive fly ash the growth and widening
50
51 623 of new products appear to occur homogeneously across the sample at a millimetric scale
52
53 624 in our alkali activated materials which would benefit the formation of a homogeneously
54
55 625 reinforced material.
56
57
58
59
60
61
62
63
64
65

1 626 At volume scale of the sample, a comparison between the mechanical performance
2
3 627 induced by alkali activated binder (KF40) and by ordinary Portland cement (KC40) is
4
5 628 shown in Figure 14 for samples prepared with the same binder content and cured for 7,
6
7 629 14 and 60 days. No relevant changes in the compressibility curves are observed for KF40
8
9 630 and KC40 samples cured for 7 days before testing (Figure 14A). For longer curing times,
10
11 631 results show a higher compressibility reduction and yield stress increase for KF40 treated
12
13 632 samples compared to cement treated samples (Figures 14B and 14C). The post-yield
14
15 633 behaviour induced by ordinary Portland cement shows the highest slope of the
16
17 634 compressibility curve, highlighting a more evident destructuration stage for cement
18
19
20
21
22
23 635 treated samples at increasing vertical stresses.
24
25
26
27
28
29
30
31
32
33
34
35
36
37
38
39
40
41
42
43
44
45
46
47
48
49
50
51
52
53
54
55
56
57
58
59
60
61
62
63
64
65

1
2
3
4
5
6
7
8
9
10
11
12
13
14
15
16
17
18
19
20
21
22
23
24
25
26
27
28
29
30
31
32
33
34
35
36
37
38
39
40
41
42
43
44
45
46
47
48
49
50
51
52
53
54
55
56
57
58
59
60
61
62
63
64
65



636

637 **Fig. 14** One dimensional compression curves of treated samples as function of binder
 638 type (i.e. KF40 vs. KC40): (A) 7 days of curing; (B) 14 days of curing; (C) 60 days of
 639 curing

640

641

1 642 **3 Conclusions**

2
3 643 The development of a novel binder that is an alkali activated calcium-rich fly ash for clay
4
5
6 644 soil stabilisation was investigated. The study of its microstructural evolution showed that
7
8 645 structural changes occur around calcium-bearing minerals from fly ash which constitute
9
10
11 646 the reactive phases, and whose dissolution leads to the formation of new compounds on
12
13 647 its surface first and then growing into the available space. Capillary pore spaces are
14
15 648 progressively filled by new compounds (i.e thernadite and silicate-calcium chains) over
16
17
18 649 time. Whereas the newly formed silicate-calcium chains possess an intrinsic porosity of
19
20
21 650 nanometric size conducting to the formation of a new class of small pores over time.
22
23 651 Different heterogenous matrices of various porosity and arrangement are however
24
25 652 observed across the material and owed to the high heterogeneity of fly ash whose particles
26
27
28 653 locally react differently.

29
30 654 The interaction between the binder and kaolin showed that small sized kaolinite platelets
31
32 655 fill the spaces between coarser grains from fly ash. Kaolin is therefore leading the
33
34
35 656 microstructural organisation, that is, the pore network is characterised by pores ranging
36
37
38 657 in lower size compared to the binder. Nevertheless, the microstructural changes remain
39
40 658 similar over time i.e. filling of capillary pores and appearance of nanometric pores from
41
42 659 silicate-calcium chains.

43
44
45 660 One-dimensional compression tests performed on treated sample highlighted the
46
47 661 effectiveness of alkali activated binders to promote an improvement of the mechanical
48
49
50 662 behaviour of treated soil. A reduction of compressibility and increase of the yield stress
51
52 663 soil was observed since the very short term.

53
54 664 The observed microstructural evolution is similar to the one of cement system and should
55
56
57 665 therefore conduct to akin performances that is an increase in strength and ability to resist

1 666 to aggressive substances due to changes in transport properties. It has been confirmed by
2
3 667 observing the similarities of the mechanical performance of alkali activated binder treated
4
5 668 samples with cement treated ones for short curing time. A marked improvement of the
6
7
8 669 mechanical behaviour of soil is induced by alkali activated binder starting from 14 days
9
10
11 670 of curing, representing a viable sustainable alternative to the use of ordinary stabilizing
12
13 671 agent for soil improvement.

14
15 672 However, regarding the complexity of both cement and alkali activated systems which
16
17
18 673 are multi-components systems, a coupling of those microstructural observations with
19
20
21 674 mechanical performances and transport properties is of further interest. Namely, a
22
23 675 complementary three-dimensional characterisation of the pore network using for instance
24
25 676 microtomography would greatly help to assess the connectivity and tortuosity of the pore
26
27
28 677 network which are primordial parameters to understand properly transport properties and
29
30 678 therefore durability. Using micro-indentation coupled with Scanning Electron Imaging
31
32
33 679 would also allow to measure local hardness variations following the extent of reaction of
34
35 680 calcium particles and therefore help to apprehend how significant are the local
36
37
38 681 microstructural variations for the mechanical performances at a macroscopic scale.

39
40 682

41 42 683 **Acknowledgements**

43
44
45 684 The authors wish to acknowledge the support of the European Commission via the Marie
46
47 685 Skłodowska-Curie Innovative Training Networks (ITN-ETN) project TERRE 'Training
48
49
50 686 Engineers and Researchers to Rethink geotechnical Engineering for a low carbon future'
51
52 687 (H2020-MSCA-ITN-2015-675762).

53
54
55 688

56 57 689 **References**

1 690 Askeland, D.R., Fulay, P.P., Wright, W.J., 2011. The science and engineering of
2
3 691 materials, 6th ed. ed. Cengage Learning, Stamford, CT.
4
5 692 Basha E.A., Hashim R., Muntohar A., 2003. Effect of the cement-rice husk ash on the
6
7 693 plasticity and compaction of soil, *Electron. J. Geotech. Eng.* 8.
8
9 694 Buchwald, A., Kaps, C., Hohmann, M., 2003. Alkali-activated binders and pozzolan
10
11 695 cement binders—complete binder reaction or two sides of the same story, in: *Proceedings*
12
13 696 *of the 11th International Conference on the Chemistry of Cement. Portland Cement*
14
15 697 *Association Durban, South Africa*, pp. 1238–1246.
16
17 698 Chemed, Y., 2015. Effect of hydrated lime on kaolinite surface properties and its
18
19 699 rheological behaviour. *Université de Nantes*.
20
21 700 Clemens, H., Mayer, S., Scheu, C., 2008. Microstructure and Properties of Engineering
22
23 701 Materials. *Neutrons Synchrotron Radiat. Eng. Mater. Sci. Fundam. Appl.* 1–20.
24
25 702 Coudert, E., Paris, M., Deneele, D., Russo, G., Tarantino, A., 2019. Use of alkali activated
26
27 703 fly ash binder for kaolin clay soil stabilisation: Physicochemical evolution. *Constr. Build.*
28
29 704 *Mater.* 201 (2019) 539–552, <https://doi.org/10.1016/j.conbuildmat.2018.12.188>
30
31 705 Cristelo, N., Glendinning, S., Fernandes, L., Pinto, A.T., 2012. Effect of calcium content
32
33 706 on soil stabilisation with alkaline activation. *Constr. Build. Mater.* 29, 167–174.
34
35 707 <https://doi.org/10.1016/j.conbuildmat.2011.10.049>
36
37 708 Cristelo, N., Glendinning, S., Teixeira Pinto, A., 2011. Deep soft soil improvement by
38
39 709 alkaline activation. *Proc. Inst. Civ. Eng. - Ground Improv.* 164, 73–82.
40
41 710 <https://doi.org/10.1680/grim.900032>
42
43 711 Duxson P, Provis JL, Lukey GC, Van Deventer JS, 2007. The role of inorganic polymer
44
45 712 technology in the development of ‘green concrete’. *Cem. Concr. Res.* 2007; 37:1590–7
46
47 713 Fang, G., Bahrami, H., Zhang, M., 2018. Mechanisms of autogenous shrinkage of alkali-
48
49
50
51
52
53
54
55
56
57
58
59
60
61
62
63
64
65

1 714 activated fly ash-slag pastes cured at ambient temperature within 24 h. *Constr. Build.*
2
3 715 *Mater.* 171, 377–387. <https://doi.org/10.1016/j.conbuildmat.2018.03.155>
4
5 716 James J., Pandian P.K., 2016. Industrial wastes as auxiliary additives to cement/lime
6
7
8 717 stabilization of soils, *Adv. Civ. Eng.* 2016 1–17.
9
10 718 Jennings, H.M., Bullard, J.W., Thomas, J.J., Andrade, J.E., Chen, J.J., Scherer, G.W.,
11
12
13 719 2008. Characterization and Modeling of Pores and Surfaces in Cement Paste:
14
15 720 Correlations to Processing and Properties. *J. Adv. Concr. Technol.* 6, 5–29.
16
17 721 Lawrence, M., Jiang, Y., 2017. Porosity, Pore Size Distribution, Micro-structure, in:
18
19 722 Amziane, S., Collet, F. (Eds.), *Bio-Aggregates Based Building Materials*. Springer
20
21 723 Netherlands, Dordrecht, pp. 39–71. https://doi.org/10.1007/978-94-024-1031-0_2
22
23 724 McLellan BC, Williams RP, Lay J, Van Riessen A, Corder GD., 2011. Costs and carbon
24
25 725 emissions for geopolymer pastes in comparison to Ordinary Portland Cement. *J. Clean*
26
27 726 *Prod* 2011; 19:1080–90
28
29 727 Muller, A.C.A., 2014. Characterization of porosity & CSH in cement pastes by 1H NMR.
30
31 728 École Polytechnique Fédérale de Lausanne, Suisse.
32
33 729 Nalbantoğlu Z., 2004. Effectiveness of class C fly ash as an expansive soil stabilizer,
34
35 730 *Constr. Build. Mater.* 18, 377–381.
36
37 731 Nath, S.K., Maitra, S., Mukherjee, S., Kumar, S., 2016. Microstructural and
38
39 732 morphological evolution of fly ash based geopolymers. *Constr. Build. Mater.* 111, 758–
40
41 733 765. <https://doi.org/10.1016/j.conbuildmat.2016.02.106>
42
43 734 Provis, J.L., Deventer, J.S.J. va., 2009. *Geopolymers Structure, processing, properties*
44
45 735 and industrial applications, Woodhead Publishing in materials. Woodhead, Cambridge.
46
47 736 Rios, S., Cristelo, N., Viana da Fonseca, A., Ferreira, C., 2016. Structural Performance
48
49 737 of Alkali-Activated Soil Ash versus Soil Cement. *J. Mater. Civ. Eng.* 28, 4015125.
50
51
52
53
54
55
56
57
58
59
60
61
62
63
64
65

1 738 [https://doi.org/10.1061/\(ASCE\)MT.1943-5533.0001398](https://doi.org/10.1061/(ASCE)MT.1943-5533.0001398)
2
3 739 Sargent, P., 2015. The development of alkali-activated mixtures for soil stabilisation. In
4
5 740 Handbook of alkali-activated cements, mortars and concretes (pp. 555-604). Woodhead
6
7 741 Publishing
8
9 742 Scrivener, K.L., 2004. Backscattered electron imaging of cementitious microstructures:
10
11 743 understanding and quantification. *Cem. Concr. Compos.* 26 8 935–945.
12
13 744 Scrivener, K.L., Kirkpatrick, R.J., 2008. Innovation in use and research on cementitious
14
15 745 material. *Cem. Concr. Res.* 38, 128–136.
16
17 746 <https://doi.org/10.1016/j.cemconres.2007.09.025>
18
19 747 Shi, C., Krivenko, P.V., Roy, D.M., 2006. Alkali-activated cements and concretes. Taylor
20
21 748 & Francis, London ; New York.
22
23 749 Silva, R.A., Oliveira, D.V., Miranda, T., Cristelo, N., Escobar, M.C., Soares, E., 2013.
24
25 750 Rammed earth construction with granitic residual soils: The case study of northern
26
27 751 Portugal. *Constr. Build. Mater.* 47, 181–191.
28
29 752 <https://doi.org/10.1016/j.conbuildmat.2013.05.047>
30
31 753 Singhi, B., Laskar, A.I., Ahmed, M.A., 2016. Investigation on Soil–Geopolymer with
32
33 754 Slag, Fly Ash and Their Blending. *Arab. J. Sci. Eng.* 41, 393–400.
34
35 755 <https://doi.org/10.1007/s13369-015-1677-y>
36
37 756 Tenn, N., Allou, F., Petit, C., Absi, J., Rossignol, S., 2015. Formulation of new materials
38
39 757 based on geopolymer binders and different road aggregates. *Ceram. Int.* 41, 5812–5820.
40
41 758 <https://doi.org/10.1016/j.ceramint.2015.01.010>
42
43 759 United Nations, 2004. A More Secure World: Our Shared Responsibility. Report of the
44
45 760 Secretary-General's High-level Panel on Threats, Challenges and Change, 2004.
46
47 761 van Deventer, J.S.J., Provis, J.L., Duxson, P., Brice, D.G., 2010. Chemical Research and
48
49
50
51
52
53
54
55
56
57
58
59
60
61
62
63
64
65

1 762 Climate Change as Drivers in the Commercial Adoption of Alkali Activated Materials.
2
3 763 Waste Biomass Valorization 1, 145–155. <https://doi.org/10.1007/s12649-010-9015-9>
4
5
6 764 van Deventer, J.S.J., San Nicolas, R., Ismail, I., Bernal, S.A., Brice, D.G., Provis, J.L.,
7
8 765 2015. Microstructure and durability of alkali-activated materials as key parameters for
9
10
11 766 standardization. J. Sustain. Cem.-Based Mater. 4, 116–128.
12
13 767 <https://doi.org/10.1080/21650373.2014.979265>
14
15
16 768 Vitale E., Russo G., Deneele D. 2019. Multi-scale analysis on soil improved by alkali
17
18 769 activated binders. E3S Web of Conferences 92, 11003 (2019) - IS-Glasgow 2019;
19
20 770 <https://doi.org/10.1051/e3sconf/20199211003>
21
22
23 771 Vitale E., Marocco A., Khatib M., Russo G. 2020a. Hydro-mechanical behaviour of
24
25 772 alkali-activated binder treated soil. E3S Web of Conferences 195, 06003 (2020) – E-
26
27 773 UNSAT 2020; <https://doi.org/10.1051/e3sconf/202019506003>
28
29
30 774 Vitale E., Russo G., Deneele D. 2020b. Use of Alkali-Activated Fly Ashes for Soil
31
32 775 Treatment. Geotechnical Research for Land Protection and Development. CNRIG 2019.
33
34 776 Lecture Notes in Civil Engineering, vol 40. Springer
35
36
37 777 Vitale, E., Russo, G., Dell’Agli, G., Ferone, C., and Bartolomeo, C. 2017. Mechanical
38
39 778 behaviour of soil improved by alkali activated binders. Environments 4(4), 80.
40
41 779 <https://doi.org/10.3390/environments4040080>
42
43
44 780 Wardhono, A., Law, D.W., Strano, A., 2015. The Strength of Alkali-activated Slag/fly
45
46 781 Ash Mortar Blends at Ambient Temperature. Procedia Eng. 125, 650–656.
47
48 782 <https://doi.org/10.1016/j.proeng.2015.11.095>
49
50
51 783 Wilkinson, A., Haque, A., Kodikara, J., 2010. Stabilisation of clayey soils with industrial
52
53 784 by-products: part A. Proc. Inst. Civ. Eng. - Ground Improv. 163, 149–163.
54
55 785 <https://doi.org/10.1680/grim.2010.163.3.149>
56
57
58
59
60
61
62
63
64
65

1 786 Wong, H.S., Buenfeld, N.R., Head, M.K., 2006. Estimating transport properties of
2
3 787 mortars using image analysis on backscattered electron images. *Cem. Concr. Res.* 36,
4
5 788 1556–1566.
6
7
8 789 Xi F., Davis S. J., Ciaias P., Crawford-Brown D., Guan D., Pade C., Shi T., Syddall M.,
9
10 790 Lv J., Ji L., Bing L., Wang J., Wei W., Yang K.-H., Lagerblad B., Galan I., Andrade C.,
11
12 791 Zhang Y., Liu Z. 2016. Substantial global carbon uptake by cement carbonation, *Nature*
13
14 792 *Geoscience*, 9, 12-2016
15
16 793 Zhang Z, Provis JL, Reid A, Wang H., 2014. Geopolymer foam concrete: an emerging
17
18 794 material for sustainable construction. *Constr Build Mater* 2014; 56:113–27.
19
20 795 Zhang, M., Guo, H., El-Korchi, T., Zhang, G., Tao, M., 2013. Experimental feasibility
21
22 796 study of geopolymer as the next-generation soil stabilizer. *Constr. Build. Mater.* 47,
23
24 797 1468–1478. <https://doi.org/10.1016/j.conbuildmat.2013.06.017>
25
26
27
28
29
30 798
31
32
33
34
35
36
37
38
39
40
41
42
43
44
45
46
47
48
49
50
51
52
53
54
55
56
57
58
59
60
61
62
63
64
65

Table 1

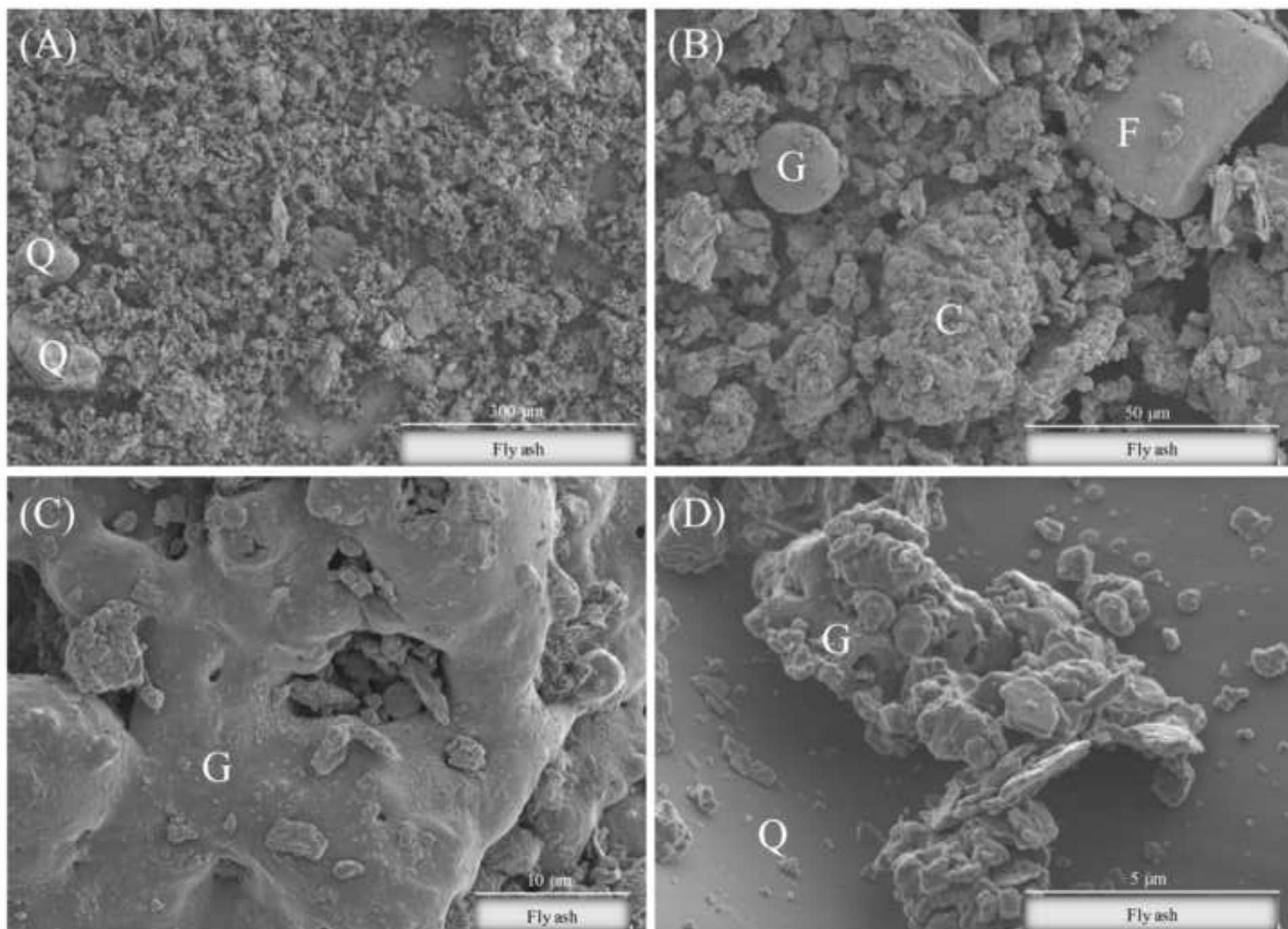
Chemical composition (wt. %) of raw fly ash and kaolin.

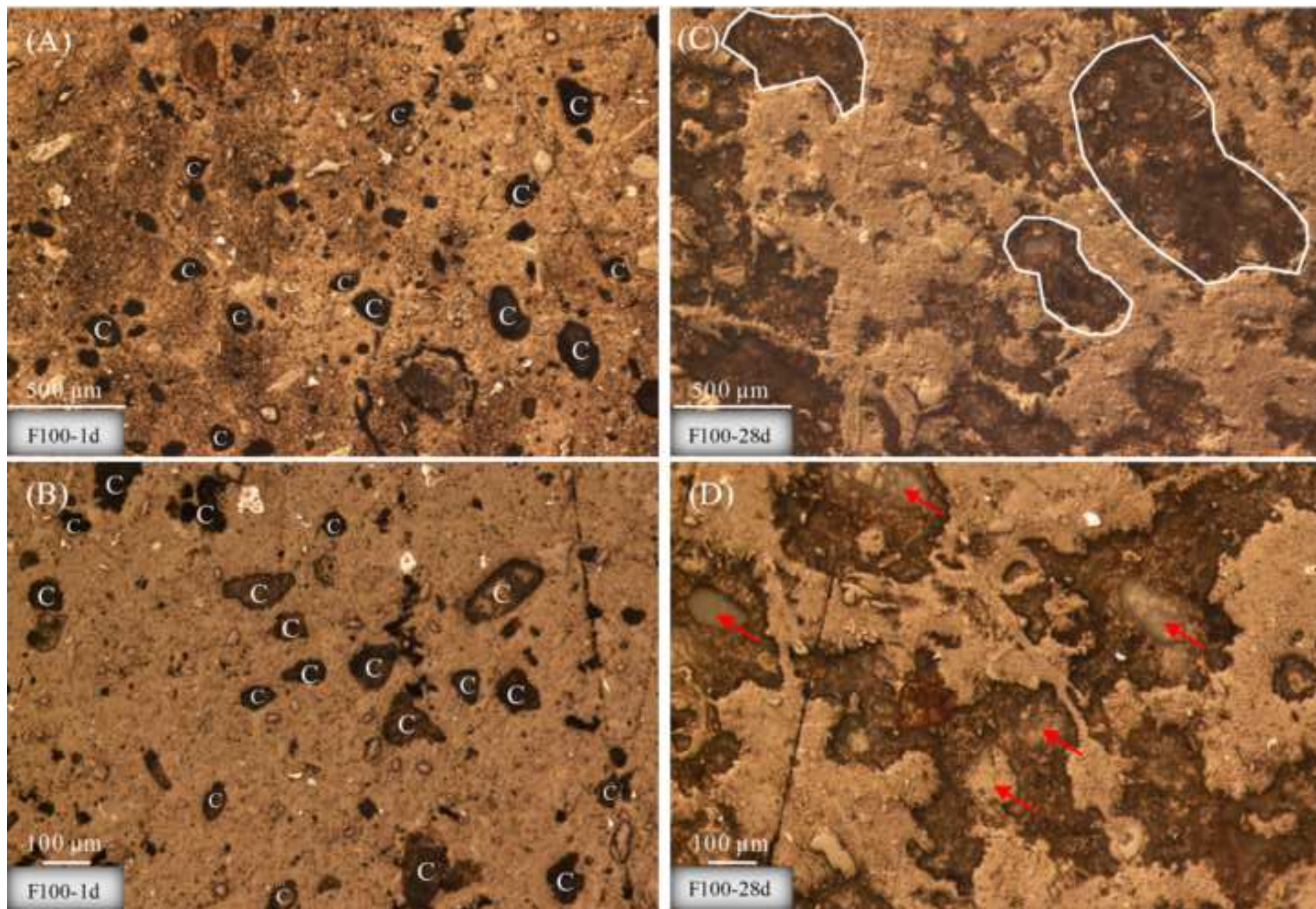
	SiO ₂	Al ₂ O ₃	Fe ₂ O ₃	CaO	CaO _{free} ^a	MgO	SO ₃	Na ₂ O	K ₂ O	H ₂ O	L.o.I.
Fly ash	39.4	19.8	7.4	18.6	5.2	1.8	4.1	2.0	1.8	0.0	1.7 ^b
Kaolin	49.2	34.5	1.2	0.0	0.0	0.2	0.0	0.1	1.7	13.1	12.0 ^c

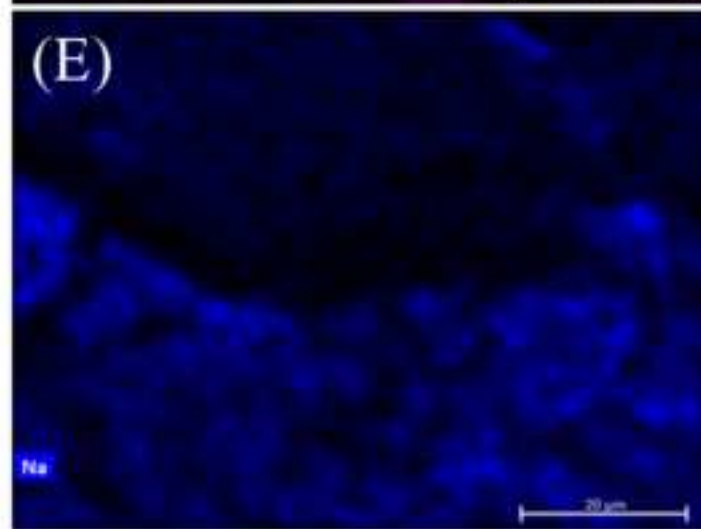
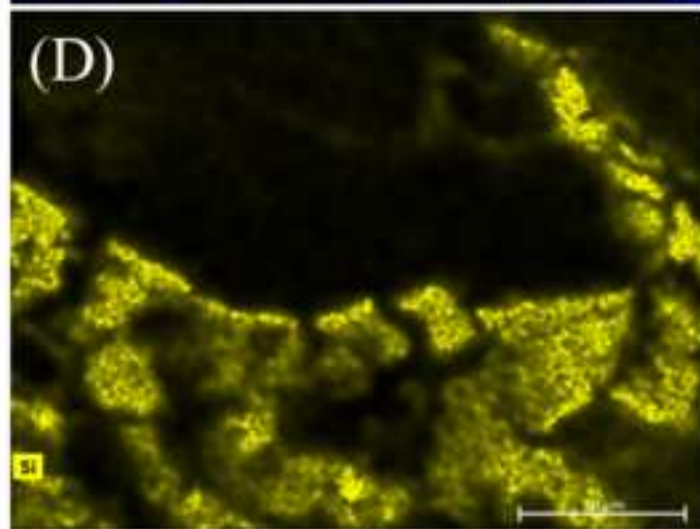
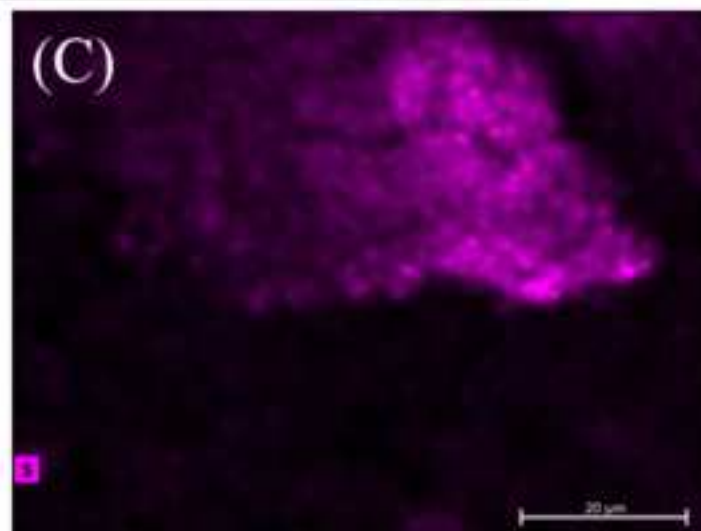
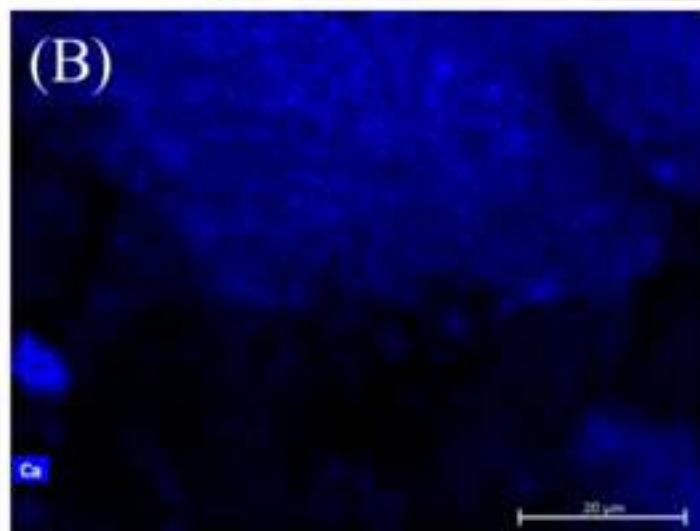
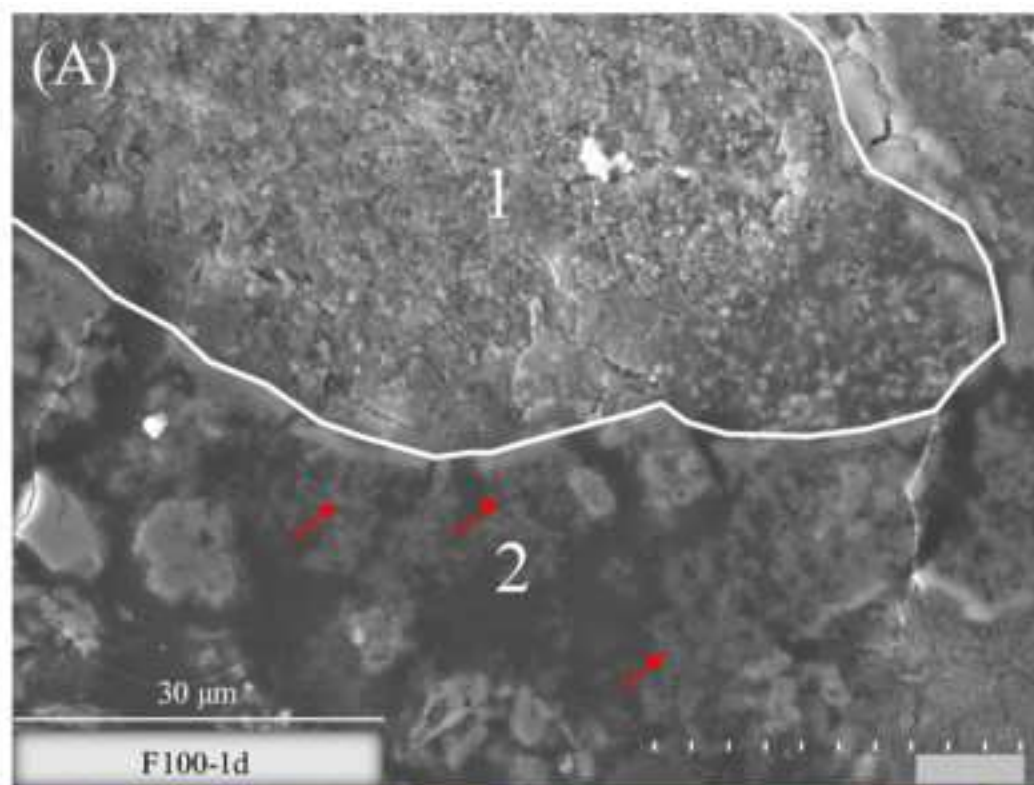
^a Free calcium oxide content

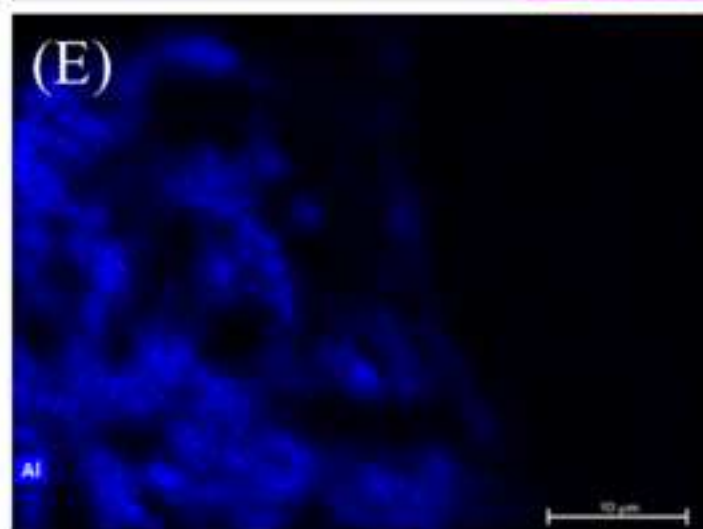
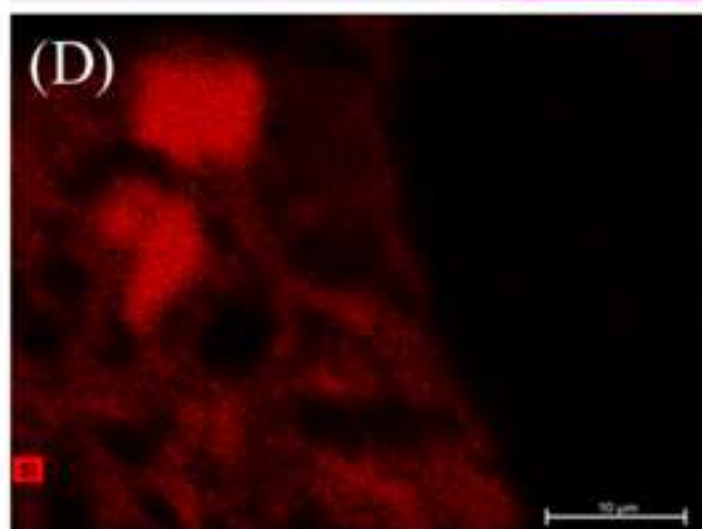
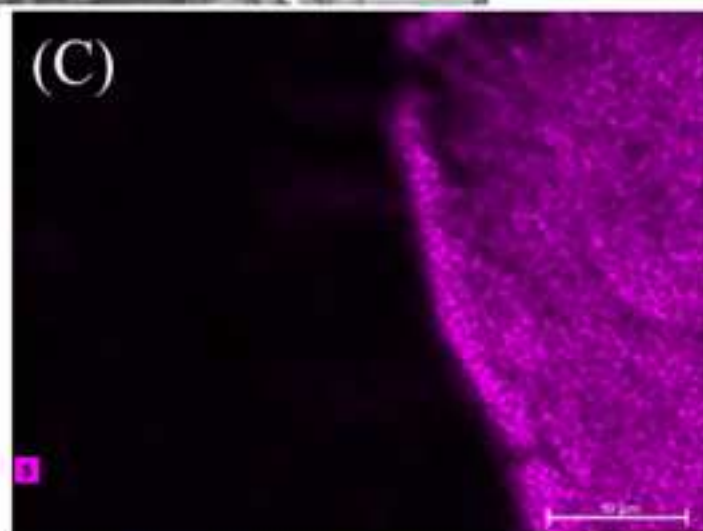
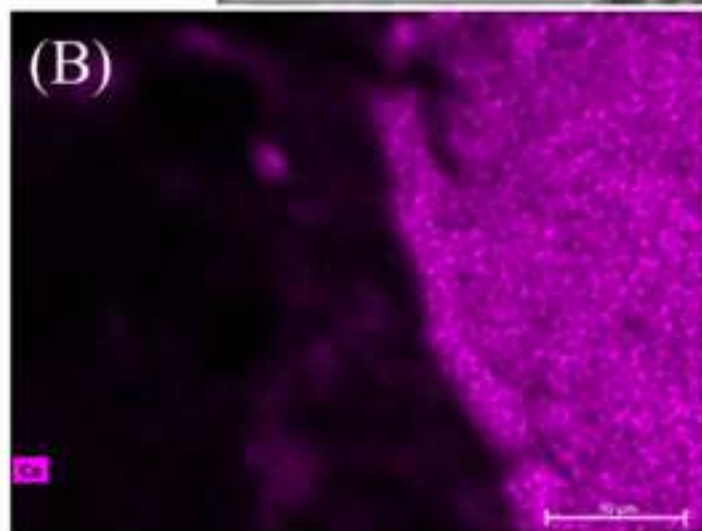
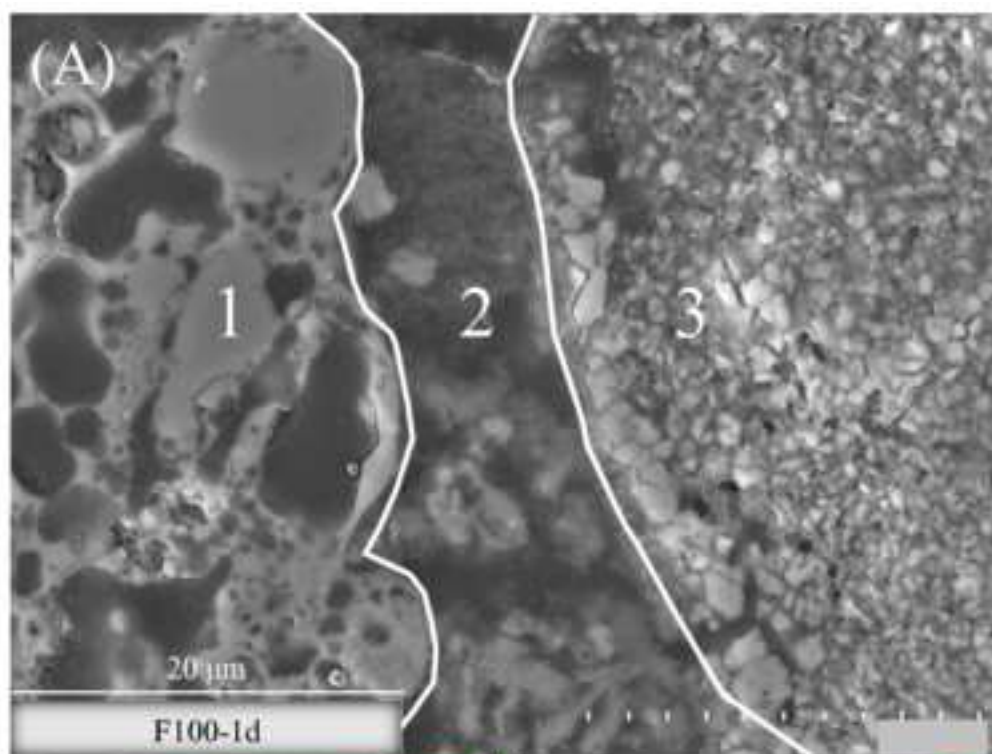
^b L.o.I = Loss on ignition 900 °C

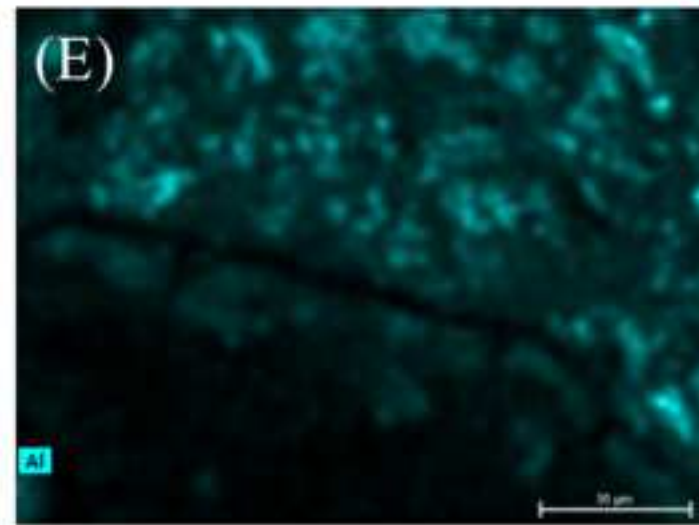
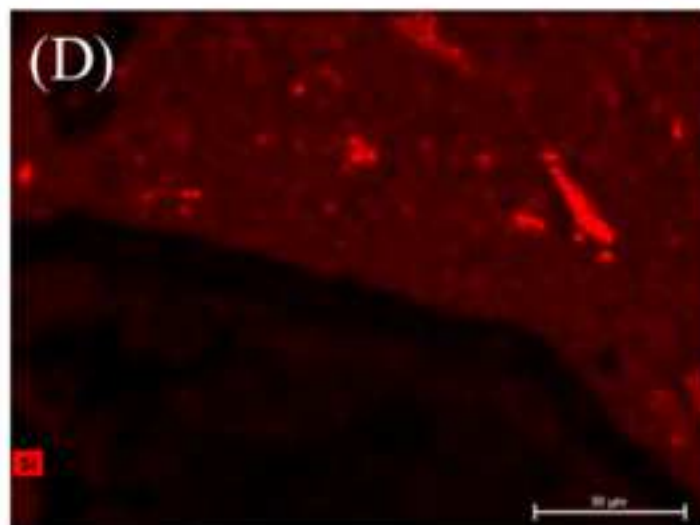
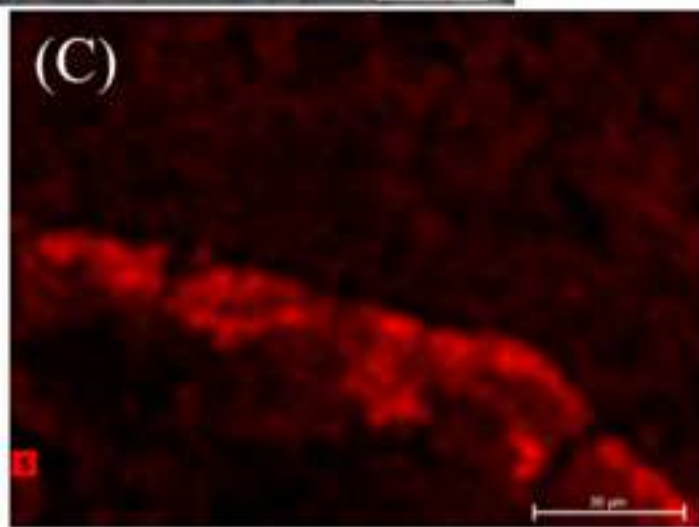
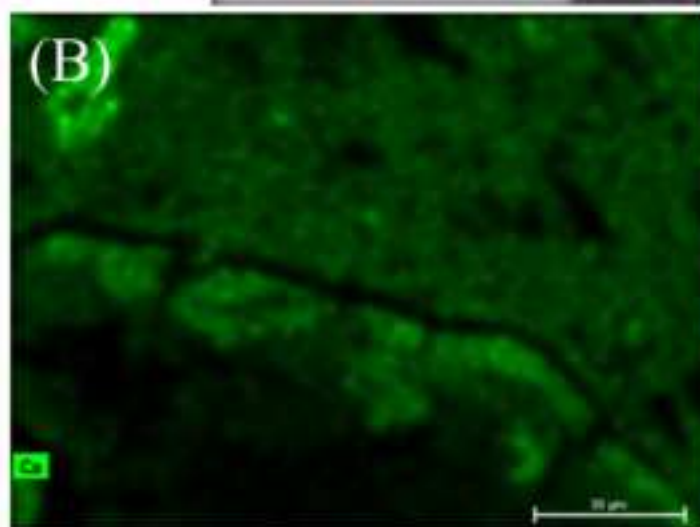
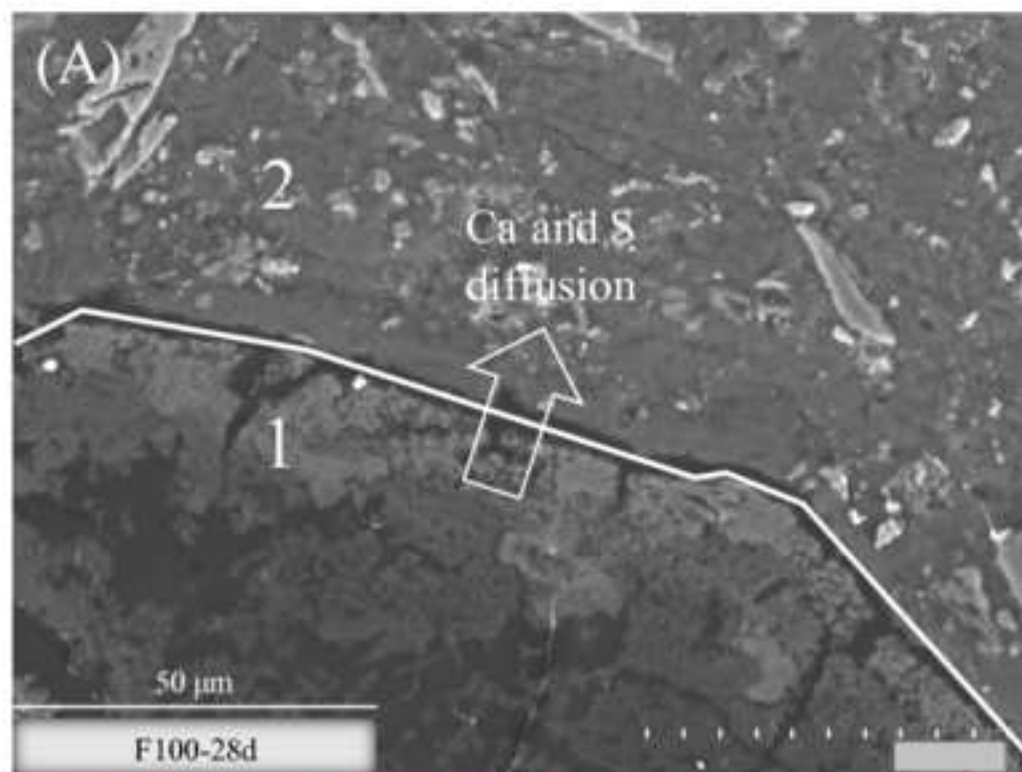
^c L.o.I = Loss on ignition 1000 °C

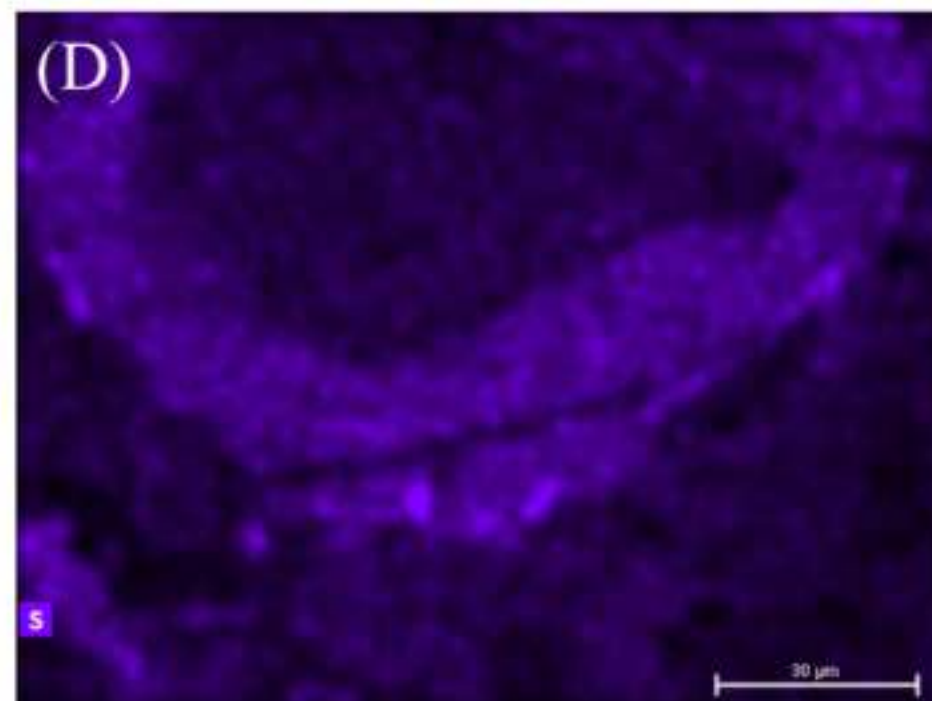
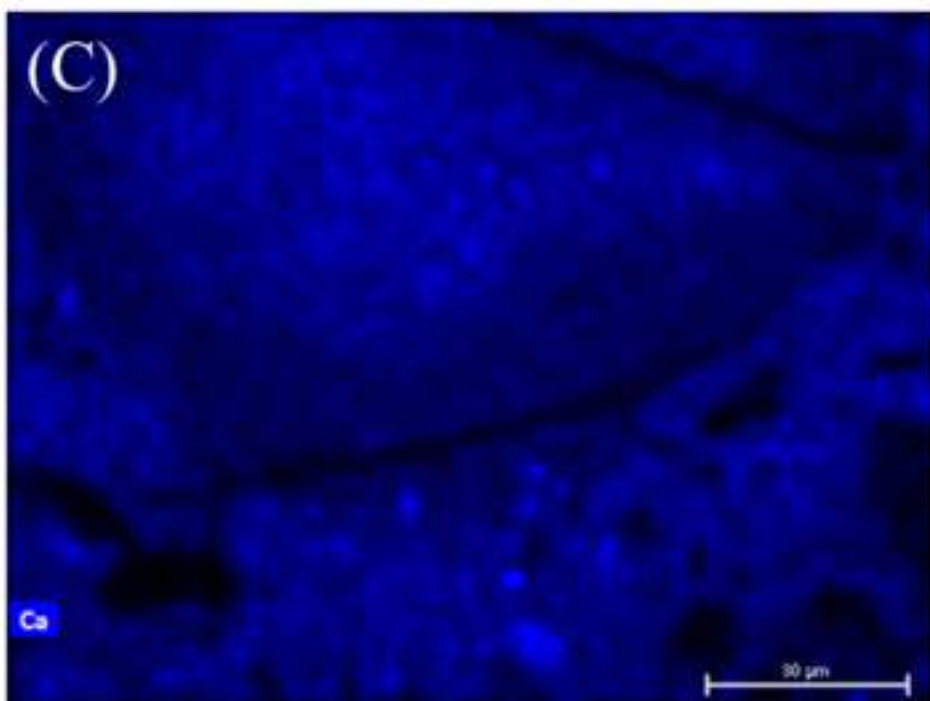
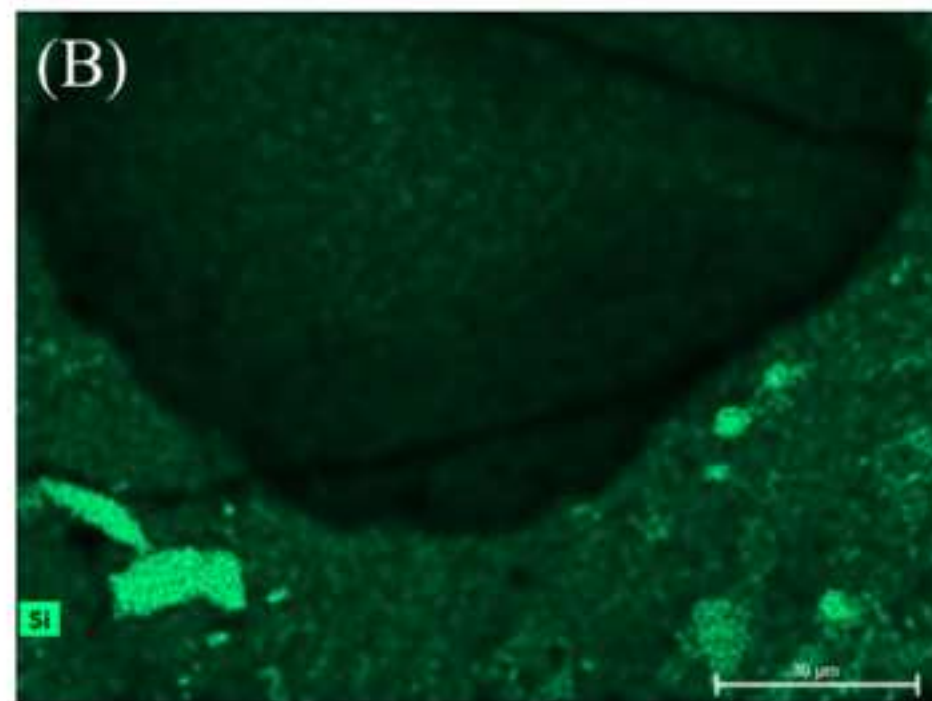
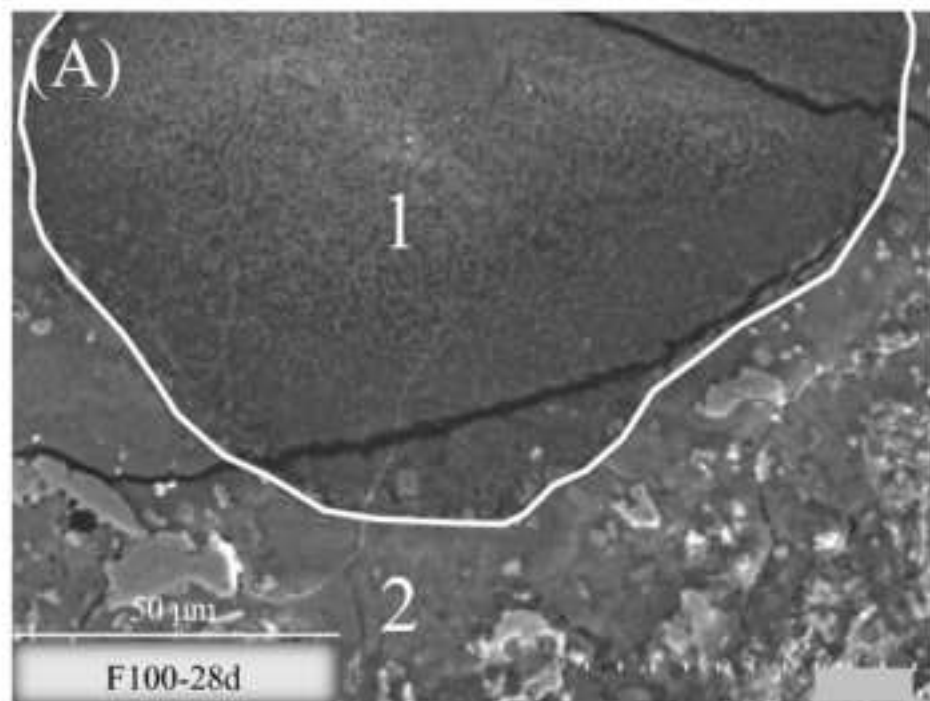


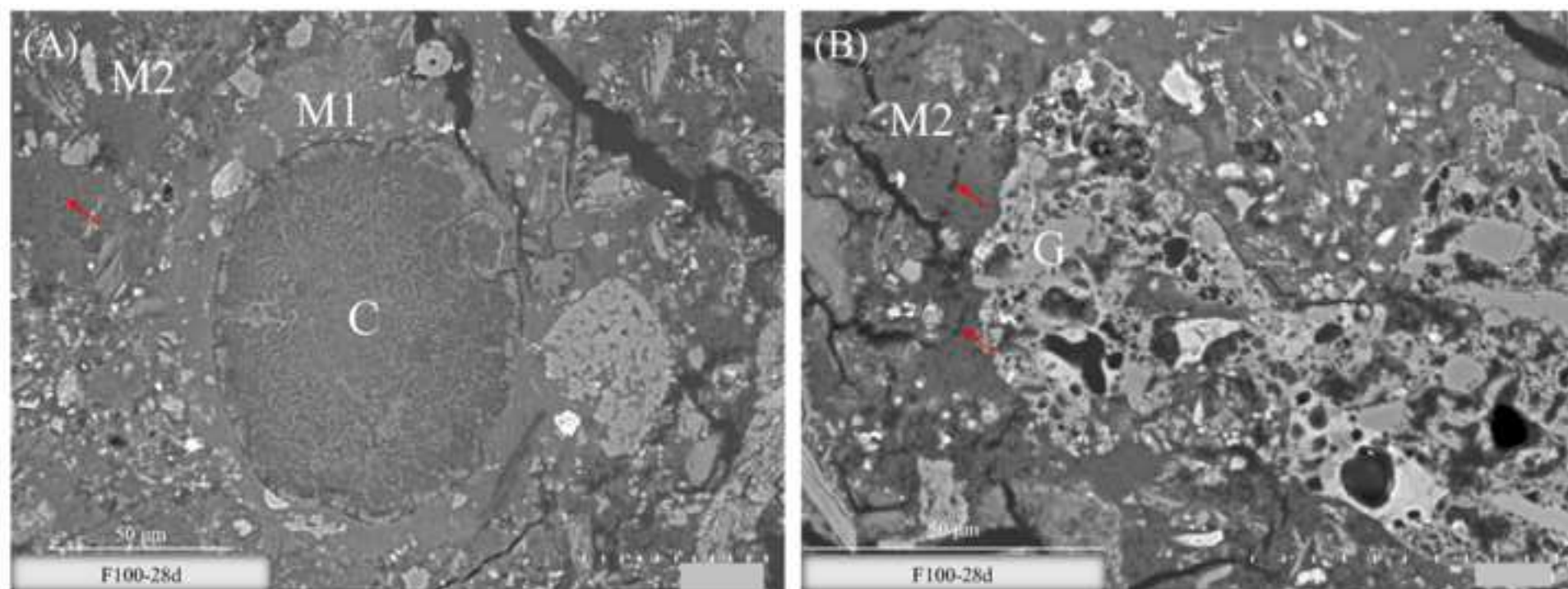


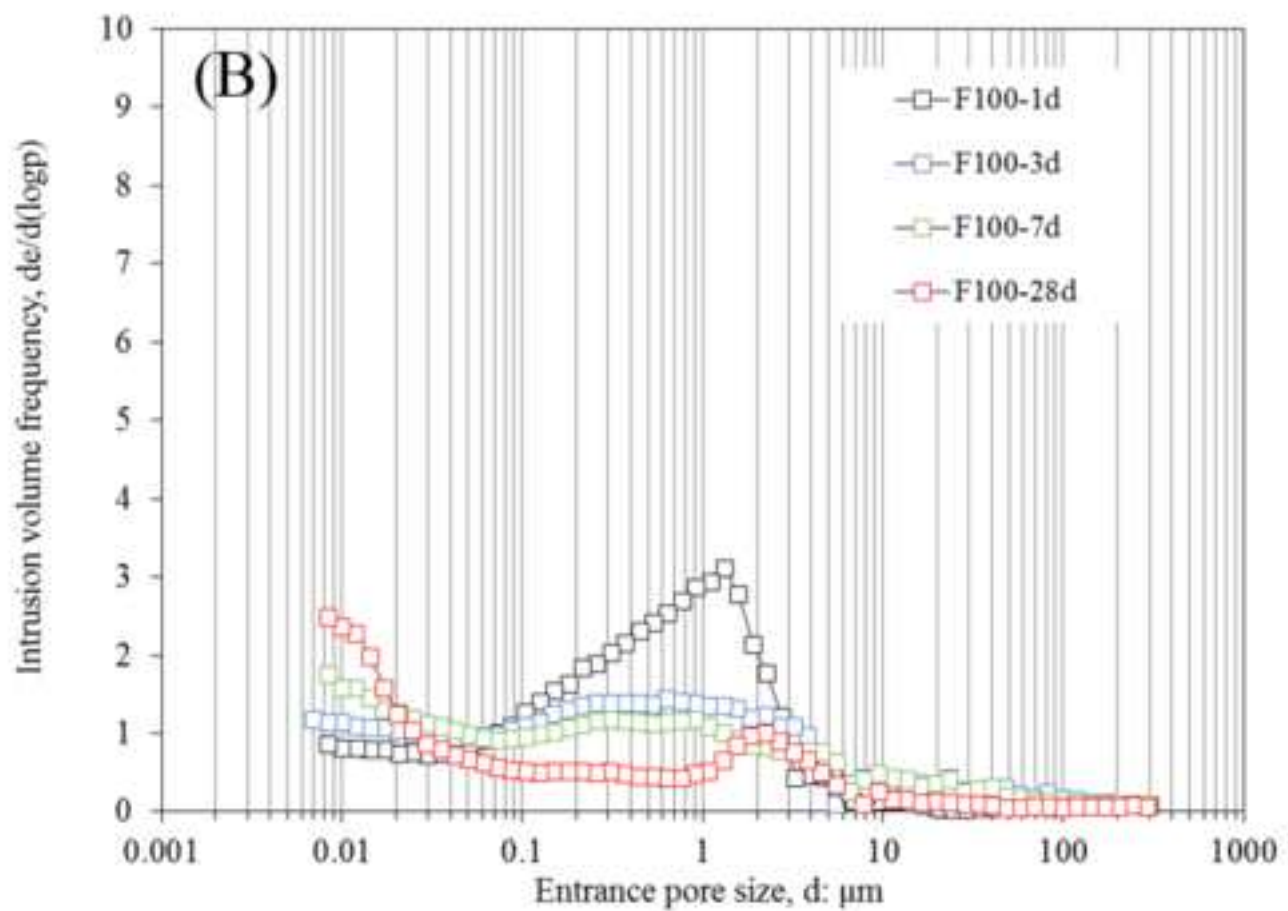
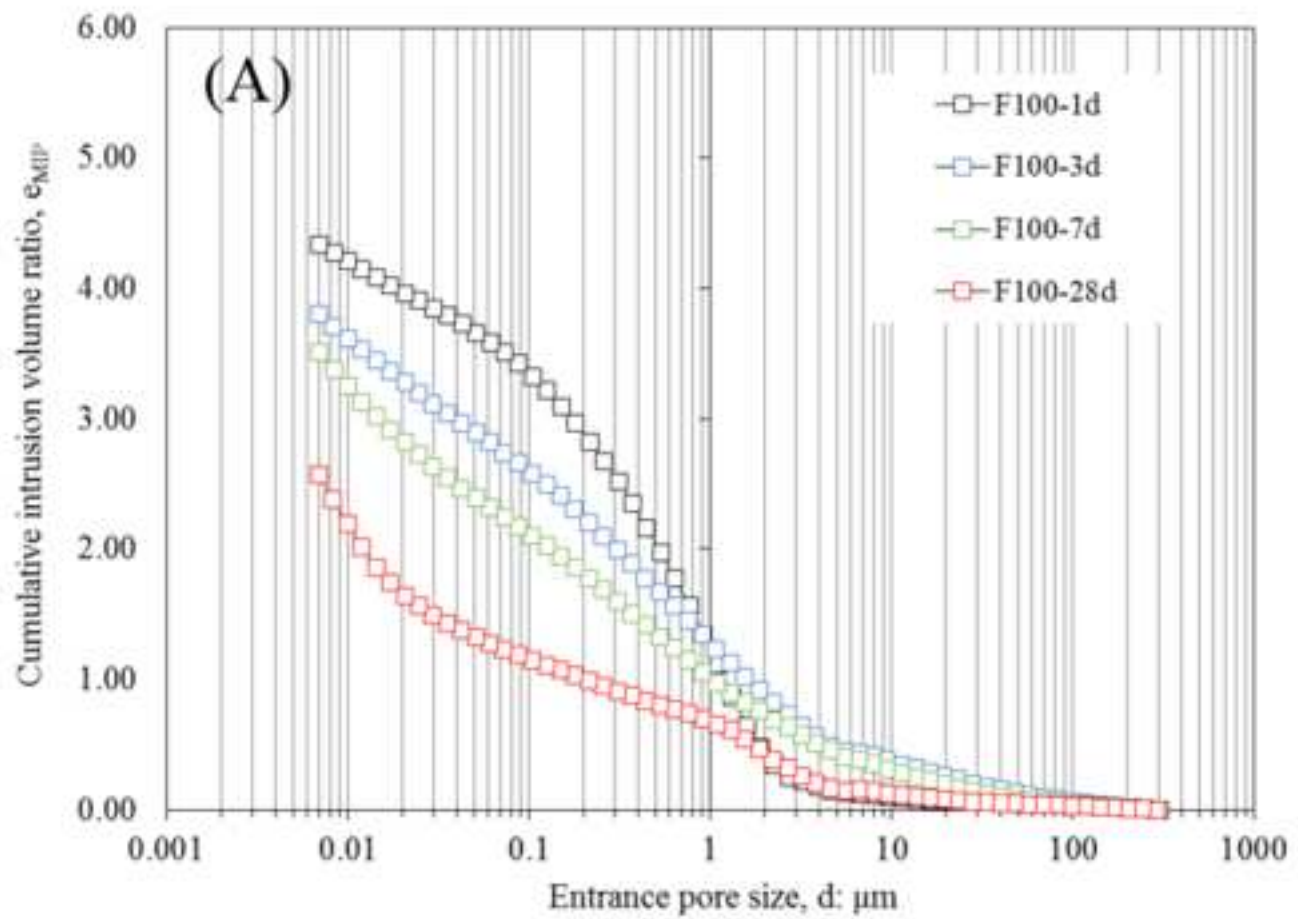


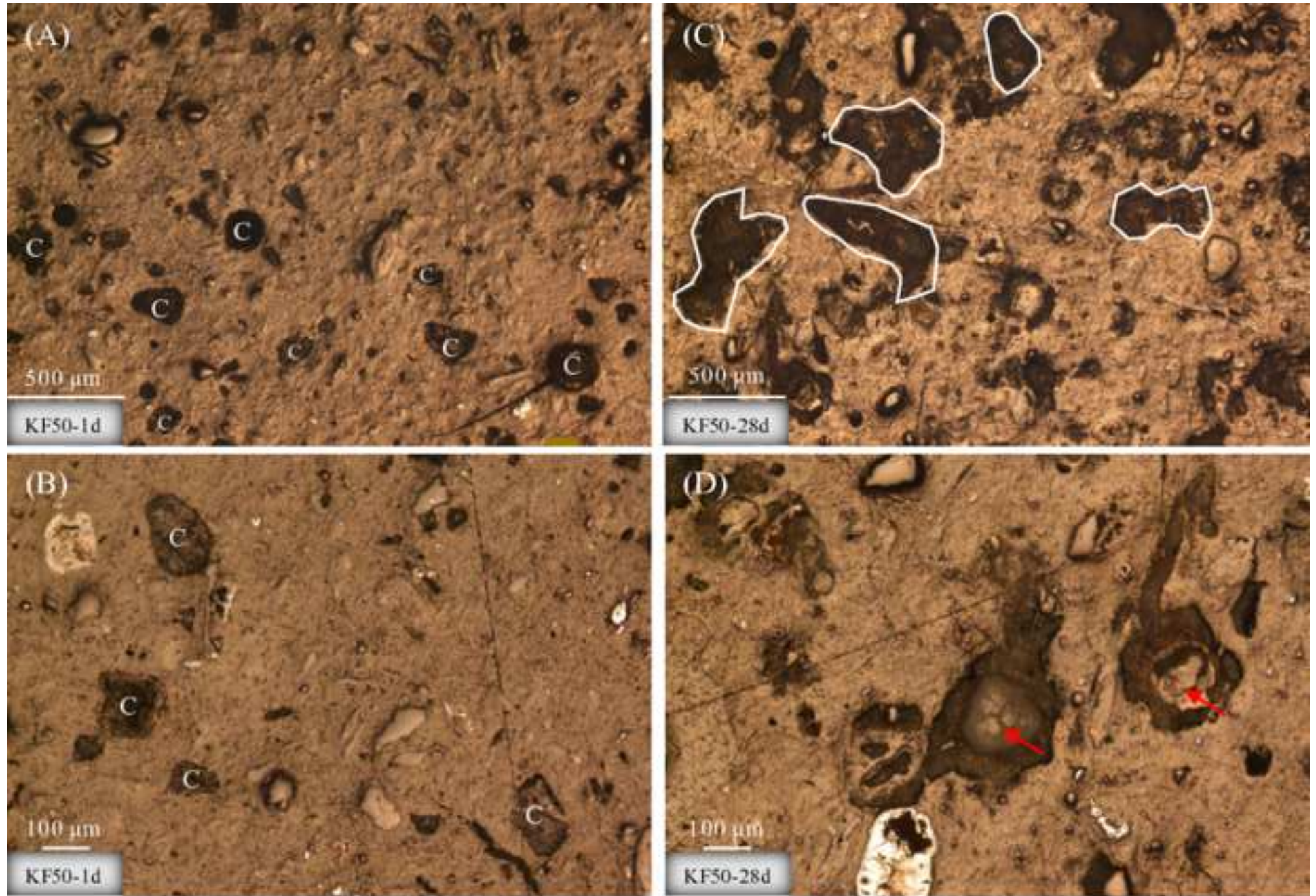


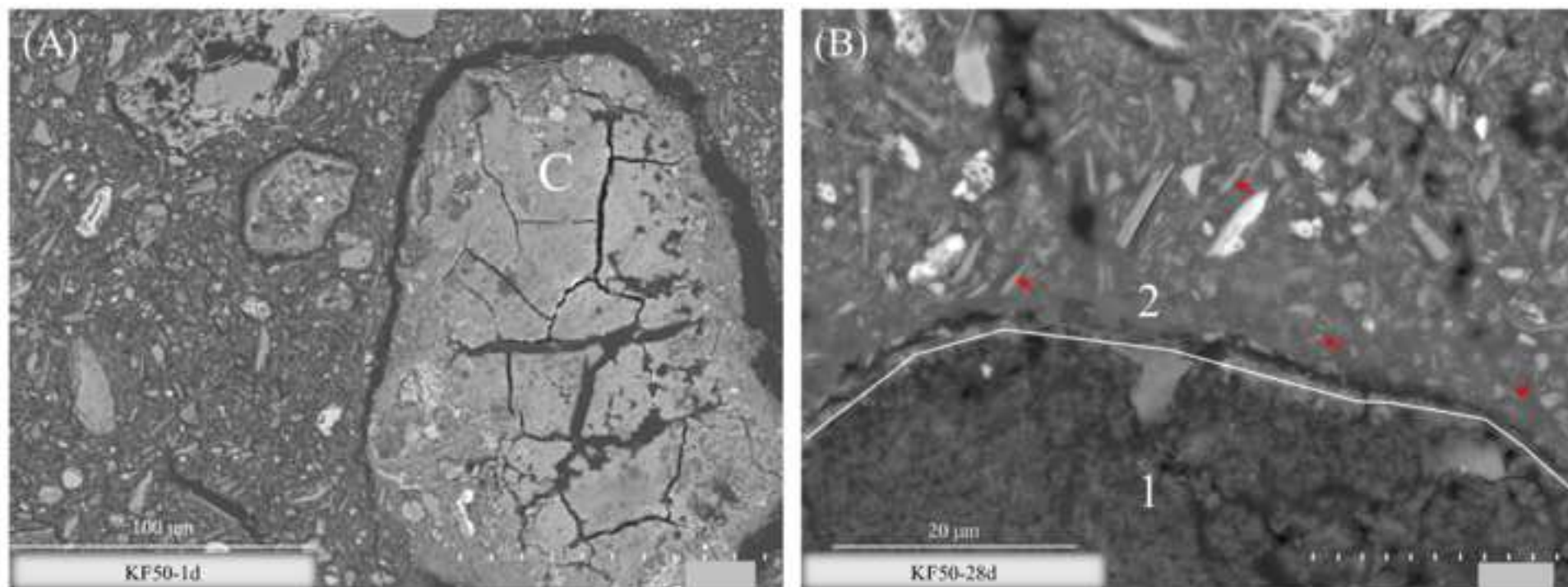


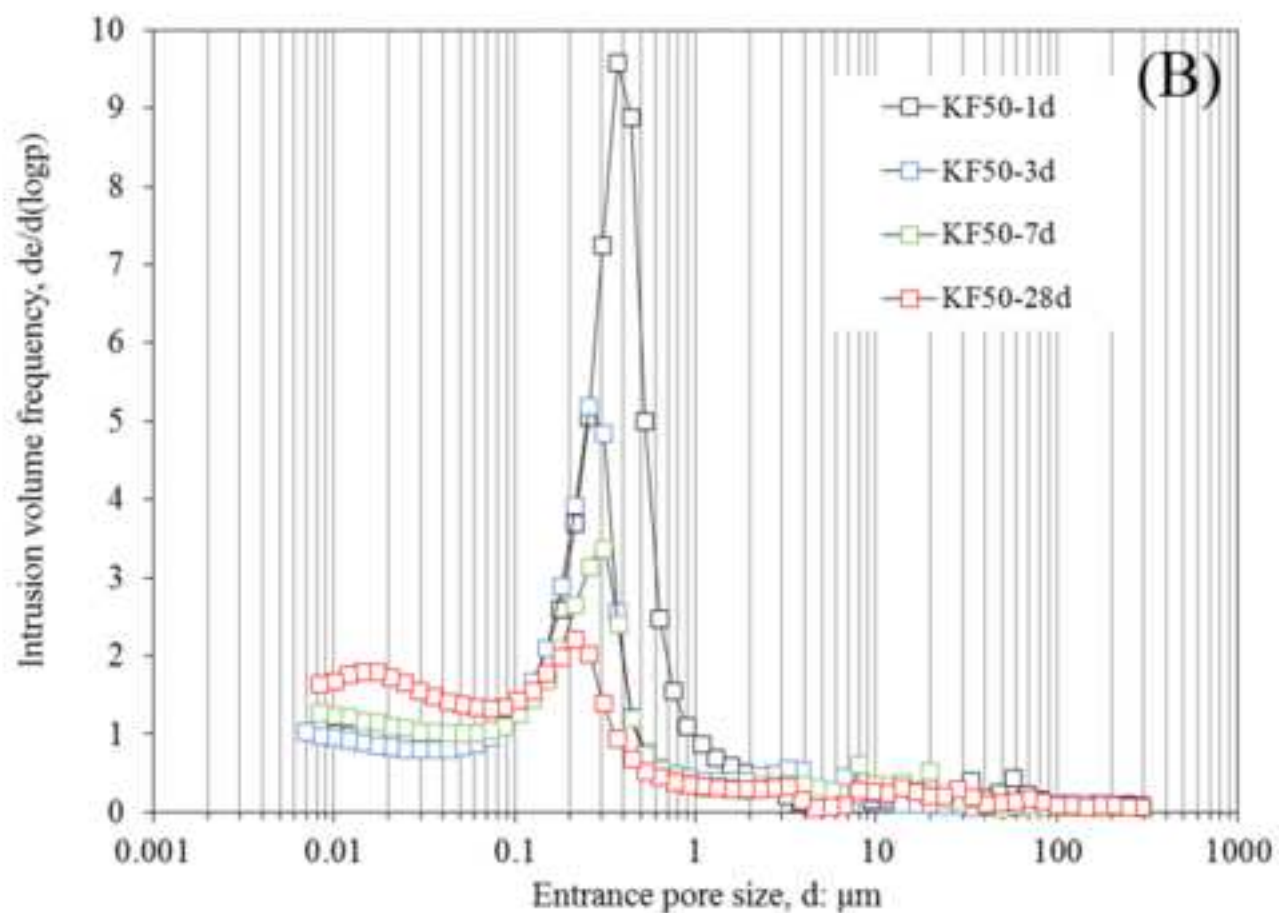
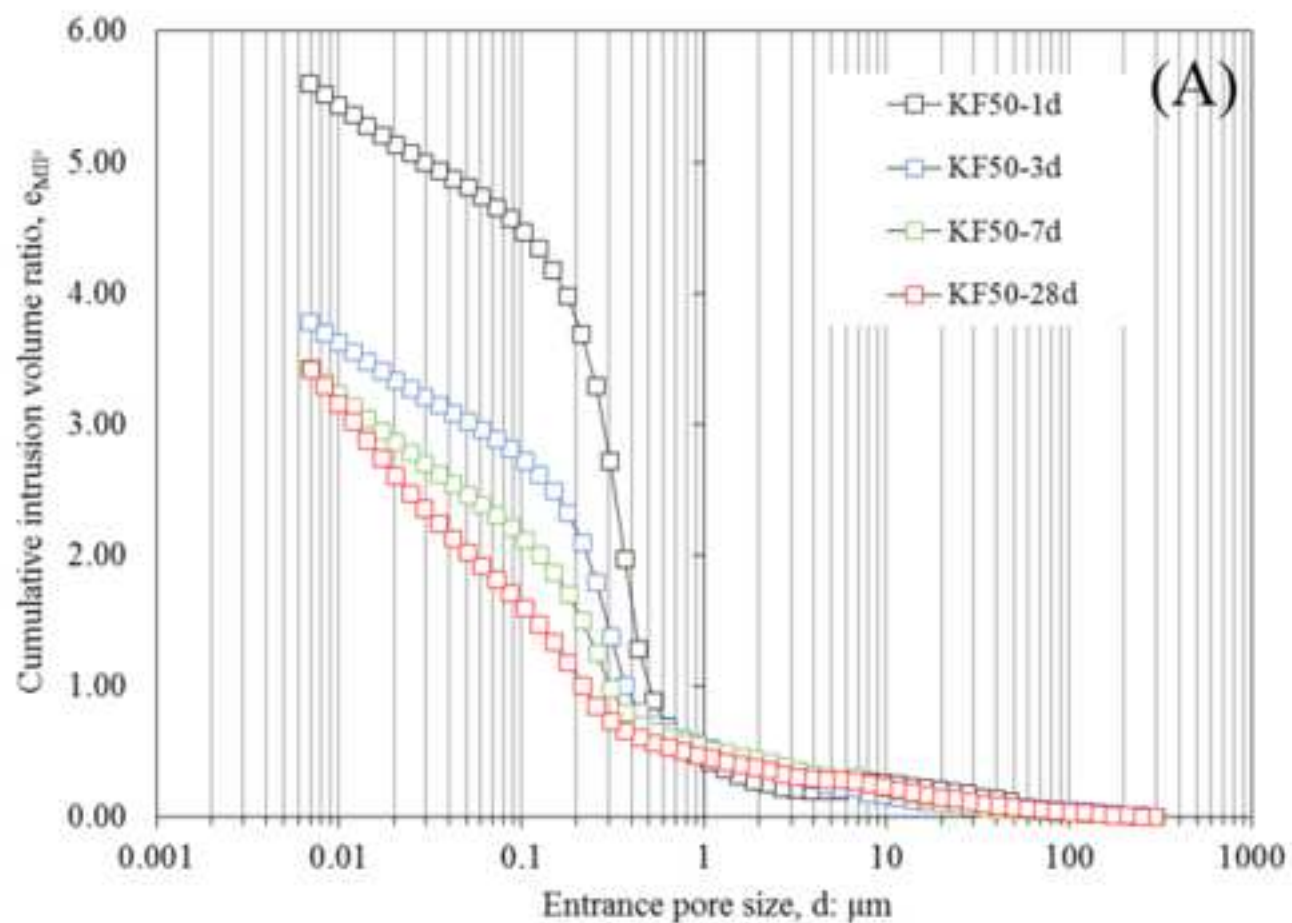


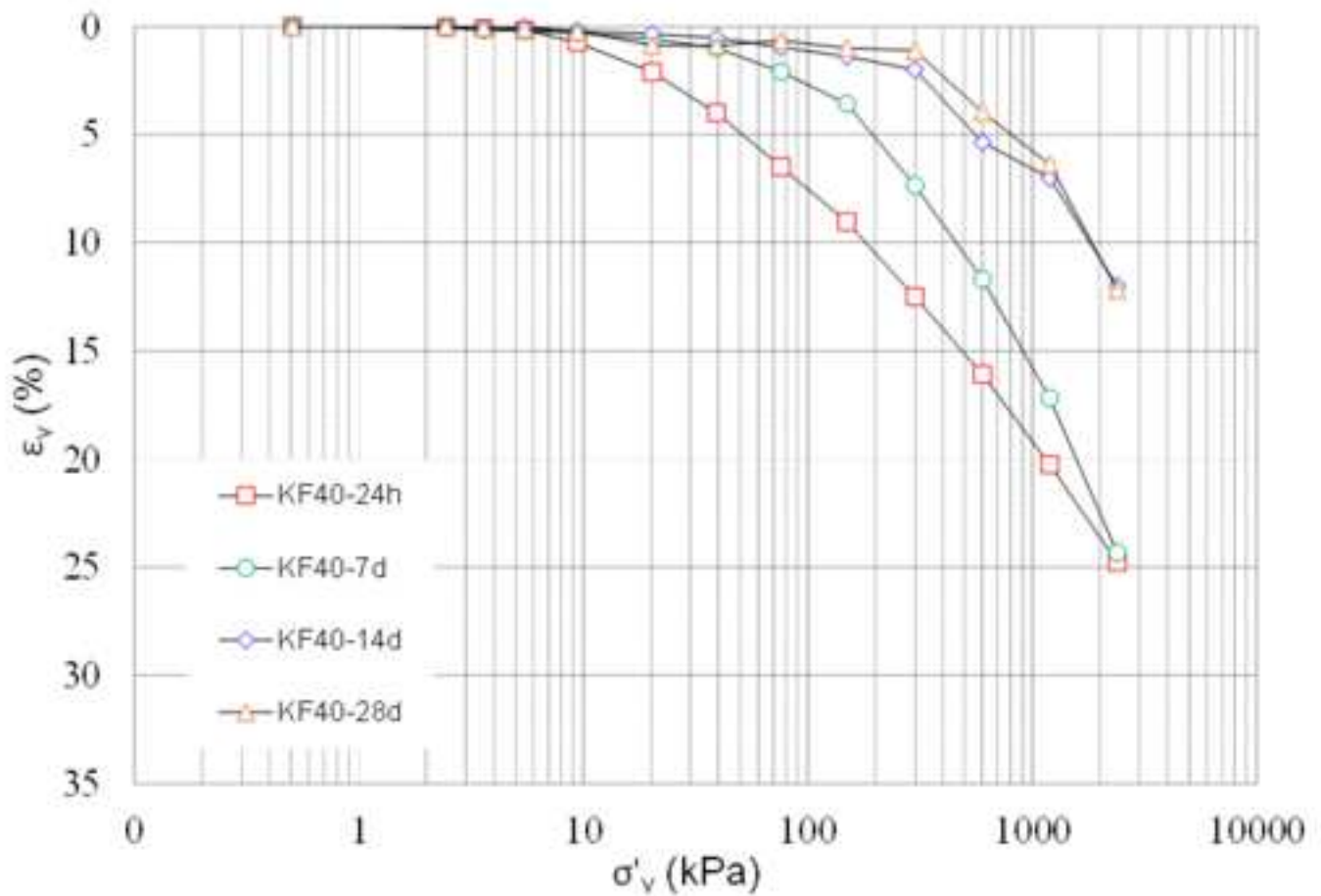
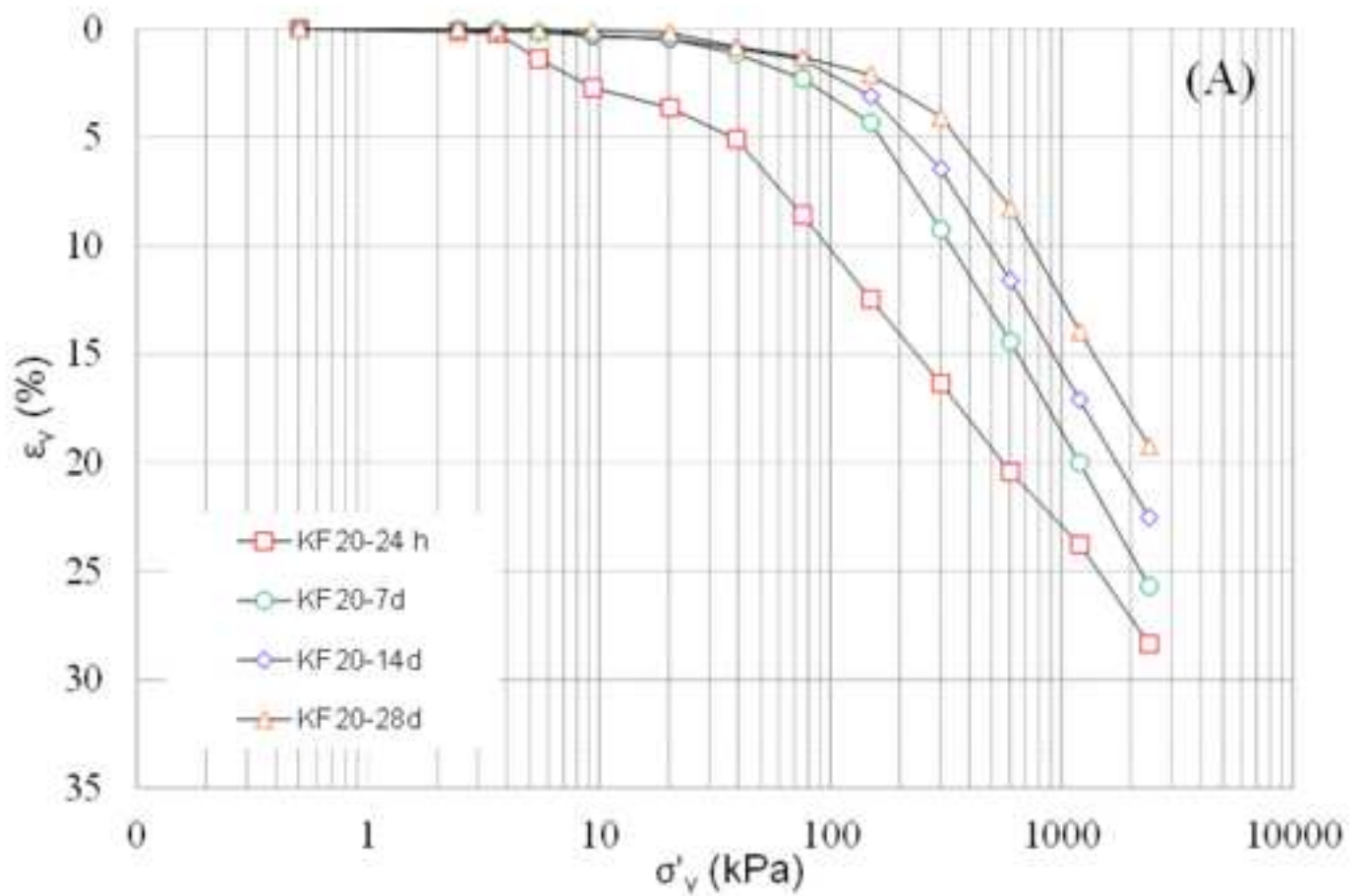


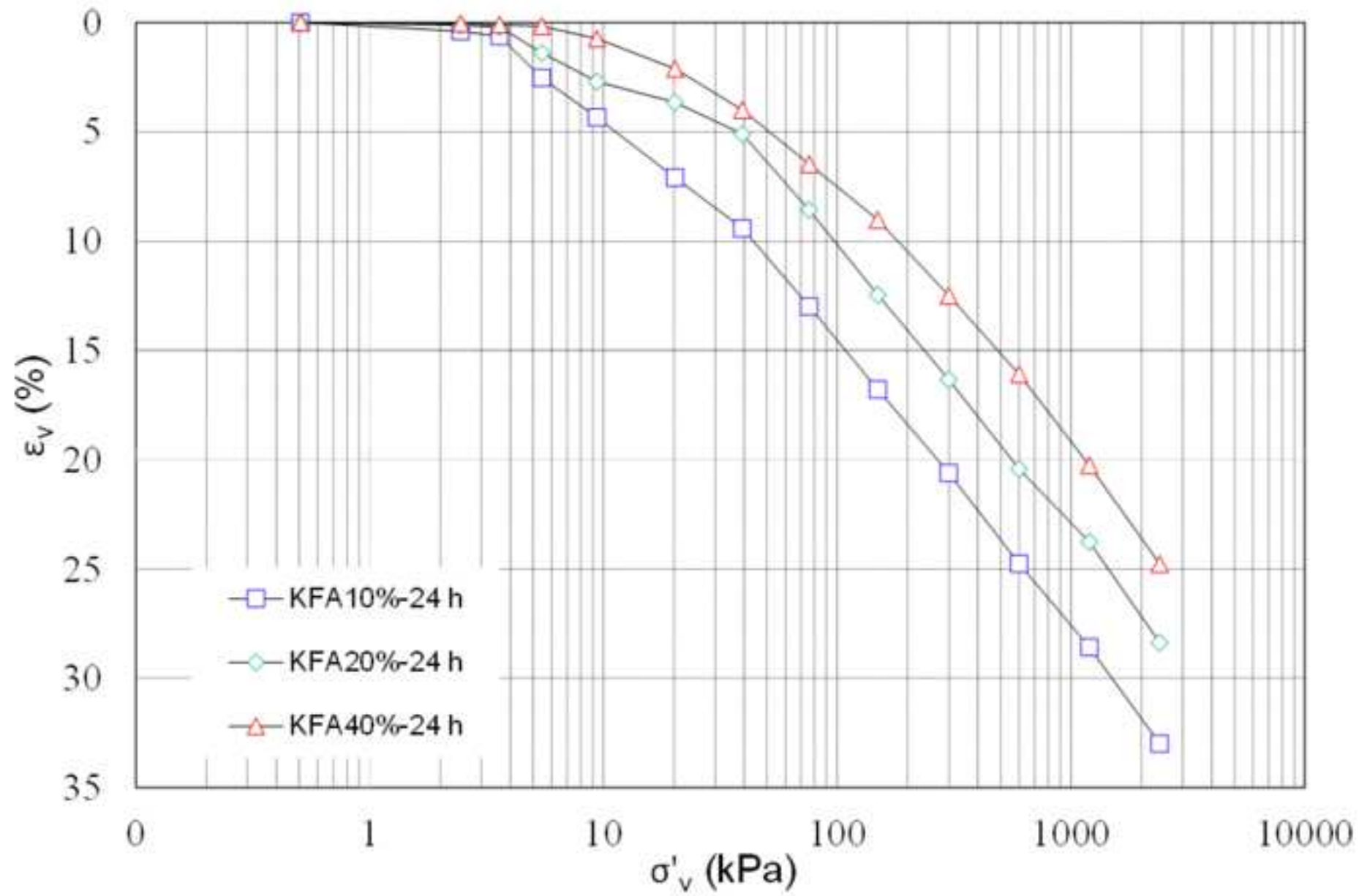


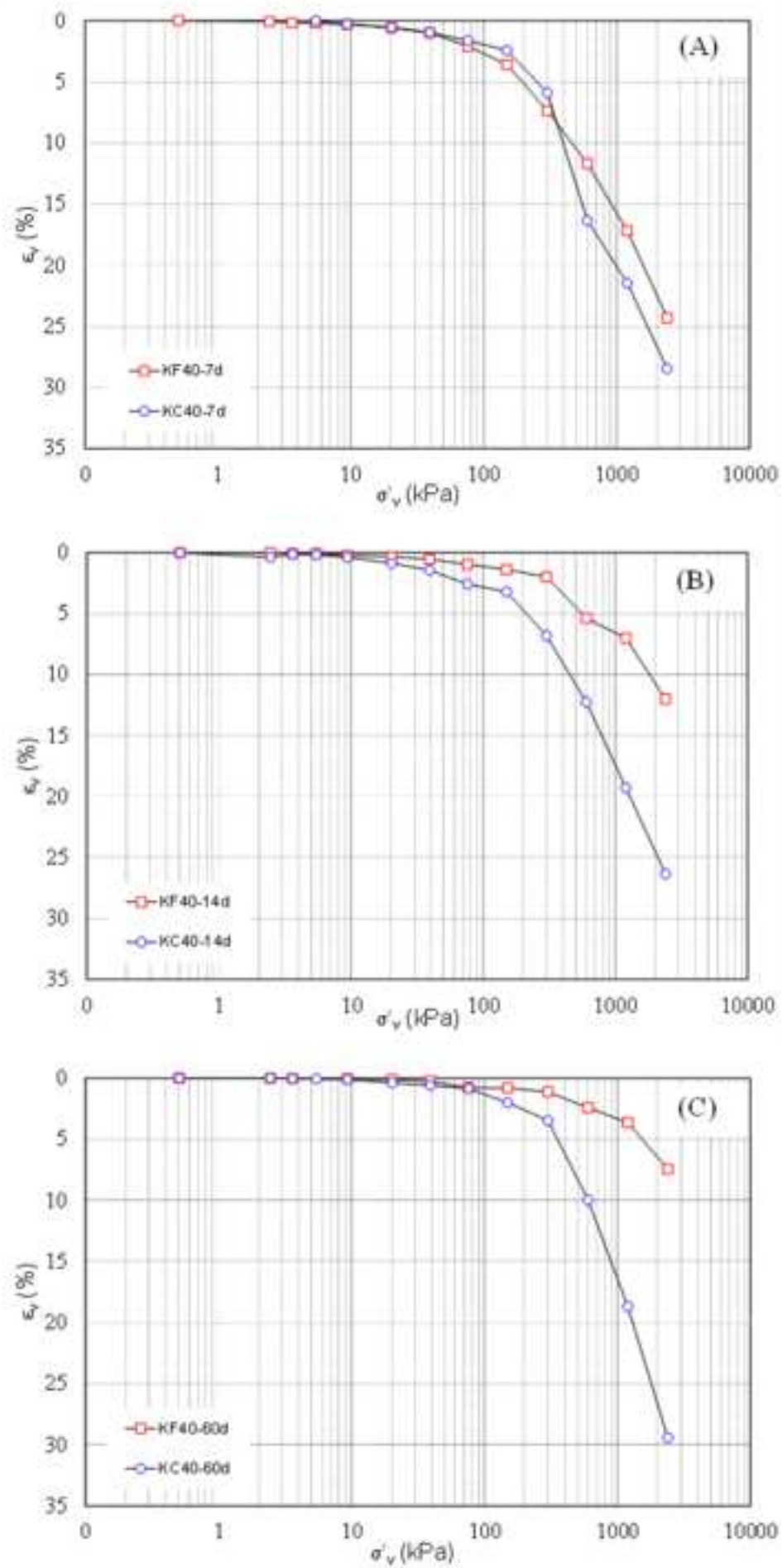












ANSWERS TO EDITOR COMMENTS

We would like to thank the Editor for giving us the opportunity of revising the paper

EDITOR

Note that "mechanical behavior of the alkali activated binder treated soils" needs to be included in this study. We do not want salami sliced papers! Your "Use of alkali activated High-calcium fly ash binder for kaolin clay soil stabilisation: Physicochemical evolution" has already been accepted. I would suggest that you combine the remaining two of three structural levels (namely, microstructure level, and volume element level), into this paper

Authors' Reply

It was not our intention to produce salami papers, the mechanical part was not included simply because we had no mechanical tests at the time of submission on the 'reconstituted' material, which is the object in this paper and the previous one already published. However, we agree with the editor that adding a mechanical part makes the paper more robust. We have therefore conducted additional mechanical tests (one-dimensional compression) and the revised version of the paper now combines the microstructure level with experimental evidence at volume element level.

As a result:

- 1) the title of the paper has been amended as follows:
"MICROSTRUCTURAL EVOLUTION AND MECHANICAL BEHAVIOUR OF ALKALI ACTIVATED FLY ASH BINDER TREATED CLAY"
- 2) one Author has been added, namely Dr Enza Vitale (University of Naples Federico II), who conducted the additional mechanical tests reported in the paper.
- 3) Text with marked changes has been uploaded for highlights the added parts.

Highlights

- alkali activated fly ash-based binder enhances engineering characteristics of soft clay-rich soils
- microstructural evolution of a calcium-rich fly ash from coal combustion-based binder activated by a sodium-based alkaline solution has been investigated
- microstructural changes occur around calcium-containing phases derived from fly ash which are the reactive phases of the system
- evolution of the pore network over time is characterized by a progressive filling of capillary pores by new compounds
- relevant improvement of mechanical performances of soil treated by alkali activated fly ash-based binder have been detected

Declaration of interests

The authors declare that they have no known competing financial interests or personal relationships that could have appeared to influence the work reported in this paper.

The authors declare the following financial interests/personal relationships which may be considered as potential competing interests:

Elodie Coudert: Data curation; Investigation; Methodology; Roles/Writing - original draft; Writing - review & editing. **Dimitri Deneele:** Conceptualization; Data curation; Investigation; Methodology; Supervision. **Giacomo Russo:** Conceptualization; Data curation; Methodology; Supervision; Roles/Writing - original draft; Writing - review & editing. **Alessandro Tarantino:** Conceptualization; Methodology; Supervision.

**MICROSTRUCTURAL EVOLUTION AND MECHANICAL BEHAVIOUR OF ALKALI
ACTIVATED FLY ASH BINDER TREATED CLAY**

1 **MICROSTRUCTURAL EVOLUTION AND MECHANICAL BEHAVIOUR OF**
2
3 **ALKALI ACTIVATED FLY ASH BINDER TREATED CLAY**
4
5
6

7
8 Elodie Coudert^{a,b}, Dimitri Deneele^{c,d}, Giacomo Russo^{e*}, Enza Vitale^e, Alessandro
9
10 Tarantino^b
11
12

13
14
15
16 ^a Department of Civil and Mechanical Engineering, University of Cassino and Southern
17 Lazio, Via Gaetano di Biasio, 43, 03043 Cassino, FR, Italy

18
19 ^b Department of Civil and Environmental Engineering, University of Strathclyde, 75
20 Montrose Street, Glasgow, Scotland, G1 1XJ, United Kingdom

21
22
23 ^c Institut des Matériaux Jean Rouxel (IMN), Université de Nantes, CNRS, 2 rue de la
24 Houssinière, BP 32229, 44322 Nantes Cedex 3, France

25
26 ^d GERS-LEE, Univ Gustave Eiffel, IFSTTAR, F-44344 Bouguenais, France

27
28 ^e Department of Earth Science, Environment and Resources, University of Napoli
29 Federico II, Via Cinthia 21 80126, Napoli, Italy

30
31
32 * Corresponding Author, giaruso@unina.it
33
34
35
36
37
38
39
40
41
42
43
44
45
46
47
48
49
50
51
52
53
54
55
56
57
58
59
60
61
62
63
64
65

1 **18 Abstract**

2
3
4 19 This work focuses on the use of alkali activated fly ash-based binder to enhance
5
6 20 engineering characteristics of soft clay-rich soils and as a substitute to standard stabilisers
7
8 21 (e.g., ~~that are~~ lime or cement). Especially, it examines the microstructural evolution of a
9
10 22 calcium-rich fly ash from coal combustion-based binder activated by a sodium-based
11
12 23 alkaline solution. To this end, the processes generating the microstructure and the
13
14 24 evolution of the pore network over time are investigated. A second point addressed by
15
16 25 this study is how the presence of ~~small-sized~~ kaolin particles soil affects the
17
18 26 microstructural features of the binder. The microstructure has therefore been investigated
19
20 27 by considering the binder alone and the binder mixed with kaolin. The effects of
21
22 28 microstructural evolution have been observed at macroscopic level by means of one-
23
24 29 dimensional compression tests.

25
26 30 The combination of completing techniques has been used including Optical microscopy,
27
28 31 Scanning Electron Microscopy and Mercury Intrusion Porosimetry in order to gain an
29
30 32 overview of the complex pore structure.

31
32 33 Microstructural changes occur around calcium-containing phases derived from fly ash
33
34 34 which are the reactive phases of the system. Namely, the dissolution of calcium-rich
35
36 35 grains leads to the formation of new compounds that first cover the grain surfaces and
37
38 36 then further grow into the available space. Furthermore, the evolution of the pore network
39
40 37 over time is characterized by a progressive filling of capillary pores by new compounds
41
42 38 while small nanometric pores are being formed and associated with the newly formed
43
44 39 silicate-calcium chains. Similar tendencies are observed when the binder is mixed with
45
46 40 the soil although the general porosity is lesser due to the filling of pores by small-sized
47
48 41 kaolinite platelets. Experimental evidences at microscale level have been linked to the
49
50 42 macroscopic behaviour of treated soil.

49
50 44 **Keywords:** Kaolin, Fly ash, Soil treatment, Alkali activated material, Microstructure,
51
52 45 Mechanical Behaviour

53
54
55
56 47 **1. Introduction**

1 48 Soft clay-rich soils are frequently encountered in construction sites. Their poor
2
3 49 mechanical performances represent a critical issue in engineering projects and are
4
5
6 50 commonly improved by using either Ordinary Portland Cement or lime as a soil stabiliser.
7
8 51 Nevertheless, those conventional stabilisers are associated with high carbon dioxide
9
10 52 emissions and energy intensive processes, significantly increasing the worldwide carbon
11
12
13 53 footprint (Scrivener and Kirkpatrick, 2008, Xi et al. 2016). The anthropogenic carbon
14
15
16 54 emissions have been increasingly recognized to be one of the main responsible of climate
17
18 55 changes and environmental degradation (United Nations, 2004). In the low carbon
19
20
21 56 agenda, it is then of outmost relevance the development of cost- and carbon-efficient
22
23 57 technologies. In the construction sector, for which cement production contributes to at
24
25 58 least 5–8% of global carbon dioxide emissions (Scrivener and Kirkpatrick, 2008),
26
27
28 59 alternative industrial by-products (e.g. high-calcium fly ash, rice husk ash, silica fume)
29
30 60 have been successfully used as cementing agents in soil improvement resulting in
31
32
33 61 environmental and economic benefits (Basha et al. 2003, Nalbantoğlu 2004, Sargent
34
35 62 2015, James & Pandian 2016).

36
37 63 As an alternative, the use of Alkali Activated Material (AAM) as a soil stabiliser is
38
39
40 64 gaining more and more attention over the past ten years. Alkali Activated Materials are
41
42 65 defined as any binder system derived by the reaction of an alkali metal source (usually
43
44
45 66 alkali hydroxide and alkali silicate solutions) with a solid aluminosilicate powder
46
47
48 67 (commonly metakaolin, fly ash, blast furnace slag or natural pozzolan) (Buchwald et al.,
49
50 68 2003; Shi et al., 2006). It gives a hardened material at room temperature with mechanical
51
52 69 properties potentially suitable for Portland cement replacement. Alkali Activated
53
54
55 70 Materials could constitute a viable sustainable soil binder because of their lower CO₂
56
57 71 emission process compared to traditional Portland cement (Duxson et al. 2007; McLellan

1 72 et al. 2011, Zhang et al. 2014). Furthermore, recent studies have shown a positive
2
3 73 potential and feasibility results of using alkali activated binders for soil improvement, and
4
5 74 this not only for different types of soil i.e. clayey soil (Wilkinson et al., 2010; Singhi et
6
7
8 75 al., 2016; Vitale et al. 2017, Vitale et al. 2019; Vitale et al. 2020a, 2020b), sandy clay
9
10 76 (Cristelo et al., 2011), marl, marlstone (Cristelo et al., 2012), silty sand (Rios et al., 2016)
11
12
13 77 or else road aggregates (Tenn et al., 2015); but also for different applications i.e. in deep
14
15 78 soft soil (Cristelo et al., 2011), at shallow depth (Zhang et al., 2013) or in rammed earth
16
17
18 79 construction (Silva et al., 2013).

20 80 Works on alkali activated binder treated soils are relatively recent and constitute a novel
21
22 81 domain of application. Our study particularly focuses on the use of a calcium-rich fly ash
23
24
25 82 from coal combustion activated by sodium-based alkaline solution as a binder for clay
26
27
28 83 kaolin stabilisation. Kaolin was selected as a model soil that represent a wide class of
29
30 84 clays encountered in engineering projects and for maintaining the system simple.
31
32 85 Kaolinite being not reactive to alkaline activation at ambient temperature, a more reactive
33
34
35 86 aluminosilicate source is required for chemical reactions to occur. For that purpose, a
36
37
38 87 calcium-rich fly ash was selected in the context of resource-saving being an industrial
39
40 88 waste. The main aim is to assess the feasibility of using this novel binder for soil
41
42 89 treatment.

44 90 When addressing the feasibility of using a class of material for a novel application, there
45
46
47 91 are several important parameters to consider such as the composition, microstructure and
48
49
50 92 processing which all ultimately affect the performance-to-cost ratio of a material
51
52 93 (Askeland et al., 2011). A detailed understanding of both the composition but also the
53
54
55 94 structure of the binder across length scales is therefore required in order to control
56
57 95 materials properties through its processing.

1 96 Two main length scales of investigation can be distinguished with relevant importance.
2
3 97 A first one is the particle scale and corresponds to the identification of the different phases
4
5 98 constituting particles in terms of chemical composition and crystal structure. Important
6
7
8 99 properties of particles depend on the arrangements of atoms and types of bonding within
9
10
11 100 each phase (Clemens et al., 2008). A second scale of observation is at the level of group
12
13 101 of particles, or microstructure. Microstructural investigations for alkali activated
14
15 102 materials are of prime importance as their physical properties depend largely on their pore
16
17 103 network characteristics and microstructure (Nath et al., 2016; Lawrence and Jiang, 2017).
18
19
20 104 This is associated with the fact that the microstructure controls the transport properties of
21
22 105 the binder and the stability of the matrix when exposed to aggressive agents (van Deventer
23
24 106 et al., 2015).
25
26
27 107 In our previous study the physicochemical evolution of similar systems than those herein
28
29 108 studied was carried out i.e. identification and evolution of the constitutive phases until 28
30
31 109 days of curing time at an atomic level. It showed that the soil i.e. kaolin was not reactive.
32
33
34 110 Whereas, fly ash was partly reactive. Some of its phases such as the vitreous phase and
35
36 111 quartz were mainly unreactive, while calcium-containing phases represented the reactive
37
38 112 phases. The new compounds formed were an amorphous silicate consisting of chains
39
40 113 combined with calcium probably incorporating three-dimensional four-fold aluminium
41
42 114 environments and thenardite Na_2SO_4 (Coudert et al., 2019).
43
44
45 115 The present work ~~therefore constitutes a complementary study and focusses on the next~~
46
47 116 ~~level that is the microstructural description, . It particularly aims at providing a first step~~
48
49
50 117 ~~towards an understanding of the microstructural evolution~~ taking into account the
51
52 118 knowledge gained about the physicochemical evolution of the system.
53
54
55
56
57
58
59
60
61
62
63
64
65

1 119 The study was designed in three stages. An initial stage consisted in the identification of
2
3 120 the phases present in the reactive aluminosilicate source i.e. the original calcium-rich fly
4
5 121 ash and description of their structure, shape and size distribution. The different
6
7
8 122 constituents of fly ash being inhomogeneously reactive (Provis and Deventer, 2009), it
9
10 123 was important to identify the reactive phases around which microstructural changes were
11
12
13 124 predominant. A second stage focussed on the investigation of the microstructural
14
15 125 evolution of the alkali activated fly ash binder during the first 28 days of curing, including
16
17
18 126 (i) a description of the dispersion and arrangement of phases, (ii) an understanding of
19
20 127 which processes generate the microstructure over time and (iii) a pore network
21
22
23 128 characterisation. Fly ash being a highly inhomogeneous material (Provis and Deventer,
24
25 129 2009), a key point was to determine the homogeneity of processes across the sample at a
26
27
28 130 microscopic level. Besides, a particular emphasis was put at understanding
29
30 131 microstructural changes and processes around calcium particles which are the main
31
32
33 132 reactive phases. A third stage focussed on the interaction of the fly ash-based binder with
34
35 133 the kaolin clay to understand how the presence of kaolin modifies the microstructural
36
37
38 134 features of the system. As previously stated, kaolinite is unreactive during the alkaline
39
40 135 activation. However, because of its small size kaolinite acts as a filler of the porosity
41
42 136 (Coudert et al., 2019) and undoubtedly plays a role on the microstructural evolution. **The**
43
44 137 **effects at macroscopic level have been highlighted with reference to one dimensional**
45
46 138 **compression results, showing the improvement of the mechanical performances of the**
47
48 139 **treated soil as function of binder percentage and curing time. A final comparison between**
49
50 140 **the performance of cement treated soil with alkali activated binder treated soil has shown**
51
52
53 141 **for highlighting the effectiveness of the improvement.**
54
55
56
57 142

1
2
3
4
5
6
7
8
9
10
11
12
13
14
15
16
17
18
19
20
21
22
23
24
25
26
27
28
29
30
31
32
33
34
35
36
37
38
39
40
41
42
43
44
45
46
47
48
49
50
51
52
53
54
55
56
57
58
59
60
61
62
63
64
65

143

144 **2. Material and methods**

145 *2.1 Materials*

146 A Polish fly ash derived from hard coal and coal slime combustion in fluidised bed boiler
147 was used. Its chemical analysis is given in Table 1, and consists primarily of SiO₂, Al₂O₃
148 and CaO. The fly ash contains, approximately, 52% of particles sized lower than 45 µm
149 and 41% lower than 10 µm.

150 Speswhite kaolin provided by Imerys Minerals UK, and whose chemical composition is
151 given in Table 1 was used. It is mainly constituted of kaolinite (95%) and secondarily of
152 muscovite (4%) (Chemeda, 2015). The kaolin contains, approximately, 100 % of particles
153 sized lower than 10 µm and 80 % lower than 2 µm.

154 A unique alkaline solution was used: a sodium silicate with a mass ratio SiO₂/Na₂O of
155 1.7 and a dry mass percentage of 44%; supplied by Woellner Group and named GEOSIL
156 34417.

157

158 Table 1 - Chemical composition (wt. %) of raw fly ash and kaolin.

	SiO ₂	Al ₂ O ₃	Fe ₂ O ₃	CaO	CaO _{free} ^a	MgO	SO ₃	Na ₂ O	K ₂ O	H ₂ O	L.o.I.
Fly ash	39.4	19.8	7.4	18.6	5.2	1.8	4.1	2.0	1.8	0.0	1.7 ^b
Kaolin	49.2	34.5	1.2	0.0	0.0	0.2	0.0	0.1	1.7	13.1	12.0 ^c

159 ^a Free calcium oxide content
160 ^b L.o.I = Loss on ignition 900 °C
161 ^c L.o.I = Loss on ignition 1000 °C
162

163 *2.2 Sample preparation*

1 164 Sample preparation consisted in (i) mix of liquid sources i.e. silicate and water (ii) mix
2
3 165 of aluminosilicate powders i.e. fly ash and kaolin in the case of soil-source sample (iii)
4
5 166 mix of (i) and (ii) previously prepared.
6

7
8 167 **For microstructural analyses, two types of mixes were studied and named F100 and KF50.**
9
10 168 F100 is the fly ash-based alkali activated binder. It corresponds to a solid phase made of
11
12 169 fly ash only, whereas KF50 is the alkali activated binder treated soils and corresponds to
13
14 170 a solid phase made of 50% of fly ash and 50% of kaolin in mass.
15

16
17 171 To ensure a good workability, the amount of added water with respect to the solid mass
18
19 172 (e.g. mass of kaolin and fly ash) was fixed to 50% for all the samples. Additionally, the
20
21 173 mass ratio of alkaline solution to fly ash was fixed to 50% for all the samples, giving the
22
23 174 initial molar ratios (considering that kaolin is unreactive): $Si/Al = 2.0$, $Si/Na = 3.5$ and
24
25 175 $Al/Na = 1.8$. The Al/Na ratio was not fixed to one because of the presence of calcium
26
27 176 ions in high quantity in our system playing a role of charge compensation as well as
28
29 177 sodium.
30

31
32 178 The paste obtained was poured in closed plastic molds and cured at room temperature (20
33
34 179 °C). Samples were finally demoulded and freeze-dried at curing times of 24 hours, 3, 7
35
36 180 or 28 days.
37

38
39 181 **Samples for one dimensional compression tests were prepared with the described**
40
41 182 **technique. Three mixes have been considered in the study, namely KF10, KF20 and KF40**
42
43 183 **corresponding to a solid phase made of 10%, 20% and 40% of fly ash with reference to**
44
45 184 **dry mass of solids (fly ash+ kaolin). Remoulded samples were prepared by hand mixing**
46
47 185 **solids, alkaline solution and water at their liquid limits (i.e. $w_L=67\%$ for KF10, $w_L=60\%$**
48
49 186 **for KF20, $w_L=55\%$ for KF40). Samples were poured in the mould and placed in**
50
51
52
53
54
55
56
57
58
59
60
61
62
63
64
65

1 187 oedometer cell without compaction. Treated samples were cured for 24 hours, 7, 14, 28
2
3 188 and 60 days before mechanical testing.
4

5
6 189

7
8 190 *2.3 Methods*
9

10 191 Samples were studied by Optical and Scanning Electron Microscope from polished
11
12 192 section. Freeze-dried samples were impregnated under a vacuum with an acrylic resin
13
14 193 (LR White). The polymerisation of the resin was performed in an oven at 60 °C over 48
15
16 194 h. The samples were then polished with diamond powder. The observations from Optical
17
18 195 Microscopy were done with a Nikon LV100 polarizing optical microscope combined with
19
20 196 a ccd Nikon DS-2Mv camera and the NIS Element BS software. Whereas the
21
22 197 observations from Scanning Electron Microscope were done with a HITACHI SU5000
23
24 198 scanning electron microscope equipped with an energy-dispersive X-ray analyser
25
26 199 (Quantax microanalyser system composed of X-Flash® SDD detector and the Esprit
27
28 200 software). The polished samples were coated with carbon before the observation. The
29
30 201 microscope was operated at an accelerating voltage of 20 kV and working distances of
31
32 202 10 mm.
33
34

35 203 MIP tests were performed by a double chamber Micromeritics Autopore III apparatus. In
36
37 204 the filling apparatus (dilatometer) samples were outgassed under vacuum and then filled
38
39 205 by mercury allowing increase of absolute pressure up to ambient one. Using the same unit
40
41 206 the intrusion pressure was than raised up to approximately 200 kPa by means of
42
43 207 compressed air. The detected entrance pore diameters ranges between 134 µm and 7.3
44
45 208 µm (approximately 0.01 MPa - 0.2 MPa for a mercury contact angle of 139°). After
46
47 209 depressurisation to ambient pressure, samples were transferred to high-pressure unit,
48
49 210 where mercury pressure was increased up to 205 MPa following a previously set intrusion
50
51
52
53
54
55
56
57
58
59
60
61
62
63
64
65

1 211 program. The smallest detected entrance pore diameter was about 7 nm. Corrections to
2
3 212 pore-size distribution due to compressibility of intrusion system were applied performing
4
5
6 213 a blank test.

7
8 214 One dimensional compression tests have been performed in standard oedometer cells,
9
10 215 where vertical stress was conventionally applied in successive steps ($\Delta\sigma_v/\sigma_v = 1$) within
11
12 216 the stress interval 10 ÷ 2400 kPa. Micrometer dial gauges with an accuracy of 0.001 mm
13
14
15 217 have been used to measure vertical displacements.
16
17

18 218

19 219 **3. Results and discussion**

20
21
22
23 220 The first section of results presents the general characteristics of the raw fly ash which
24
25 221 constitutes the reactive aluminosilicate source of the mixes. The second part examines
26
27 222 the microstructural evolution of the binder. Finally, The third part focusses on the
28
29 223 description of system made by kaolin and the alkali activated binder and its mechanical
30
31 224 performance.
32
33
34

35 225

36 226 *3.1 Raw fly ash*

37
38 227 The fly ash used here contains various components. Its composition consisting of (i) a
39
40 228 vitreous phase and (ii) various crystalline phases i.e. calcium-containing minerals:
41
42 229 anhydrite CaSO_4 , calcite CaCO_3 and portlandite $\text{Ca}(\text{OH})_2$, and other minerals: quartz
43
44 230 SiO_2 , feldspar $(\text{K,Na,Ca})(\text{Si,Al})_4\text{O}_8$, hematite Fe_2O_3 and muscovite
45
46 231 $(\text{Si}_3\text{Al})\text{O}_{10}(\text{Al}_2)(\text{OH})_2\text{K}$ (Coudert et al., 2019).
47
48
49

50 232 Its particle size distribution reflects this diversity with 52 % of particles lower than 45
51
52 233 μm , 41 % of particles lower than 10 μm and 12 % of particles lower than 2 μm .
53
54
55
56
57
58
59
60
61
62
63
64
65

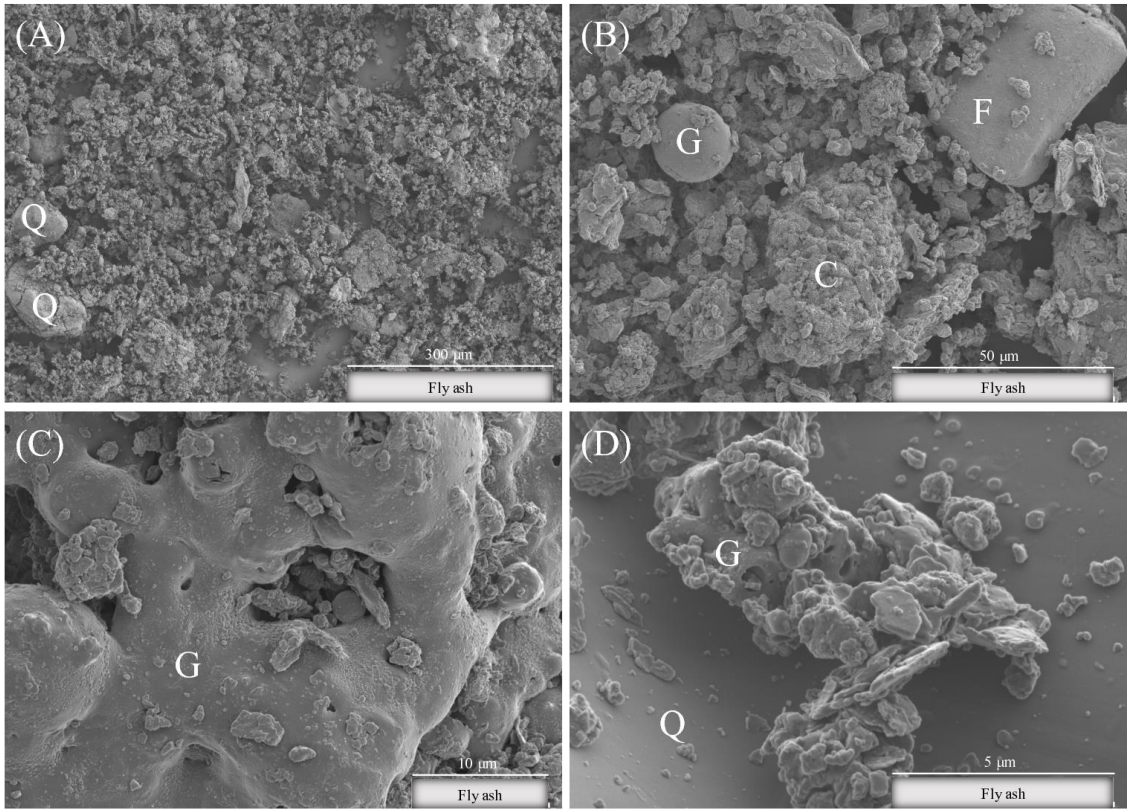
1
2
3
4
5
6
7
8
9
10
11
12
13
14
15
16
17
18
19
20
21
22
23
24
25
26
27
28
29
30
31
32
33
34
35
36
37
38
39
40
41
42
43
44
45
46
47
48
49
50
51
52
53
54
55
56
57
58
59
60
61
62
63
64
65

234 Figure 1 confirms this great variety also detectable by Scanning Electron Microscopy. In
235 fact, the fly ash presents an extremely heterogeneous microstructure with particles of
236 different shapes and ranging from 1 μm to more than 200 μm . The vitreous phase is itself
237 heterogeneous and made of (i) some spherical particles (see G Figure 1B), (ii) bigger
238 unshaped particles (see G Figure 1C) and (iii) aggregates of small particles primarily (see
239 G Figure 1D).

240 Some crystallised angular shaped minerals can also be distinguished and correspond to
241 quartz (see Q Figure 1A&D) or feldspar (see F Figure 1B).

242 Finally, regarding calcium-rich phases, our previous study showed that calcium-
243 containing minerals i.e. anhydrite CaSO_4 , calcite CaCO_3 and portlandite $\text{Ca}(\text{OH})_2$ are
244 interlaced together (Coudert et al., 2019). Especially, they are interlinked within a nodule
245 shape structure generally of 50 to 200 μm size as seen on Figure 1B (particle labelled C).

246



247

1 248 **Fig. 1** SEM micrographs of the raw fly ash; C=calcium-rich particle; F=feldspar;
2 249 G=glass; Q=quartz.
3
4 250

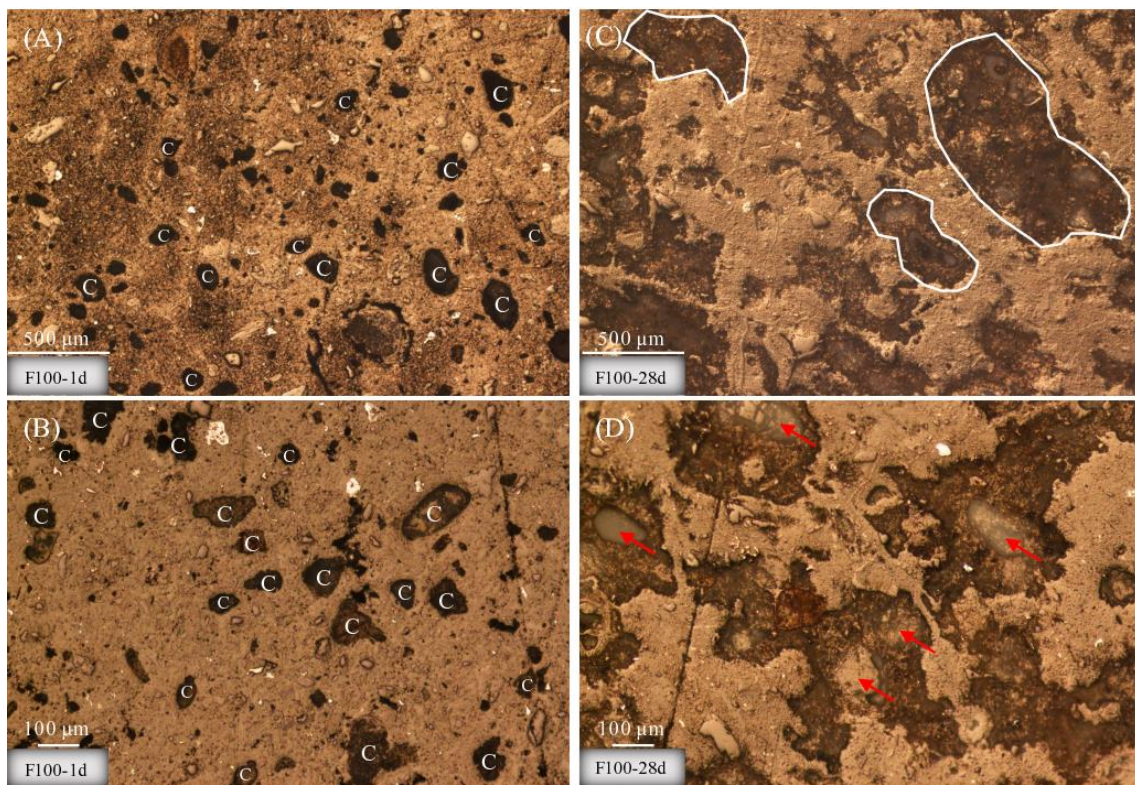
5
6 251 *3.2 Alkali activated fly ash binder*

7
8 252 *3.2.1 Optical Microscopy*

9
10 253 Figure 2 shows the microstructural evolution of the alkali activated fly ash binder over
11
12 254 time by optical microscopy. Observations were carried out until 28 days as chemical
13
14 255 reactions are fully developed at that curing time (Coudert et al., 2019).

15
16 256 After 24 hours of curing, dispersed dark spots of around 50 μm to 200 μm size are seen
17
18 257 across the overall sample (see particles labelled C on Figure 2A&B), and correspond to
19
20 258 reactive calcium-rich nodules by analogy with the previous observations of the raw fly
21
22 259 ash constituents (section 3.1). They represent approximately 15 % of the mixture.

23
24
25
26
27 260 Whereas the brown matrix includes the vitreous phase and calcium-free minerals from
28
29
30 261 fly ash.



1 **Fig. 2** Optical microscopy images of the alkali activated fly ash binder F100 (A) and (B)
2 after 24 hours, (C) and (D) at 28 days; C=calcium-rich particle.
3
4

5
6 266 By comparison, at 28 days, no dark spots are visible but instead large dark zones whose
7
8 267 edges are less well defined (see encircled areas on Figure 2C), and correspond to new
9
10 268 products formed. Figure 2D shows a closer observation of those large dark reactive areas.
11
12
13 269 The initial nodule shapes can still be distinguished at 28 days but instead of a dark spot
14
15 270 as observed at 24 hours it is a hollowed greyish structure that is seen as shown by the red
16
17
18 271 arrow (Figure 2D). This structure is associated with dissolution features over time of the
19
20 272 calcium-rich phase, and in accordance with the previous results about the
21
22
23 273 physicochemical evolution which indicate that calcium-containing phases are the main
24
25 274 reactive phases. New compounds corresponding to dark areas are therefore formed
26
27
28 275 around the hollowed dissolved calcium nodules. Those new compounds have been
29
30 276 identified in a previous study as thenardite Na_2SO_4 , and an amorphous silicate consisting
31
32
33 277 of chains combined with calcium probably incorporating three-dimensional four-fold
34
35 278 aluminium environments (Coudert et al., 2019).

36
37 279 As a consequence of those observations, the spreading of the darker areas at 28 days gives
38
39
40 280 an idea of the extent of the reaction and widening of the new compounds formation across
41
42
43 281 samples. In this system, half of the sample encompasses the new compounds and is hence
44
45 282 reactive whereas the initial calcium nodules represented only 15 % of the sample.
46
47 283 Besides, those new compounds seem homogeneously spread across the sample which
48
49
50 284 likely could give a homogeneously reinforced material at the macroscopic scale.

51
52 285 Results from optical microscopy therefore match with the observed physicochemical
53
54 286 evolution i.e. principal changes occur around calcium-rich reactive particles. That is why
55
56
57
58
59
60
61
62
63
64
65

1 287 the next session focusses on the in-situ microstructural transformation of calcium-rich
2
3 288 phases induced by the alkaline solution.
4

5
6 289

7
8 290 *3.2.2 Scanning Electron Microscopy (SEM)*
9

10 291 Figure 3 shows microstructural observations from a polished section and combined
11
12 292 chemical mappings of the alkali activated fly ash binder after 24 hours of curing.
13

14 293 Chemical mappings on Figure 3B&C indicate the presence of a calcium-rich nodule
15
16 294 labelled 1 on Figure 3A and predominantly made of calcium and sulphur. Additionally,
17
18 295 those calcium-rich particles display a granular aspect on their surface.
19
20

21
22 296 Surrounding this calcium-rich particle, the area labelled 2 on Figure 3A corresponds to a
23

24
25 297 porous zone distinguishable by the presence of dense black areas characteristic of the
26

27
28 298 filling resin of low atomic mass. Chemical mappings of that porous zone show an
29

30 299 enrichment in silicon and sodium (Figure 3D&E) indicating the presence of the sodium-
31

32 300 silicate Na_2SiO_3 alkaline solution at that short curing time. Additionally, filament like
33

34
35 301 structures are observed within that area (see red arrow on Figure 3A), and considered as
36

37 302 the beginning of the secondary phases formation i.e. the amorphous silicate consisting of
38

39
40 303 chains combined with calcium and potentially aluminium. In fact, a former study about
41

42 304 cementitious microstructures has shown the formation of similar arrangements associated
43

44
45 305 with Calcium Silicate Hydrates whose structure strongly resembles the one of our newly
46

47 306 formed chains (Scrivener, 2004). Moreover, it appears that those filament structures are
48

49 307 stacked around particles corresponding to the initiation of the reaction process after 24
50

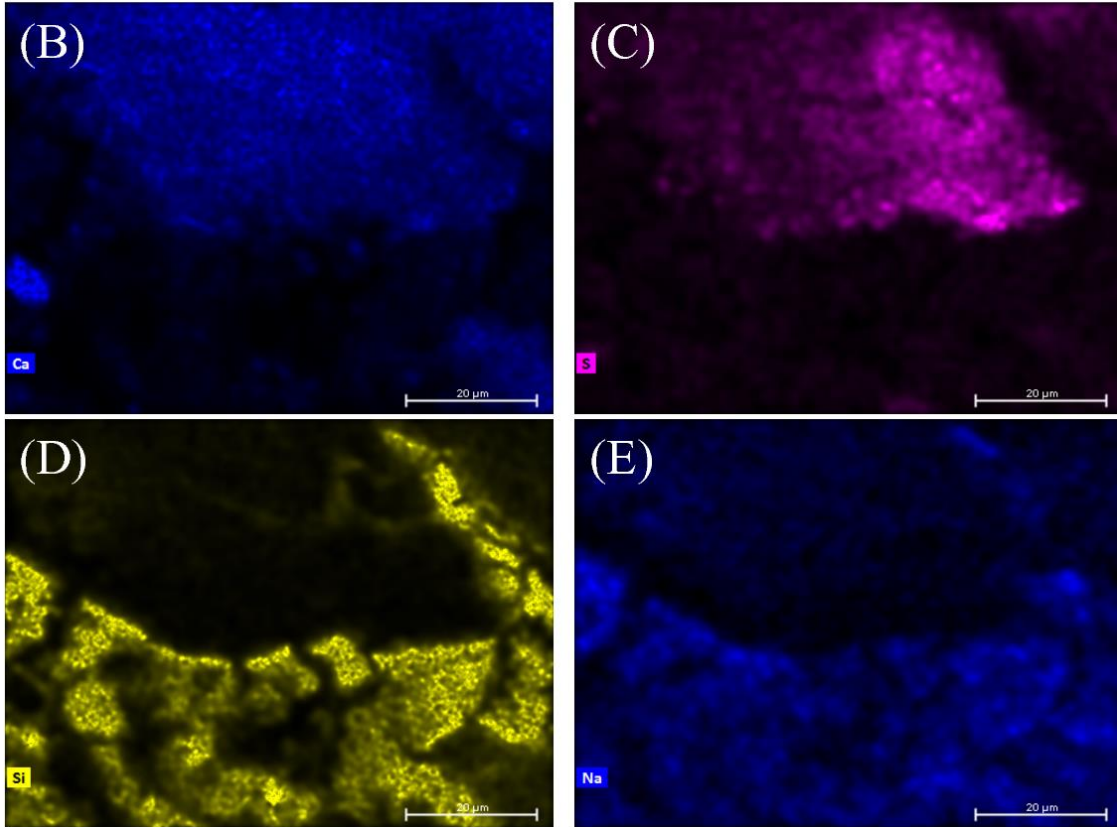
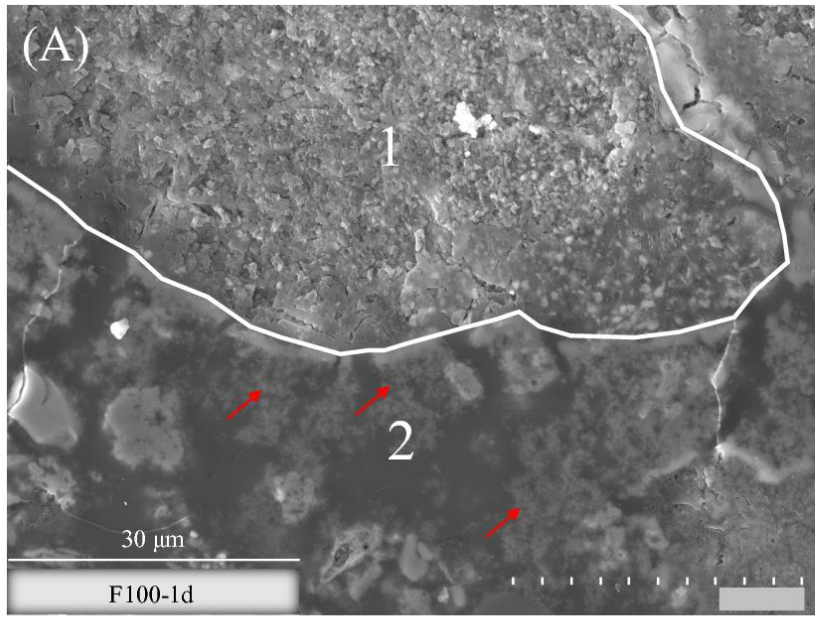
51
52 308 hours of curing.
53

54 309 Figure 4 also shows microstructural observations of the alkali activated fly ash binder
55

56
57 310 after 24 hours of curing, and particularly illustrates the microstructural difference
58
59
60
61
62
63
64
65

1 311 between a calcium-rich particle and a particle from the vitreous phase both originally
2
3 312 present in the fly ash. They can both be distinguished by SEM by their chemical
4
5
6 313 composition and microstructural features. Regarding calcium-rich particles, they present
7
8 314 a nodule shape with a granular surface (see 3 on Figure 4A) as previously observed
9
10 315 (Figure 3A). Whereas particles from the vitreous phase display a vesicular structure (see
11
12
13 316 1 on Figure 4A) and can be distinguished using chemical mappings by their enrichment
14
15 317 in silicon and aluminium (Figure 4D&E).
16
17
18 318 In between those two particles, a porous area labelled 2 on Figure 4A and with filament
19
20 319 like structures can once again be observed and evidences the initiation of the reaction
21
22
23 320 processes. Consequently, from Figure 3 as from Figure 4 it is noticeable that the alkali
24
25 321 activated binder after 24 hours of curing presents a high porosity created by the fly ash
26
27 322 grains of various sizes and that is filled by water, alkaline solution, and the new product
28
29 323 starting to be formed.
30
31
32 324
33
34
35
36
37
38
39
40
41
42
43
44
45
46
47
48
49
50
51
52
53
54
55
56
57
58
59
60
61
62
63
64
65

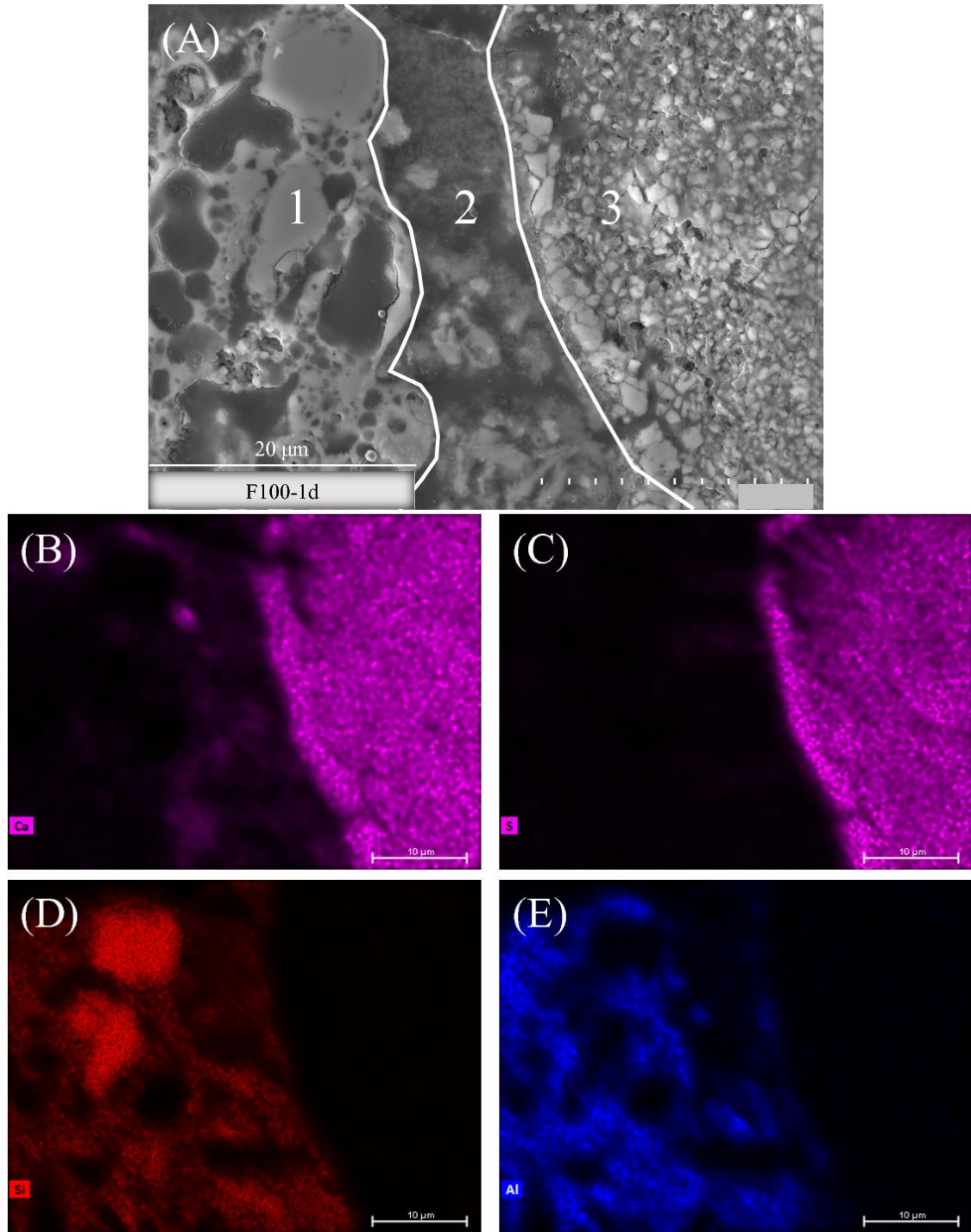
1
2
3
4
5
6
7
8
9
10
11
12
13
14
15
16
17
18
19
20
21
22
23
24
25
26
27
28
29
30
31
32
33
34
35
36
37
38
39
40
41
42
43
44
45
46
47
48
49
50
51
52
53
54
55
56
57
58
59
60
61
62
63
64
65



325
326
327
328
329

Fig. 3 SEM observations of the alkali activated fly ash binder F100 after 24 hours of curing: (A) SEM micrograph, and chemical mappings of: (B) calcium, (C) sulphur, (D) silicon and (E) sodium.

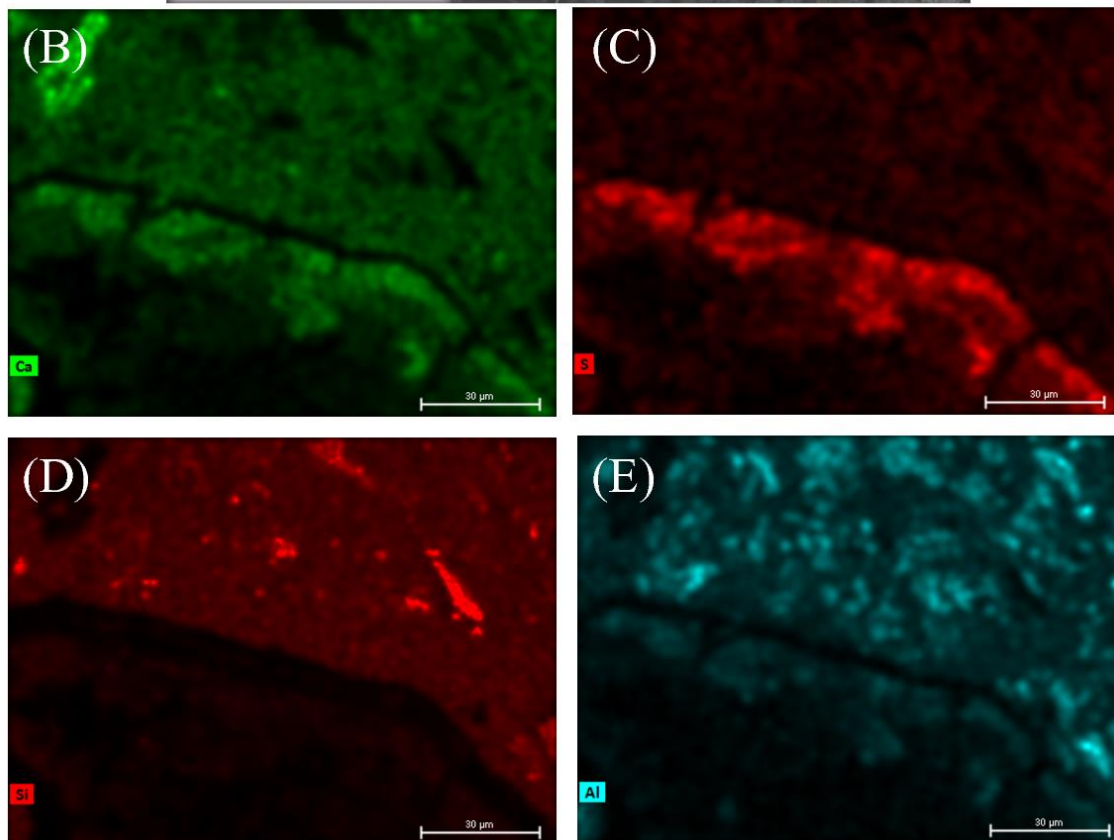
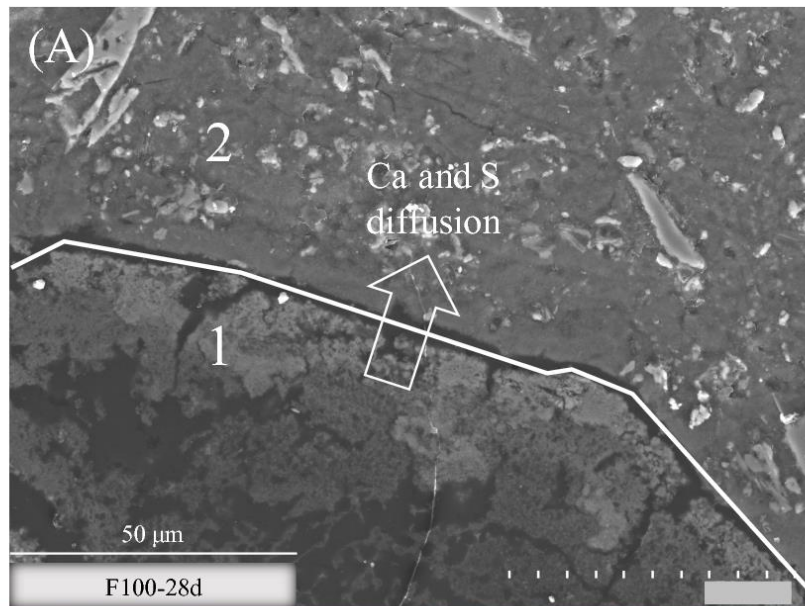
1
2
3
4
5
6
7
8
9
10
11
12
13
14
15
16
17
18
19
20
21
22
23
24
25
26
27
28
29
30
31
32
33
34
35
36
37
38
39
40
41
42
43
44
45
46
47
48
49
50
51
52
53
54
55
56
57
58
59
60
61
62
63
64
65



330
331
332
333
334

Fig. 4 SEM observations of the alkali activated fly ash binder F100 after 24 hours of curing: (A) SEM micrograph, and chemical mappings of: (B) calcium, (C) sulphur, (D) silicon and (E) aluminium

1 335 Figure 5 shows SEM observations and combined chemical mappings of the alkali
2
3 336 activated fly ash binder after 28 days of curing. It especially focuses on the interface
4
5
6 337 between a calcium-rich nodule labelled 1 and the surrounding matrix labelled 2.
7
8 338 Regarding the calcium-rich nodule, it displays a hollowed structure, especially in its
9
10 339 centre, and as similarly observed previously by optical microscopy in section 3.2.1. In
11
12
13 340 addition, those hollowed structures show dense black zones indicating the presence of
14
15 341 filling resin and therefore porosity. Those structural characteristics strongly contrast with
16
17 342 calcium nodules after 24 hours presenting a granular surface, and are attributed to the
18
19 343 dissolution of calcium-rich phases over time leaving behind a porous body. It is supported
20
21 344 by chemical mappings on Figure 5B&C showing a strong impoverishment in calcium and
22
23 345 sulphur in the hollowed area with respect to nodules after 24 hours.
24
25
26
27 346 An enrichment in calcium and sulphur is seen in the outer part of the nodule suggesting
28
29 347 a mechanism of dissolution of calcium and sulphur moving from the calcium nodules to
30
31 348 the matrix. Moreover, few silicon supplied in that system by the alkaline solution is
32
33 349 detected above the edges of the calcium nodule and inside implying that the alkaline
34
35 350 solution penetrates through the calcium-nodule accelerating its dissolution. The
36
37 351 coloration due to the silicon presence inside the nodule is few marked as unreactive quartz
38
39 352 which corresponds to intensely coloured and well defined edges spots on the silicon
40
41 353 chemical mapping (Figure 5D) are present in the matrix and induces a rescaling of the
42
43 354 silicon coloration.
44
45
46
47
48
49 355
50
51
52
53
54
55
56
57
58
59
60
61
62
63
64
65



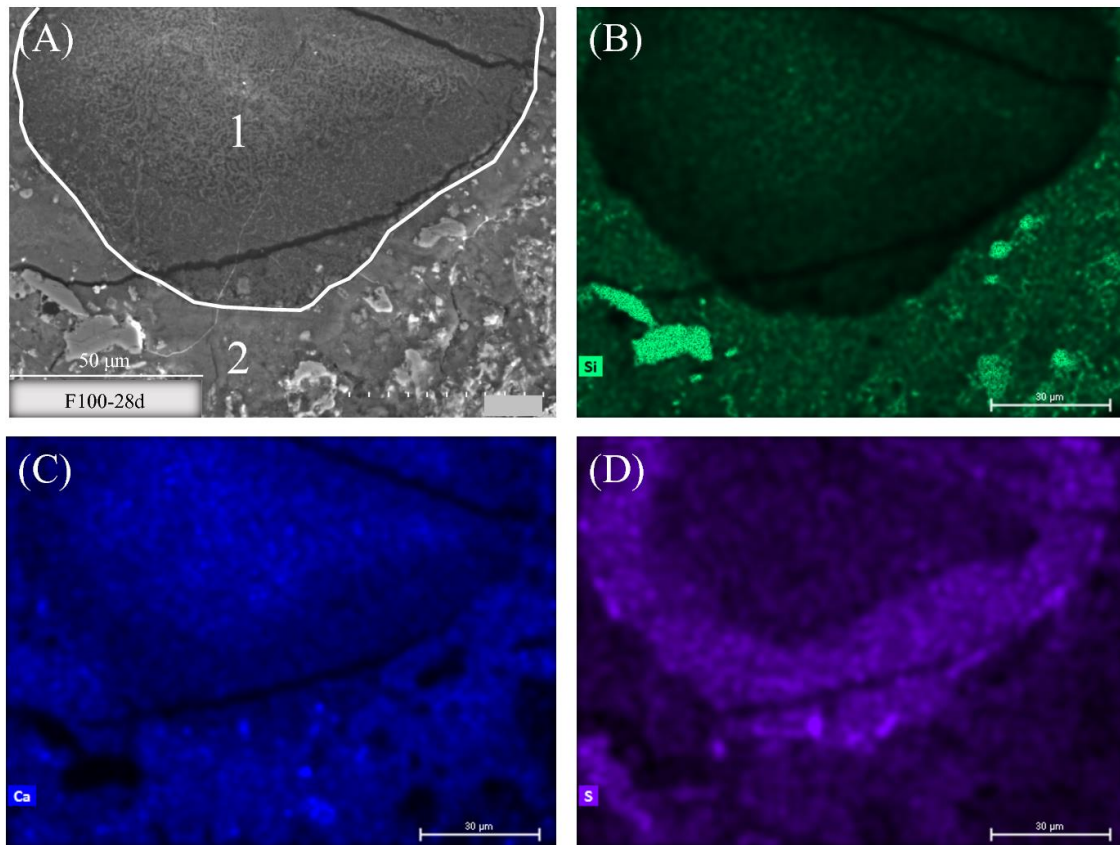
356

357 **Fig. 5** SEM observations of the alkali activated fly ash binder F100 at 28 days: (A) SEM
 358 micrograph, and chemical mappings of: (B) calcium, (C) sulphur, (D) silicon and (E)
 359 aluminium.

360

361 Regarding the area surrounding the calcium nodule labelled 1, it is massive and presents
 362 a low porosity compared to the binder after 24 hours. It corresponds to the area where

1 363 new products are formed. Its chemical mappings show a high content of calcium and
2
3 364 silicon which is in accordance with the physicochemical investigation that showed the
4
5 365 formation of silicate chains combined with calcium over time. The wide diffusion of
6
7
8 366 calcium into the matrix is clearly seen from Figure 5 when compared to the binder after
9
10 367 24 hours of curing for which calcium is contained and restrained to the nodule surface
11
12 368 (see Figure 3 and Figure 4). Concerning sulphur elements, as well initially present in the
13
14 369 nodule in the form of anhydrite CaSO_4 , its dissolution occurs in a lesser extent and seems
15
16 370 stopped to the outer part of the nodule at 28 days (Figure 5C). The physicochemical
17
18 371 evolution of this system showed that dissolved sulphur combine with sodium to form
19
20 372 thenardite Na_2SO_4 at 28 days (Coudert et al., 2019). Consequently, the presence of
21
22 373 thenardite is restrained to small areas around the calcium-rich particles, whereas silicate
23
24 374 two-dimensional chains combined with calcium are widely spread all around the calcium
25
26 375 nodules. The formation of this thenardite crust limited around calcium nodules can be
27
28 376 explained by the low amount of sulphur elements compared to calcium (see chemical
29
30 377 composition of the raw fly ash in Table 1), that already all precipitated in this small area.
31
32 378 The conjoint chemical mapping of sodium to localise thenardite is not shown here as
33
34 379 sodium is a volatile element for which it is difficult to get a chemical mapping showing
35
36 380 a reliable representativeness of sodium dispersion.
37
38 381 Finally, important crackings are observed around calcium-rich particle as seen on Figure
39
40 382 5 and are associated with shrinkage processes frequently observed for alkali activated
41
42 383 materials (Fang et al., 2018).
43
44
45
46
47
48
49
50
51
52
53
54
55
56
57
58
59
60
61
62
63
64
65

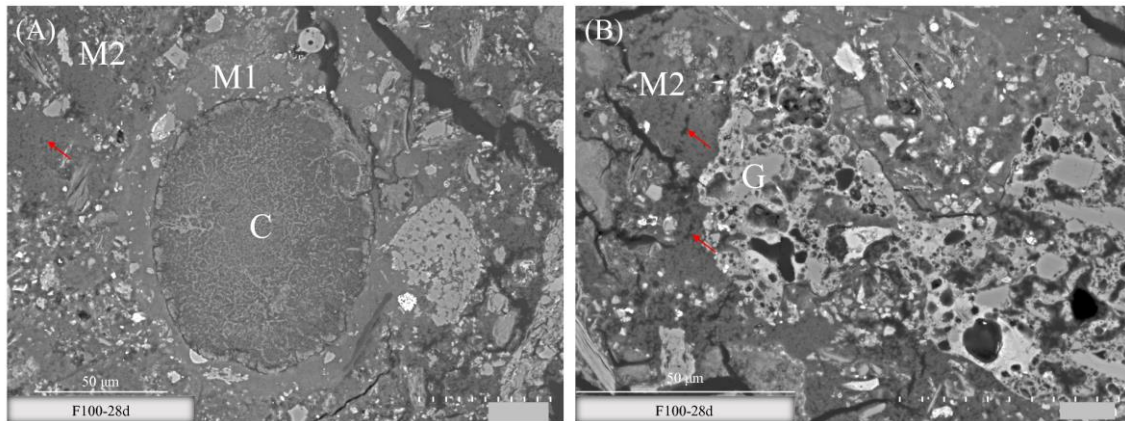


385

386 **Fig. 6** SEM observations of the alkali activated fly ash binder F100 at 28 days: (A) SEM
 387 micrograph, and chemical mappings of: (B) silicon, (C) calcium and (D) sulphur.
 388

389 Figure 6 shows the alkali activated fly ash binder at 28 days, and more particularly a
 390 calcium-rich reactive nodule labelled 1 surrounded by a dense matrix comprising both
 391 new products and non-reactive phases such as quartz or aluminium containing minerals.
 392 However, in that case the extent of dissolution of the calcium nodule appears lower as the
 393 hollowed structure is not seen but rather a granular microstructure similar of those
 394 observed after 24 hours. Chemical mappings show that the dissolution of that nodule did
 395 start as calcium is widely diffused into the matrix, and an enrichment in sulphur is once
 396 again seen in the outer part of the nodule. Nevertheless, the dissolution is at a different
 397 stage as calcium is still strongly detected in the centre of the nodule and no hollowed
 398 structure is noticed. Consequently, the extent of reaction of a calcium-rich nodule varies

399 locally. A lesser porosity of the calcium nodule could for instance moderates its
400 dissolution. Its size, its content in calcium and sulphur or else the amount of water locally
401 available are also all parameters that may locally affect the extent of reaction.



403
404 **Fig. 7** Comparing SEM microstructural changes of the alkali activated fly ash binder F100
405 at 28 days around: (A) a calcium-rich nodule labelled C, and (B) a particle from the
406 vitreous phase labelled G; M1 = dense matrix; M2 = porous matrix

408 Figure 7 shows micrographs of the alkali activated binder after 28 days, and more
409 particularly the difference between microstructural changes occurring (A) around a
410 calcium rich particle identified as the dark reactive zones in optical microscopy, and
411 around a glassy particle identified as the brown matrix in optical microscopy.

412 It is worth noting that although amorphous and extremely porous the vesicular glassy
413 phases reaction is negligible as its vesicular structure remains similar to the one after 24
414 hours (see Figure 4A, particle labelled 1). This observation is in accordance with our
415 previous study about the physicochemical evolution of that system which shows that the
416 vitreous phase mainly remains unreactive (Coudert et al., 2019). It is well known that the
417 rate of reaction of the aluminosilicate vitreous phases of fly ash at ambient temperature
418 following alkaline activation is slow and takes several days (Provis and Deventer, 2009;
419 Wardhono et al., 2015). Whereas the calcium-rich particles in our mixes are extremely

1 420 and quickly reactive as the formation of new products containing calcium already starts
2
3 421 after 24 hours as seen previously in Figure 3. Hence, the faster reaction of calcium-rich
4
5 422 particles leads to the formation of dense products (as seen in Figure 7A) freezing the
6
7
8 423 system and preventing the later reaction of the aluminosilicate glassy phases.
9

10 424 Massive and dense areas are observed around calcium-rich nodules (see Figure 7A), while
11
12
13 425 a more porous matrix is seen around vesicular glassy phases (see Figure 7B). The
14
15 426 comparison in Figure 7 hence evidences that there are different matrices forming the
16
17
18 427 alkali activated treated soil: (i) a first circularly-shaped matrix identified around calcium-
19
20 428 rich particles and presenting a high density labelled M1 on Figure 7A, and (ii) a more
21
22
23 429 porous matrix less bonded labelled M2 on Figure 7A&B whose pores are shown by red
24
25 430 arrows, and located around glassy phases of lower reactivity. A previous investigation of
26
27
28 431 that system by Nuclear Magnetic Resonance showed the signature of only one type of
29
30 432 silicate chains combined with calcium and spreaded into the matrix as a new compound
31
32
33 433 (Coudert et al., 2019). Therefore, Scanning Electron Microscopy provides an additional
34
35 434 information: although the atomic structure of the silicate chain remains similar, the
36
37
38 435 arrangement of those phases in the matrix varies following the local environment.
39
40 436 Similarly to the great heterogeneity of fly ash, the matrix formed is also highly
41
42 437 heterogeneous.

44
45 438

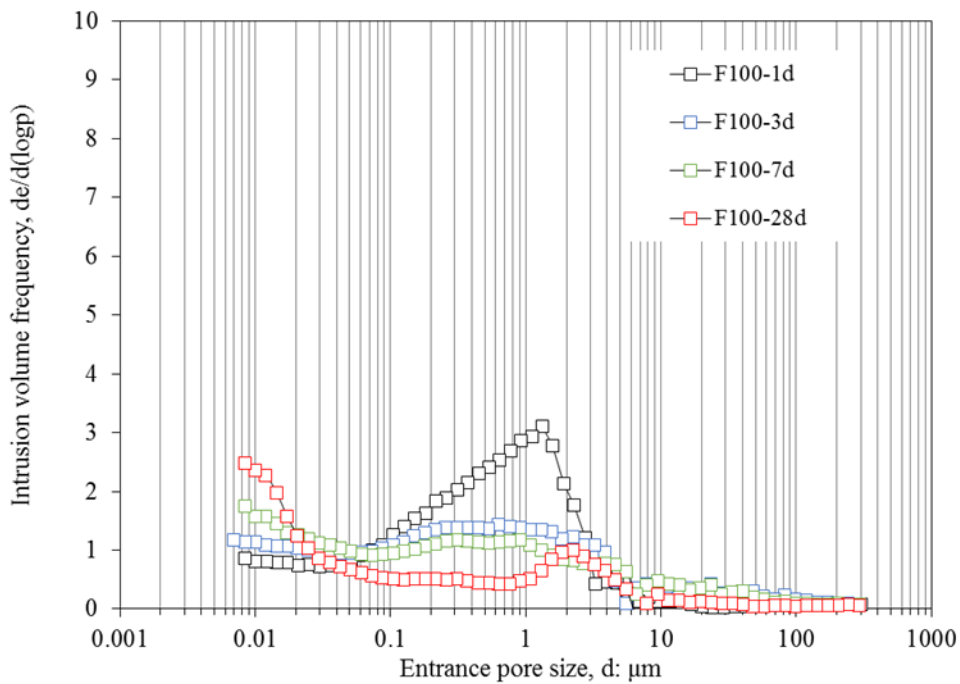
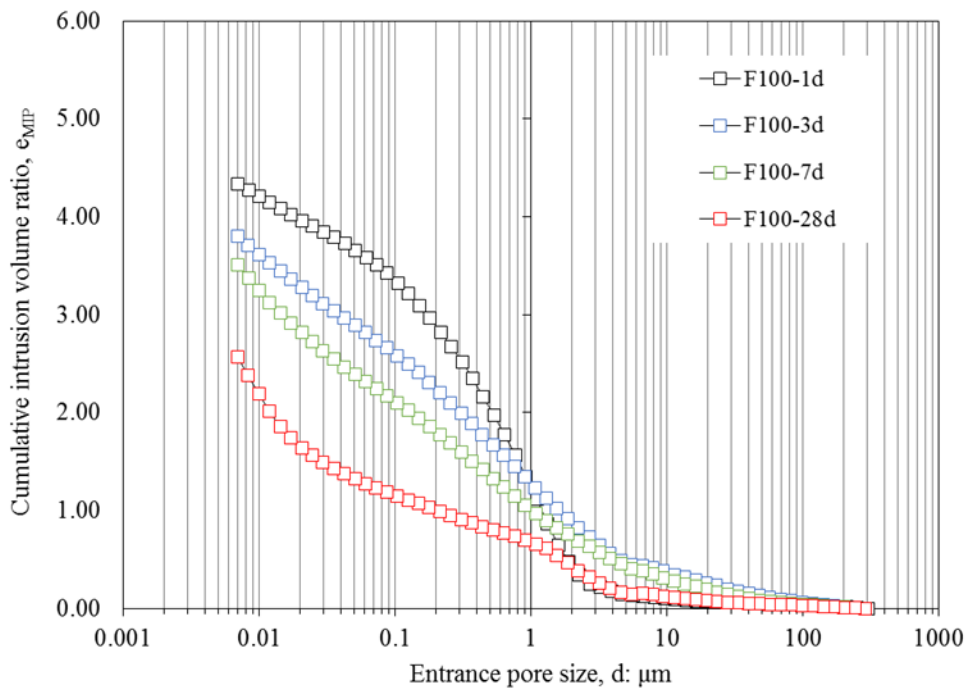
47 439 *3.2.3 Mercury Intrusion Porosimetry (MIP)*

48
49 440 Figure 8A shows cumulative curves of mercury intrusion porosimetry tests of the alkali
50
51
52 441 activated fly ash binder over time. The longer the curing time, the lower is the cumulative
53
54 442 intrusion volume ratio implying a progressive decrease of the overall porosity over time,
55
56
57 443 and in accordance with the general tendencies observed by SEM in section 3.2.2. It is
58
59
60
61
62
63
64
65

1 444 owed to the progressive filling of pores by the new compounds formed i.e. calcium-
2
3 445 silicate two-dimensional chains and thenardite.
4

5
6 446 Figure 8B shows the frequency distributions of pore entrance diameters belonging to the
7
8 447 alkali activated fly ash binder over time. Samples at 24 hours, 3 and 7 days all show one
9
10 448 broad modal pore sizes between 0.05 μm and 3 μm . However, from 24 hours to 7 days
11
12 449 the frequency of those pores progressively decreases due to their filling by newly formed
13
14 450 compounds. Whereas, at 28 days a narrower modal pore size at about 2 μm is observed.
15
16 451 By analogy with SEM pictures, those remaining pores at 2 μm could correspond to either
17
18 452 the size of the cracks seen around calcium particles and associated with shrinkage as
19
20 453 previously observed on Figure 5, the porosity formed within calcium nodules after their
21
22 454 dissolution also seen on Figure 5, or else pores that have not been filled by new
23
24 455 compounds within the more porous matrix previously identified and labelled M2 on
25
26 456 Figure 7.
27
28
29
30
31

32 457 Finally, in the area of lower pore size i.e. below 20 nm the increase of frequency over
33
34 458 time corresponds to the formation of a new class of pores inside the matrix. It is associated
35
36 459 with the formation of the silicate two-dimensional chains combined with calcium, whose
37
38 460 structure resembles those of Calcium-Silicate Hydrates (i.e. C-S-H phases commonly
39
40 461 found in Portland cement) known for possessing an intrinsic porosity of a nanometer size
41
42 462 (Muller, 2014). However, this small new class of pores cannot be fully probed by MIP
43
44 463 technique whose detection limit in the small entrance pore size is of 7 nm.
45
46
47
48
49
50
51
52
53
54
55
56
57
58
59
60
61
62
63
64
65



464

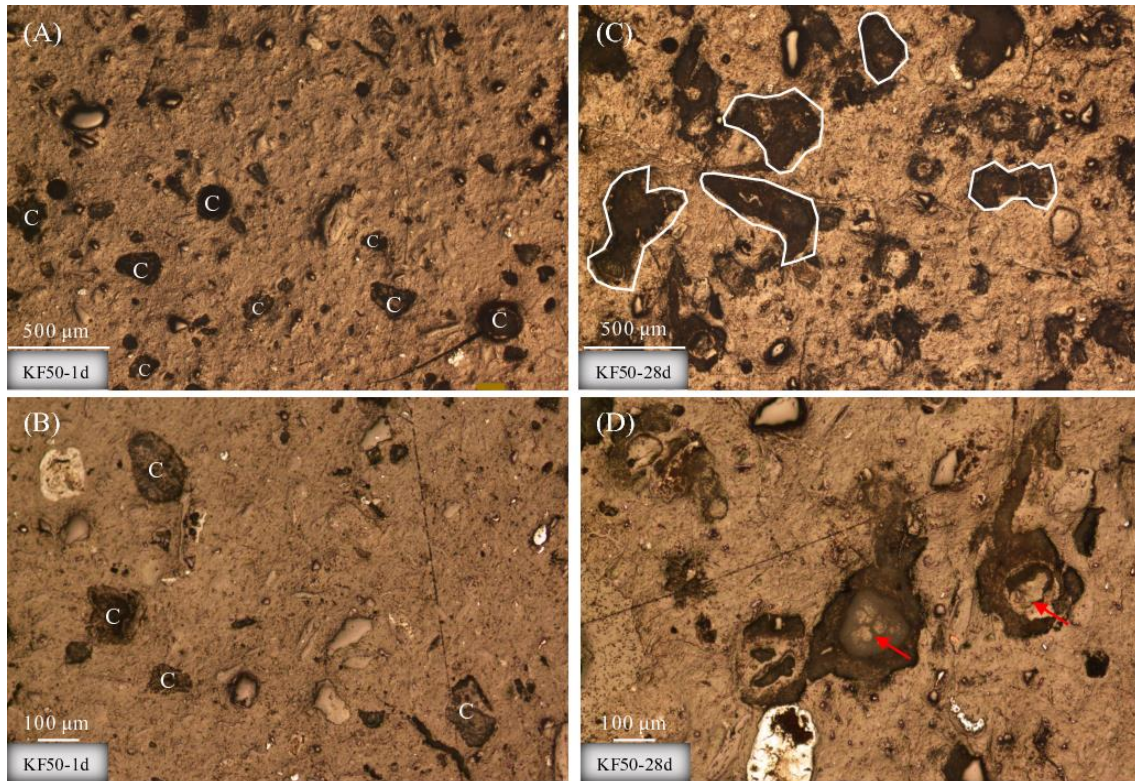
465 **Fig. 8** Comparing mercury intrusion porosimeter tests of the alkali activated fly ash binder
 466 F100 over time and in terms of (A) cumulative intrusion volume ratios, (B) intrusion
 467 volume frequency ratios as a function of entrance pore size.

468

469

470 *3.3 Interaction between the alkali activated fly ash binder and kaolin*

1 471 The following section aims at understanding the interaction between kaolin and the alkali
2
3 472 activated fly ash binder previously described. Our former study focussing on the
4
5
6 473 physicochemical evolution of the same mixes herein studied showed that kaolin was not
7
8 474 reactive during alkaline activation and did not modify the reaction sequence when
9
10 475 compared to the one of the alkali activated fly ash binder alone (Coudert et al., 2019).
11
12 476 Accordingly, similar mechanisms of ions dissolution precipitation from the calcium-rich
13
14 477 particles into the matrix leading to the formation of new products also occur in the alkali
15
16 478 activated fly ash binder treated soil as previously described for the binder in section 3.2.2,
17
18 479 and hence will not be detailed here.
19
20
21 480 Regarding the pore network structure, our previous study also showed that kaolinite
22
23 481 platelets were homogeneously spread across the matrix. This section consequently aims
24
25 482 at giving a deeper insight of the influence of kaolin on the microstructure with respect to
26
27 483 the binder alone.
28
29
30 484 Figure 9 shows microstructural observations of the alkali activated fly ash binder treated
31
32 485 soil over time by optical microscopy. Similarly, to the alkali activated fly ash binder, after
33
34 486 24 hours of curing, dispersed dark spots corresponding to calcium-rich nodules are seen
35
36 487 across the overall sample, whereas at 28 days larger dark zones encompassing the newly
37
38 488 formed compounds have grown around those nodules. Hollowed greyish nodule
39
40 489 structures at 28 days can also be distinguished as for the binder and associated with the
41
42 490 dissolution of calcium-rich particles.
43
44
45
46
47
48
49
50
51
52
53
54
55
56
57
58
59
60
61
62
63
64
65



492

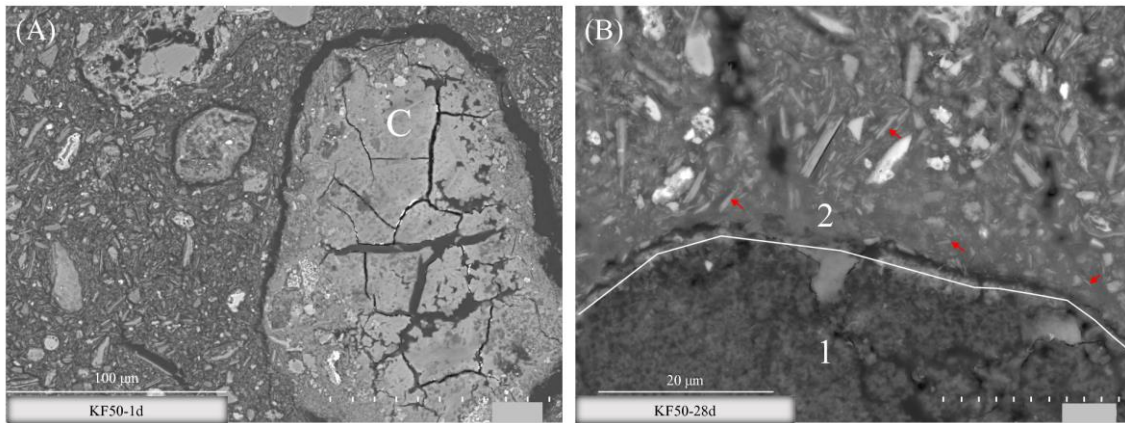
493 **Fig. 9** Optical microscopy images of the alkali activated fly ash binder treated soil KF50
 494 (A) and (B) after 24 hours, (C) and (D) at 28 days, C=calcium-rich particle.
 495

496 The widening of darker zones which indicates the extent of reaction is lesser than the
 497 binder and represents around $\frac{1}{4}$ of the sample. This is consistent with the proportions of
 498 aluminosilicate solid considering that half of fly ash containing the reactive calcium
 499 nodules has been replaced by non-reactive kaolin in this soil-binder mixture.
 500 Consequently, the growth and development of new products into the available spaces
 501 does not seem influenced by the presence of kaolin.

502 Figure 10 shows micrographs of the alkali activated binder treated soil. After 24 hours
 503 crackings around and inside calcium nodules are seen (see particle C on Figure 10A), and
 504 associated to shrinkage similarly to the alkali activated fly ash binder at 28 days. The
 505 treated soil at 28 days however shows less marked crackings as shown on Figure 10B
 506 which focusses on the interface between a calcium-rich nodule labelled 1 and the

1 507 surrounding dense matrix labelled 2. It is attributed to the presence of kaolinite acting as
2
3 508 a filler at the periphery of the calcium-rich nodules (see red arrows on Figure 10B
4
5
6 509 showing kaolinite platelets).

7
8 510



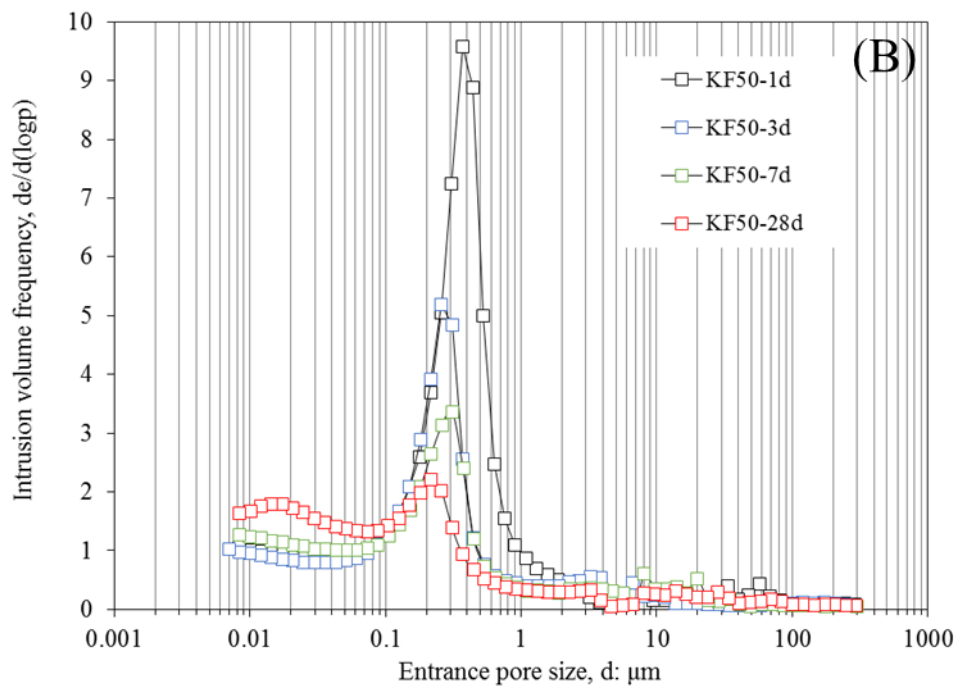
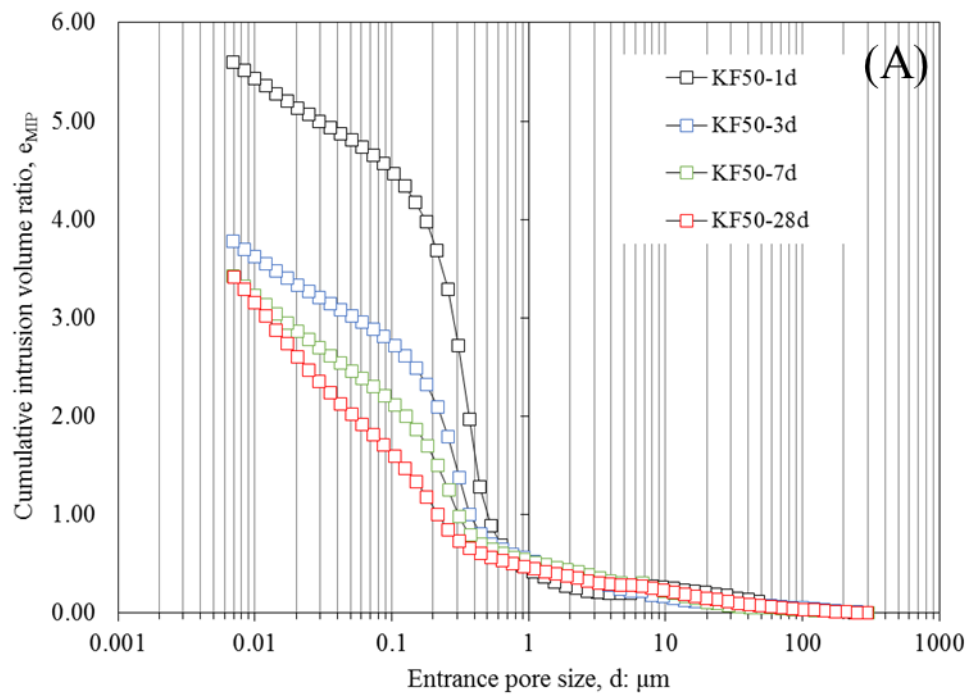
24 511

26 512 **Fig. 10** SEM micrographs of the alkali activated fly ash binder treated soil KF50 at (A)
27 513 24 hours and (B) 28 days.

28 514

31 515 Figure 11A shows cumulative curves of mercury intrusion porosimetry tests of the alkali
32
33 516 activated fly ash binder treated kaolin over time. Similarly to what was observed for the
34
35 517 alkali activated binder, a decrease of the total porosity is detected over time.

38 518 Figure 11B shows the frequency distributions of pore entrance diameters belonging to the
39
40 519 treated soil over curing time. Similarly to the alkali activated fly ash binder, the treated
41
42 520 soil at 24 hours shows one modal pore sizes. Nevertheless, compared to the binder it is
43
44 521 associated with a lower entrance pore size value around 0.4 μm and a much thinner peak.
45
46 522 The non-presence of a wide class of pores between 0.05 μm and 3 μm at 24 hours as seen
47
48 523 for the alkali activated fly ash binder is associated with the filling of the spaces between
49
50 524 the coarse grains of fly ash by the small sized kaolinite platelets. At 24 hours, kaolin
51
52 525 therefore leads the organisation of the system microstructure as the typical pattern of
53
54 526 kaolin (i.e. a monomodal curve with a peak around 0.4 μm) is shaping the curve.



527

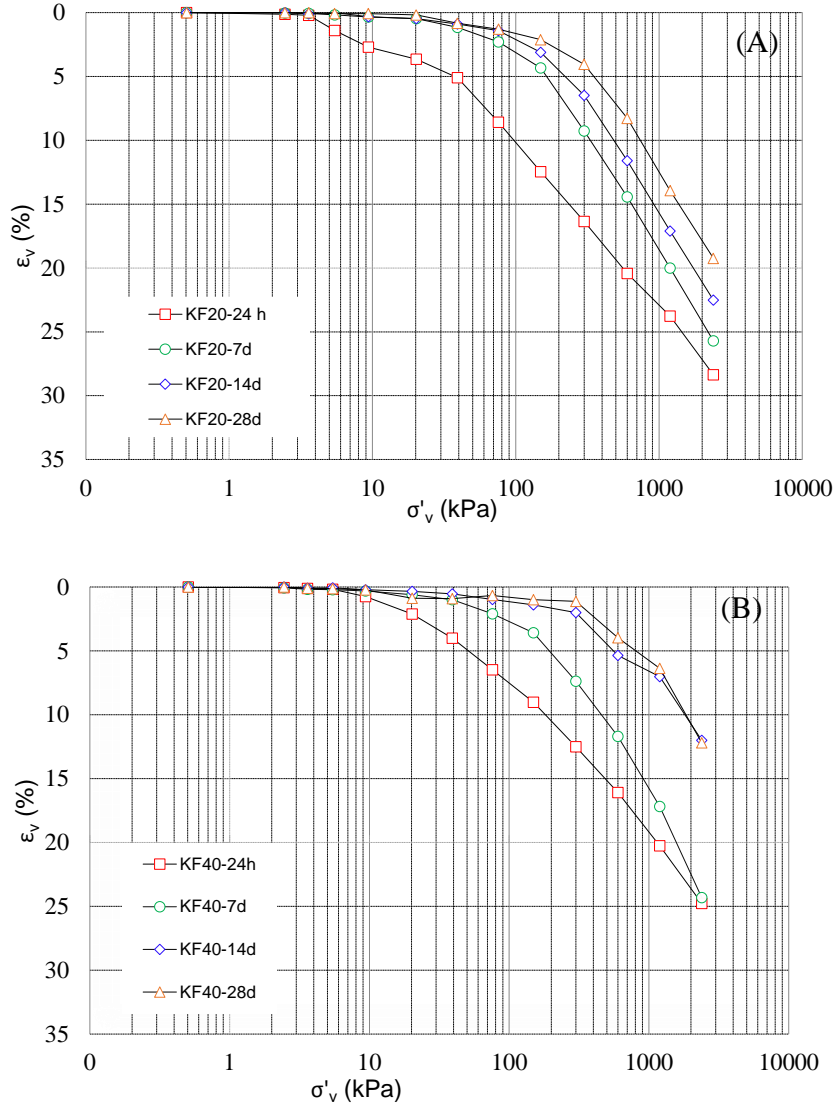
528 **Fig. 11** Comparing mercury intrusion porosimeter tests of the alkali activated fly ash
 529 binder treated soil KF50 over time and in terms of (A) cumulative intrusion volume ratios,
 530 (B) intrusion volume frequency ratios as a function of entrance pore size.
 531

1 532 Increasing the curing time, the filling of largest pores around the peak is seen as for the
2
3 533 binder and due to the progressive filling of those pores by the newly products formed. A
4
5
6 534 little shift of the residual peak towards smaller entrance diameters is also observed.
7

8 535 Finally, the formation of a new class of pores in the area of lower pore size i.e. below 30
9
10 536 nm is observed between 7 and 28 days of curing. Similarly to the binder, it is associated
11
12
13 537 with the intrinsic porosity of the newly formed silicate-calcium chains. The delay in
14
15
16 538 detection compared to the binder is due to the lower amount of phases formed for that
17
18 539 system.
19

20 540 Figure 12 shows the results of one dimensional compression tests on KF20 and KF40
21
22 541 treated samples at increasing curing times, namely 24h, 7, 14 and 28 days. Addition of
23
24
25 542 alkali activated binder induces an overall reduction of compressibility of the treated
26
27
28 543 samples, with reduced volume strains for reference vertical stresses. The reduction is
29
30 544 more relevant for increasing curing times, showing the stiffer behaviour of the treated
31
32
33 545 sample. Coupled with the reduction of compressibility, an increase of yield stress of the
34
35 546 samples is observed. The transition from a reversible behaviour to an irreversible one is
36
37
38 547 shifted (yield stress) to higher vertical stresses. The shift is more relevant for higher
39
40 548 amount of binder and at increasing curing time, revealing the reactivity of the binder to
41
42
43 549 promote an improvement of the mechanical response of the treated soil. For stress levels
44
45 550 higher than yield stress, treated samples show a higher compressibility coefficient (i.e.
46
47
48 551 slope of the compressibility curve), depending on the destructure stage induced by
49
50 552 load increase, more evident for longer curing times and higher binder content. As a
51
52 553 confirmation, in Figure 13 the compressive behaviour of treated samples is reported as
53
54
55 554 function of binder contents. Sample prepared at 10%, 20% and 40% of alkali activated
56
57 555 fly ash and cured for 24 hours before testing show a progressive improvement mainly
58
59
60
61
62
63
64
65

1 556 related to the amount of new compounds forming over time. Compressibility curves show
 2
 3 557 a reduction of compressibility evidenced by the relevant decrease of volume strains and
 4
 5
 6 558 an increase yield stresses of the treated samples, whose extent depends on binder content.



559
 560
 561 **Fig. 12** One dimensional compression curves of alkali activated binder treated samples at
 562 24 h, 7, 14 and 28 days of curing: (A) KF20; (B) KF40.
 563

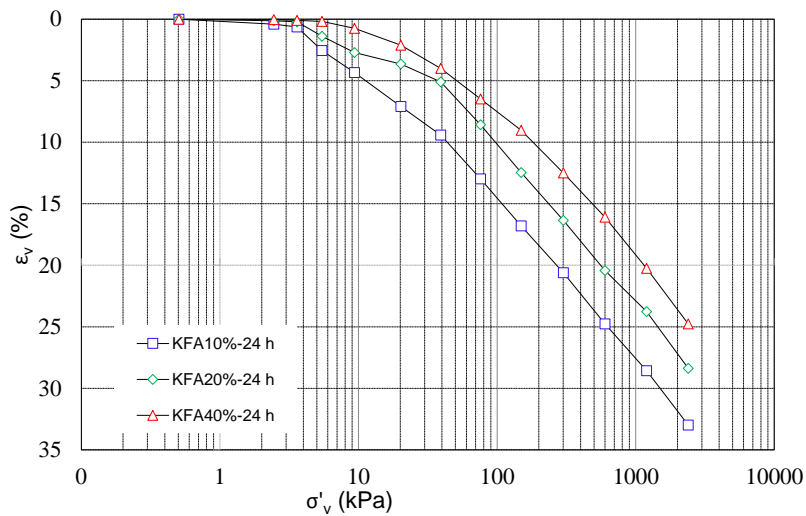


Fig. 13 One dimensional compression curves of treated samples as function of binder contents (i.e. KF10, KF20, KF40) at 24 hours of curing.

3.4 Comparison with Portland cement

This last section focusses on a comparison with microstructural development in Portland cement for which the mechanisms involved appear alike. This comparison particularly helps at providing a better understanding of (i) how microstructures are formed and (ii) interpreting the short and long-term performances of the treated soil regarding the evolution of the binder over time. **At macroscopic level, the effectiveness of alkali activated binder soil treatment has been highlighted by comparison with mechanical performance induced by Portland cement.**

3.4.1 Processes generating the microstructure

In cement systems, the dissolution of cement particles releases ions into the pore solution which then combine with water to form mainly Calcium Silicate Hydrates C-S-H (Muller, 2014). In a similar way, in our alkali activated binder, the dissolution of calcium-rich particles from fly ash releases calcium cations into the pore solution which then combine with water and silicon anions from the alkaline solution to form silicate two-

1 583 dimensional chains combined with calcium. A former investigation by Nuclear Magnetic
2
3 584 Resonance nevertheless showed that the chains structure is slightly different from C–S–
4
5 585 H, namely they are not well organized, of high length and may incorporate aluminum in
6
7
8 586 a three dimensional environment which has not been described in literature yet (Coudert
9
10
11 587 et al., 2019).

12
13 588 Secondly, it was reported for cement systems that the first Calcium Silicate Hydrates C–
14
15 589 S–H cover cement grains and further grow into the available space. All cement grains are
16
17
18 590 therefore surrounded by a shell of C–S–H (Scrivener, 2004). Again similarly in this study,
19
20
21 591 optical microscopy images clearly show the development and growth of new products
22
23 592 around calcium-rich reactive particles suggesting a similar mechanism.

24
25 593 Furthermore, Scrivener (2004) shows that as the cement grains dissolve, this might leave
26
27 594 a hollow shell (Scrivener, 2004). The various extent of reaction of individual cement
28
29
30 595 grains depends on their sizes: small cement grains hydrate completely in the first stages
31
32 596 and remain as hollow shells of hydration product; whereas big grains further hydrate
33
34
35 597 which forms denser hydration products and which fill in the gap between shell and grain
36
37 598 (Muller, 2014). In this study it is also noticeable that calcium-rich reactive phases react
38
39
40 599 at different rates: some completely dissolve after 28 days leaving a hollow shell while
41
42 600 other remain with their initial structure and still contain calcium. Consequently, and
43
44
45 601 similarly to what is described in the literature, depending on the calcium nodule size, the
46
47 602 local products formed slightly differ which could lead to local variation of the inherent
48
49 603 material properties.

50
51
52 604

53
54 605 *3.4.2 Pore network characteristics*
55
56
57
58
59
60
61
62
63
64
65

1 606 Regarding the pore network characteristics of cement systems, two populations of pores
2
3 607 are generally distinguished: (i) capillary pores which correspond to space not being filled
4
5 608 by solid products of hydration, and (ii) small pores called gel pores associated to the
6
7
8 609 intrinsic porosity of Calcium Silicate Hydrates C-S-H. Over time, while chemical
9
10 610 reactions proceed the population of capillary pores decreases whereas the population of
11
12 611 gel pores increases, which may lead to the formation of disconnected spaces (Jennings et
13
14 612 al., 2008). Our alkali activated binder shows similar tendencies that is a progressive
15
16 613 decrease of intermediate pores or capillary pores while a new class of pores associated
17
18 614 with silicate-calcium chain products is detected using Mercury Intrusion Porosimetry.
19
20
21
22
23
24

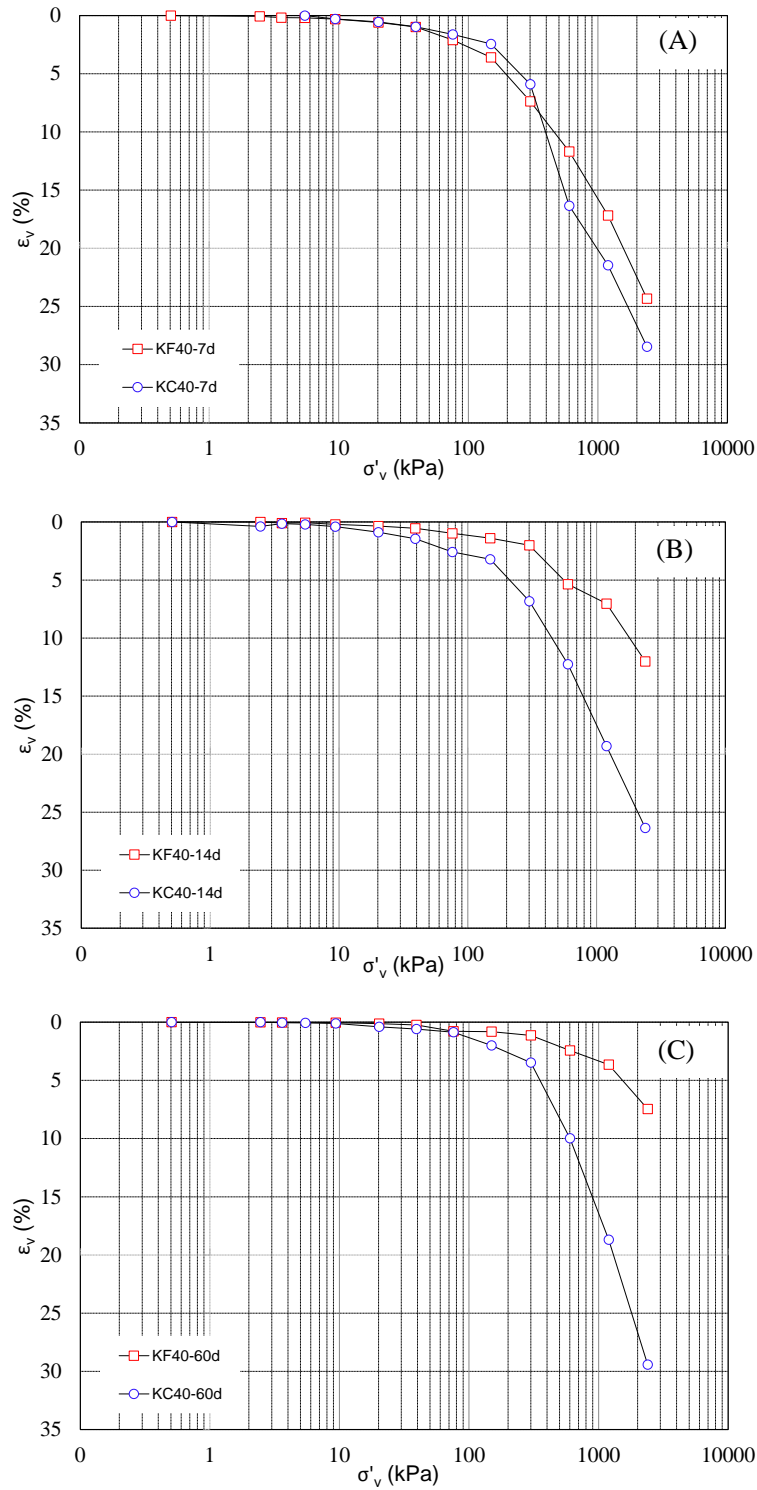
25 616 *3.4.3 Macroscopic behaviour according to the microstructure evolution*

26
27 617 Since both the processes generating the microstructure and the evolution of the pore
28
29 618 network over time of our alkali activated binder are similar to cement systems, a similar
30
31 619 influence of the microstructure on the short and long-term performances can be expected.
32
33 620 Changes in the pore network strongly influence transport properties that govern the rate
34
35 621 of all major deterioration processes and the service life of building materials (Wong et
36
37 622 al., 2006). Namely the formation of gel pores inside the capillary spaces tends to decrease
38
39 623 the connectivity of the pore network inhibiting the transport of aggressive substances such
40
41 624 as acids, carbonate or chloride through concrete and therefore enhancing the material
42
43 625 durability (van Deventer et al., 2010; Muller, 2014).
44
45 626 Finally, despite the great inhomogeneity of the reactive fly ash the growth and widening
46
47 627 of new products appear to occur homogeneously across the sample at a millimetric scale
48
49 628 in our alkali activated materials which would benefit the formation of a homogeneously
50
51 629 reinforced material.
52
53
54
55
56
57
58
59
60
61
62
63
64
65

1 630 At volume scale of the sample, a comparison between the mechanical performance
2
3 631 induced by alkali activated binder (KF40) and by ordinary Portland cement (KC40) is
4
5 632 shown in Figure 14 for samples prepared with the same binder content and cured for 7,
6
7 633 14 and 60 days. No relevant changes in the compressibility curves are observed for KF40
8
9 634 and KC40 samples cured for 7 days before testing (Figure 14A). For longer curing times,
10
11 635 results show a higher compressibility reduction and yield stress increase for KF40 treated
12
13 636 samples compared to cement treated samples (Figures 14B and 14C). The post-yield
14
15 637 behaviour induced by ordinary Portland cement shows the highest slope of the
16
17 638 compressibility curve, highlighting a more evident destructuration stage for cement
18
19 639 treated samples at increasing vertical stresses.
20
21
22
23
24

25 640 ~~Experimental evidences, not reported in this study, confirm the improved mechanical~~
26
27 641 ~~behaviour of the alkali activated binder treated soils, with a relevant increase of stiffness~~
28
29 642 ~~compared to the not treated soil, an increase of the range of stresses to which the soil is~~
30
31 643 ~~subjected to limited strains under reversible behaviour, as well a destructuration stage~~
32
33 644 ~~beyond that stress level. An improved shear resistance is also clearly visible after 28 days~~
34
35 645 ~~of curing and associated to contractile behaviour.~~
36
37
38
39
40
41
42
43
44
45
46
47
48
49
50
51
52
53
54
55
56
57
58
59
60
61
62
63
64
65

1
2
3
4
5
6
7
8
9
10
11
12
13
14
15
16
17
18
19
20
21
22
23
24
25
26
27
28
29
30
31
32
33
34
35
36
37
38
39
40
41
42
43
44
45
46
47
48
49
50
51
52
53
54
55
56
57
58
59
60
61
62
63
64
65



646

647 **Fig. 14** One dimensional compression curves of treated samples as function of binder
648 type (i.e. KF40 vs. KC40): (A) 7 days of curing; (B) 14 days of curing; (C) 60 days
649 of curing

650

651

1 652 **3 Conclusions**

2
3 653 The development of a novel binder that is an alkali activated calcium-rich fly ash for clay
4
5
6 654 soil stabilisation was investigated. The study of its microstructural evolution showed that
7
8 655 structural changes occur around calcium-bearing minerals from fly ash which constitute
9
10
11 656 the reactive phases, and whose dissolution leads to the formation of new compounds on
12
13 657 its surface first and then growing into the available space. Capillary pore spaces are
14
15 658 progressively filled by new compounds (i.e thernadite and silicate-calcium chains) over
16
17
18 659 time. Whereas the newly formed silicate-calcium chains possess an intrinsic porosity of
19
20
21 660 nanometric size conducting to the formation of a new class of small pores over time.
22
23 661 Different heterogenous matrices of various porosity and arrangement are however
24
25 662 observed across the material and owed to the high heterogeneity of fly ash whose particles
26
27
28 663 locally react differently.

29
30 664 The interaction between the binder and kaolin showed that small sized kaolinite platelets
31
32 665 fill the spaces between coarser grains from fly ash. Kaolin is therefore leading the
33
34
35 666 microstructural organisation, that is, the pore network is characterised by pores ranging
36
37
38 667 in lower size compared to the binder. Nevertheless, the microstructural changes remain
39
40 668 similar over time i.e. filling of capillary pores and appearance of nanometric pores from
41
42 669 silicate-calcium chains.

43
44 670 **One-dimensional compression tests performed on treated sample highlighted the**
45
46
47 671 **effectiveness of alkali activated binders to promote an improvement of the mechanical**
48
49
50 672 **behaviour of treated soil. A reduction of compressibility and increase of the yield stress**
51
52 673 **soil was observed since the very short term.**

53
54 674 The observed microstructural evolution is similar to the one of cement system and should
55
56
57 675 therefore conduct to akin performances that is an increase in strength and ability to resist

1 676 to aggressive substances due to changes in transport properties. It has been confirmed by
2
3 677 observing the similarities of the mechanical performance of alkali activated binder treated
4
5 678 samples with cement treated ones for short curing time. A marked improvement of the
6
7
8 679 mechanical behaviour of soil is induced by alkali activated binder starting from 14 days
9
10
11 680 of curing, representing a viable sustainable alternative to the use of ordinary stabilizing
12
13 681 agent for soil improvement.

14
15 682 However, regarding the complexity of both cement and alkali activated systems which
16
17
18 683 are multi-components systems, a coupling of those microstructural observations with
19
20
21 684 mechanical performances and transport properties is of further interest. Namely, a
22
23 685 complementary three-dimensional characterisation of the pore network using for instance
24
25 686 microtomography would greatly help to assess the connectivity and tortuosity of the pore
26
27
28 687 network which are primordial parameters to understand properly transport properties and
29
30 688 therefore durability. Using micro-indentation coupled with Scanning Electron Imaging
31
32
33 689 would also allow to measure local hardness variations following the extent of reaction of
34
35 690 calcium particles and therefore help to apprehend how significant are the local
36
37
38 691 microstructural variations for the mechanical performances at a macroscopic scale.

39
40 692

41 42 693 **Acknowledgements**

43
44
45 694 The authors wish to acknowledge the support of the European Commission via the Marie
46
47 695 Skłodowska-Curie Innovative Training Networks (ITN-ETN) project TERRE 'Training
48
49
50 696 Engineers and Researchers to Rethink geotechnical Engineering for a low carbon future'
51
52 697 (H2020-MSCA-ITN-2015-675762).

53
54
55 698

56 57 699 **References**

1 700 Askeland, D.R., Fulay, P.P., Wright, W.J., 2011. The science and engineering of
2
3 701 materials, 6th ed. ed. Cengage Learning, Stamford, CT.
4
5 702 Basha E.A., Hashim R., Muntohar A., 2003. Effect of the cement-rice husk ash on the
6
7 703 plasticity and compaction of soil, *Electron. J. Geotech. Eng.* 8.
8
9 704 Buchwald, A., Kaps, C., Hohmann, M., 2003. Alkali-activated binders and pozzolan
10
11 705 cement binders—complete binder reaction or two sides of the same story, in: *Proceedings*
12
13 706 of the 11th International Conference on the Chemistry of Cement. Portland Cement
14
15 707 Association Durban, South Africa, pp. 1238–1246.
16
17 708 Chemed, Y., 2015. Effect of hydrated lime on kaolinite surface properties and its
18
19 709 rheological behaviour. Université de Nantes.
20
21 710 Clemens, H., Mayer, S., Scheu, C., 2008. Microstructure and Properties of Engineering
22
23 711 Materials. *Neutrons Synchrotron Radiat. Eng. Mater. Sci. Fundam. Appl.* 1–20.
24
25 712 Coudert, E., Paris, M., Deneele, D., Russo, G., Tarantino, A., 2019. Use of alkali activated
26
27 713 fly ash binder for kaolin clay soil stabilisation: Physicochemical evolution. *Constr. Build.*
28
29 714 *Mater.* 201 (2019) 539–552, <https://doi.org/10.1016/j.conbuildmat.2018.12.188>
30
31 715 Cristelo, N., Glendinning, S., Fernandes, L., Pinto, A.T., 2012. Effect of calcium content
32
33 716 on soil stabilisation with alkaline activation. *Constr. Build. Mater.* 29, 167–174.
34
35 717 <https://doi.org/10.1016/j.conbuildmat.2011.10.049>
36
37 718 Cristelo, N., Glendinning, S., Teixeira Pinto, A., 2011. Deep soft soil improvement by
38
39 719 alkaline activation. *Proc. Inst. Civ. Eng. - Ground Improv.* 164, 73–82.
40
41 720 <https://doi.org/10.1680/grim.900032>
42
43 721 Duxson P, Provis JL, Lukey GC, Van Deventer JS, 2007. The role of inorganic polymer
44
45 722 technology in the development of ‘green concrete’. *Cem. Concr. Res.* 2007; 37:1590–7
46
47 723 Fang, G., Bahrami, H., Zhang, M., 2018. Mechanisms of autogenous shrinkage of alkali-
48
49
50
51
52
53
54
55
56
57
58
59
60
61
62
63
64
65

1 724 activated fly ash-slag pastes cured at ambient temperature within 24 h. *Constr. Build.*
2
3 725 *Mater.* 171, 377–387. <https://doi.org/10.1016/j.conbuildmat.2018.03.155>
4
5 726 James J., Pandian P.K., 2016. Industrial wastes as auxiliary additives to cement/lime
6
7 727 stabilization of soils, *Adv. Civ. Eng.* 2016 1–17.
8
9
10 728 Jennings, H.M., Bullard, J.W., Thomas, J.J., Andrade, J.E., Chen, J.J., Scherer, G.W.,
11
12 729 2008. Characterization and Modeling of Pores and Surfaces in Cement Paste:
13
14 730 Correlations to Processing and Properties. *J. Adv. Concr. Technol.* 6, 5–29.
15
16
17 731 Lawrence, M., Jiang, Y., 2017. Porosity, Pore Size Distribution, Micro-structure, in:
18
19 732 Amziane, S., Collet, F. (Eds.), *Bio-Aggregates Based Building Materials*. Springer
20
21 733 Netherlands, Dordrecht, pp. 39–71. https://doi.org/10.1007/978-94-024-1031-0_2
22
23
24 734 McLellan BC, Williams RP, Lay J, Van Riessen A, Corder GD., 2011. Costs and carbon
25
26 735 emissions for geopolymer pastes in comparison to Ordinary Portland Cement. *J. Clean*
27
28 736 *Prod* 2011; 19:1080–90
29
30
31 737 Muller, A.C.A., 2014. Characterization of porosity & CSH in cement pastes by 1H NMR.
32
33 738 École Polytechnique Fédérale de Lausanne, Suisse.
34
35
36 739 Nalbantoğlu Z., 2004. Effectiveness of class C fly ash as an expansive soil stabilizer,
37
38 740 *Constr. Build. Mater.* 18, 377–381.
39
40
41 741 Nath, S.K., Maitra, S., Mukherjee, S., Kumar, S., 2016. Microstructural and
42
43 742 morphological evolution of fly ash based geopolymers. *Constr. Build. Mater.* 111, 758–
44
45 743 765. <https://doi.org/10.1016/j.conbuildmat.2016.02.106>
46
47
48 744 Provis, J.L., Deventer, J.S.J. va., 2009. *Geopolymers Structure, processing, properties*
49
50 745 *and industrial applications*, Woodhead Publishing in materials. Woodhead, Cambridge.
51
52
53 746 Rios, S., Cristelo, N., Viana da Fonseca, A., Ferreira, C., 2016. Structural Performance
54
55 747 of Alkali-Activated Soil Ash versus Soil Cement. *J. Mater. Civ. Eng.* 28, 4015125.
56
57
58
59
60
61
62
63
64
65

1 748 [https://doi.org/10.1061/\(ASCE\)MT.1943-5533.0001398](https://doi.org/10.1061/(ASCE)MT.1943-5533.0001398)
2
3 749 Sargent, P., 2015. The development of alkali-activated mixtures for soil stabilisation. In
4
5 750 Handbook of alkali-activated cements, mortars and concretes (pp. 555-604). Woodhead
6
7 751 Publishing
8
9 752 Scrivener, K.L., 2004. Backscattered electron imaging of cementitious microstructures:
10
11 753 understanding and quantification. *Cem. Concr. Compos.* 26 8 935–945.
12
13 754 Scrivener, K.L., Kirkpatrick, R.J., 2008. Innovation in use and research on cementitious
14
15 755 material. *Cem. Concr. Res.* 38, 128–136.
16
17 756 <https://doi.org/10.1016/j.cemconres.2007.09.025>
18
19 757 Shi, C., Krivenko, P.V., Roy, D.M., 2006. Alkali-activated cements and concretes. Taylor
20
21 758 & Francis, London ; New York.
22
23 759 Silva, R.A., Oliveira, D.V., Miranda, T., Cristelo, N., Escobar, M.C., Soares, E., 2013.
24
25 760 Rammed earth construction with granitic residual soils: The case study of northern
26
27 761 Portugal. *Constr. Build. Mater.* 47, 181–191.
28
29 762 <https://doi.org/10.1016/j.conbuildmat.2013.05.047>
30
31 763 Singhi, B., Laskar, A.I., Ahmed, M.A., 2016. Investigation on Soil–Geopolymer with
32
33 764 Slag, Fly Ash and Their Blending. *Arab. J. Sci. Eng.* 41, 393–400.
34
35 765 <https://doi.org/10.1007/s13369-015-1677-y>
36
37 766 Tenn, N., Allou, F., Petit, C., Absi, J., Rossignol, S., 2015. Formulation of new materials
38
39 767 based on geopolymer binders and different road aggregates. *Ceram. Int.* 41, 5812–5820.
40
41 768 <https://doi.org/10.1016/j.ceramint.2015.01.010>
42
43 769 United Nations, 2004. A More Secure World: Our Shared Responsibility. Report of the
44
45 770 Secretary-General's High-level Panel on Threats, Challenges and Change, 2004.
46
47 771 van Deventer, J.S.J., Provis, J.L., Duxson, P., Brice, D.G., 2010. Chemical Research and
48
49
50
51
52
53
54
55
56
57
58
59
60
61
62
63
64
65

1 772 Climate Change as Drivers in the Commercial Adoption of Alkali Activated Materials.
2
3 773 Waste Biomass Valorization 1, 145–155. <https://doi.org/10.1007/s12649-010-9015-9>
4
5
6 774 van Deventer, J.S.J., San Nicolas, R., Ismail, I., Bernal, S.A., Brice, D.G., Provis, J.L.,
7
8 775 2015. Microstructure and durability of alkali-activated materials as key parameters for
9
10
11 776 standardization. J. Sustain. Cem.-Based Mater. 4, 116–128.
12
13 777 <https://doi.org/10.1080/21650373.2014.979265>
14
15
16 778 Vitale E., Russo G., Deneele D. 2019. Multi-scale analysis on soil improved by alkali
17
18 779 activated binders. E3S Web of Conferences 92, 11003 (2019) - IS-Glasgow 2019;
19
20 780 <https://doi.org/10.1051/e3sconf/20199211003>
21
22
23 781 Vitale E., Marocco A., Khatib M., Russo G. 2020a. Hydro-mechanical behaviour of
24
25 782 alkali-activated binder treated soil. E3S Web of Conferences 195, 06003 (2020) – E-
26
27 783 UNSAT 2020; <https://doi.org/10.1051/e3sconf/202019506003>
28
29
30 784 Vitale E., Russo G., Deneele D. 2020b. Use of Alkali-Activated Fly Ashes for Soil
31
32 785 Treatment. Geotechnical Research for Land Protection and Development. CNRIG 2019.
33
34
35 786 Lecture Notes in Civil Engineering, vol 40. Springer
36
37 787 Vitale, E., Russo, G., Dell’Agli, G., Ferone, C., and Bartolomeo, C. 2017. Mechanical
38
39 788 behaviour of soil improved by alkali activated binders. Environments 4(4), 80.
40
41 789 <https://doi.org/10.3390/environments4040080>
42
43
44 790 Wardhono, A., Law, D.W., Strano, A., 2015. The Strength of Alkali-activated Slag/fly
45
46 791 Ash Mortar Blends at Ambient Temperature. Procedia Eng. 125, 650–656.
47
48 792 <https://doi.org/10.1016/j.proeng.2015.11.095>
49
50
51 793 Wilkinson, A., Haque, A., Kodikara, J., 2010. Stabilisation of clayey soils with industrial
52
53 794 by-products: part A. Proc. Inst. Civ. Eng. - Ground Improv. 163, 149–163.
54
55 795 <https://doi.org/10.1680/grim.2010.163.3.149>
56
57
58
59
60
61
62
63
64
65

1 796 Wong, H.S., Buenfeld, N.R., Head, M.K., 2006. Estimating transport properties of
2
3 797 mortars using image analysis on backscattered electron images. *Cem. Concr. Res.* 36,
4
5 798 1556–1566.
6
7
8 799 Xi F., Davis S. J., Ciaias P., Crawford-Brown D., Guan D., Pade C., Shi T., Syddall M.,
9
10 800 Lv J., Ji L., Bing L., Wang J., Wei W., Yang K.-H., Lagerblad B., Galan I., Andrade C.,
11
12 801 Zhang Y., Liu Z. 2016. Substantial global carbon uptake by cement carbonation, *Nature*
13
14 802 *Geoscience*, 9, 12-2016
15
16
17 803 Zhang Z, Provis JL, Reid A, Wang H., 2014. Geopolymer foam concrete: an emerging
18
19 804 material for sustainable construction. *Constr Build Mater* 2014; 56:113–27.
20
21
22 805 Zhang, M., Guo, H., El-Korchi, T., Zhang, G., Tao, M., 2013. Experimental feasibility
23
24 806 study of geopolymer as the next-generation soil stabilizer. *Constr. Build. Mater.* 47,
25
26 807 1468–1478. <https://doi.org/10.1016/j.conbuildmat.2013.06.017>
27
28
29
30 808
31
32
33
34
35
36
37
38
39
40
41
42
43
44
45
46
47
48
49
50
51
52
53
54
55
56
57
58
59
60
61
62
63
64
65